

Copyright
by
Ryan Donald Williams
2007

**The Dissertation Committee for Ryan Donald Williams Certifies that this is the
approved version of the following dissertation:**

The Fabrication of Specialized Probes for Surface Metrology

Committee:

Keith J. Stevenson, Supervisor

Paul F. Barbara

Arumugam Manthiram

Jason B. Shear

David A. Vanden Bout

The Fabrication of Specialized Probes for Surface Metrology

by

Ryan Donald Williams, B.S.

Dissertation

Presented to the Faculty of the Graduate School of

The University of Texas at Austin

in Partial Fulfillment

of the Requirements

for the Degree of

Doctor of Philosophy

The University of Texas at Austin

December 2007

Dedication

To Bekki

Acknowledgements

I would like to thank Professor Keith Stevenson for guiding me through my time in graduate school. When I arrived as a new graduate student from a little school in Arkansas, he took the time to identify my strengths and made a conscious effort to provide me with appropriate opportunities. Those opportunities have been wonderful blessings, and I feel like I can never repay him. I wish him the best in the years to come.

To my fellow group members, past and present, I extend a special thank you. Your input and friendship has made my time at UT very enjoyable. Thanks to Todd McEvoy and Stephen Maldonado for the examples they were to me as scientists, as well as for their friendship. I also thank Tim Smith for introducing me to the atomic force microscope, which I had honestly never heard of before. Thanks to Jennifer Lyon for lending an ear when things got too real, for helping me figure out how to sign Keith's name, and for the help with interpreting the red chicken scratch notes that we all know and love. I also have to thank Ganesh Vijayaraghavan for his friendship, his input and his company on all those trips to Chipotle. Thanks also to Ben Hahn and Lilia Kondrachova

for their friendship, and I wish them both the best of luck as they fight over my awesome desk space. I wish all the best to all the rest of the group members.

I also thank all of my colleagues in other research groups and departments for their help and guidance. Thanks to Tom Doyle for his friendship and for his efforts as we worked together. I also thank Yangming Sun and Mike Tiner for their guidance and patience as I learned new techniques. I hope all the best for my fellow Harding University alumnus, Amanda Pollard, and I hope she finds her time at UT to be as rewarding as I have. I thank Mike White for being a wonderful example to me during my time in graduate school. He was a good friend and will be greatly missed.

There are several people outside of the department who I would like to thank. I am especially thankful for the tutelage and guidance of my undergraduate advisor, Dr. Edmond Wilson. His guidance at the beginning of this journey made everything much easier. I would like to thank Vladimir Mancevski and Paul McClure at Xidex Corp. for all of their help and support. The experiences and opportunities they have given me have been very rewarding, and I am very grateful to have worked with them. To my family, I extend the deepest gratitude. Their support gave me confidence in the face of seemingly insurmountable odds, and I can never express how much they have meant to me. To Bekki, my wife and mother to little Dora and Bud, you're the best thing that has ever happened to me. I could write another 100 pages and never say everything, so I'll just get on with the science.

A special thank you to SPRING, the Welch Foundation, TMI, CNM, and Xidex for instrumentation and monetary support.

The Fabrication of Specialized Probes for Surface Metrology

Publication No. _____

Ryan Donald Williams, Ph. D.

The University of Texas at Austin, 2007

Supervisor: Keith J. Stevenson

This dissertation will demonstrate the synergy of nanoscopic materials and surface metrology methods by the fabrication and implementation of CNT atomic force microscopy (AFM) tips, CNT scanning tunneling microscopy (STM) tips, Pt spike AFM tips, and Pt spike near-field scanning optical microscopy (NSOM) tips for the methods of critical dimension metrology, STM, AFM phase imaging, scanning surface potential AFM (SSPM), NSOM, and three-dimensional AFM. Chapter 1 provides a general overview of the information that will be discussed in this dissertation. Chapter 2 describes two methods for the simultaneous fabrication of carbon nanotube atomic force microscopy and scanning tunneling microscopy probes. The fabrication of these high resolution probes, as well as their imaging characteristics, is described in detail. Resolution standards were used to characterize their behavior and resolution limits. In

Chapter 3, the effect of high aspect ratio probe length on AFM phase imaging is studied by fabricating highly controllable Pt spike AFM tips. By monitoring phase shifts on homogenous surfaces as a function of Pt spike length, it is shown that attractive forces at the tip are significantly reduced when high aspect ratio structures are added to conventional AFM probes. In Chapter 4, the effect of probe geometry on scanning surface potential microscopy (SSPM) is described. By studying the effect of scan height in SSPM, it was found that large surface area probe geometries, such as conventional Pt coated AFM tips, have lower surface potential resolution because of contributions from the sides of the tip as well as the cantilever. Spatial resolution standards were probed to evaluate the effect of probe geometry on SSPM sensitivity and resolution. Chapter 5 describes the fabrication of specialized probes for three-dimensional atomic force microscopy, scanning near-field optical microscopy, and scanning electrochemical – atomic force microscopy (SECM-AFM). Using techniques described in Chapters 2-4, high aspect ratio structures were added to conventional probes used in 3D AFM, NSOM and SECM-AFM to solve limitations inherent to current probe designs for each method. Preliminary data indicates that each probe will have a significant beneficial effect on the resolution limit of its technique.

Table of Contents

List of Figures	xi
Chapter 1. Development of Advanced Tools for Surface Metrology	
1.1 Introduction	1
1.2 References	8
Chapter 2. Simultaneous Fabrication of Carbon Nanotube Atomic Force Microscopy and Scanning Tunneling Microscopy Tips Via Localized Chemical Vapor Deposition and Nanomanipulation	
2.1 Introduction	10
2.2 Experimental.....	13
2.3 Results and Discussion.....	15
2.3.1 CNT AFM and STM Tip Fabrication.....	16
2.3.2 CNT AFM Tip Characterization	20
2.3.3 CNT STM Tip Characterization.....	26
2.4 Conclusions	31
2.5 References	33
Chapter 3. The Effect of Probe Length on AFM Phase Imaging	
3.1 Introduction	36
3.2 Experimental.....	38
3.3 Results and Discussion.....	39
3.3.1 The Behavior of High Aspect Ratio AFM Tips in Phase Imaging ..	39
3.3.2 Pt Probe Fabrication	43
3.3.3 Effect of Pt Spike Length on Phase Shift	46
3.3.4 Quantification of Tip-To-Sample Forces.....	48
3.3.5 Effect of Humidity on Pt Spike Phase Shifts	51
3.4 Conclusions	51
3.5 References	54
Chapter 4. The Effect of Probe Geometry on Scanning Surface Potential Atomic Force Microscopy	
4.1 Introduction	57
4.2 Experimental.....	60
4.3 Results and Discussion.....	61
4.3.1 High Aspect Ratio Probe Development.....	61

4.3.2 IDEA testing.....	63
4.3.3 Effect of Tip Structure on Resolution of Pt Nanoparticles	73
4.3.4 Mesoporous TiO ₂ Studies	75
4.4 Conclusions	80
4.5 References	81
Chapter 5. Fabrication of Specialized Probes for 3D AFM, NSOM, and Combined SECM-AFM	
5.1 Introduction	84
5.1.1 Three-Dimensional Atomic Force Microscopy.....	85
5.1.2 Near-Field Scanning Optical Microscopy	88
5.1.3 Scanning Electrochemical Microscopy-Atomic Force Microscopy	89
5.2 Experimental.....	91
5.2.1 3D AFM Probe Fabrication.....	91
5.2.2 Pt Spike NSOM Fiber Fabrication	92
5.2.3 SECM-AFM Probe Fabrication	93
5.3 Results and Discussion.....	93
5.3.1 Pt-Based 3D AFM Probes.....	93
5.3.2 3D CNT-Based AFM Probes	98
5.3.3 3D C-CNT Boot Tips.....	101
5.3.4 Pt Spike NSOM Probes.....	103
5.3.5 Combined SECM-AFM Probes	106
5.4 Conclusions	107
5.5 References	110
Vita	113

List of Figures

- Figure 1.1 Graph of the number of published AFM studies in the past 19 years. While the number of AFM studies has risen exponentially, probe development has made very little progress since the development of batch-fabricated Si AFM tips. For AFM and other SPM techniques to be useful in high resolution nanoscopic studies, further development is essential. 4
- Figure 2.1 Chronoamperometric data showing the etching process for W wires. Vigorous bubbling occurs during the etching process, so the etching current was limited to 50mA. The etching process was halted when the current dropped by more than 4mA in less than 100ms, which indicated the completion point. b) SEM micrograph of the W wire after etching. The tapered region of the W wire was typically 300 μ m in length, and the tip radii were typically less than 20nm..... 18
- Figure 2.2 SEM micrograph of an etched W wire (bottom right) in contact with a carbon nanotube grown from the apex of a Si atomic force microscopy probe (top left). (b) Through the process of electron beam deposition of carbon, the CNT is affixed to the W wire so that when it is pulled away from the AFM probe the CNT breaks to produce both a CNT AFM (at Si) and CNT STM (at W) tip. Because of the nested shell structure of multi-walled carbon nanotube, a small segment of one of the resulting nanotube lengths is often smaller in diameter. Scale bars represent 500 nm. 19
- Figure 2.3 IV curve of a CNT grown on an AFM tip by chemical vapor deposition of ethylene. At current levels approaching 7 μ A, Joule heating occurs in the carbon nanotube causing failure of the crystalline structure. This failure typically occurs in the middle of the CNT's length, and results in sharpening at the ends where failure occurred..... 21
- Figure 2.4 1 x 1 μ m AFM topography image of an optical scatterometry grating obtained with a CNT AFM tip at different feedback levels. At the top of the AFM scan feedback settings typical of a conventional Si AFM tip were used, resulting in ringing. The gain levels were increased at regular intervals indicated by white lines in (a) until the ringing artifact was eliminated. Cross-sectional line scans of the AFM data show the effect of changing proportional gain from 1 (b), to 10 (c) and then 20 (d). 23

- Figure 2.5 1 x 1 μm AFM topography image of an optical scatterometry grating taken after optimum scanning parameters were determined to eliminate ringing. (b) Phase data of the AFM scan shows misalignment of the CNT AFM tip, resulting in a larger phase shift along the front side of each trench wall. (c) Cross-sectional line scan of the data depicted in Fig. 3a shows stable imaging of the vertical sidewalls. (d) SEM micrograph of the CNT AFM tip after repeated scanning of the scatterometry grating shows no change in the CNT alignment or length. Scale bar = 500 nm. 25
- Figure 2.6 1 x 1 μm AFM topography image of a scatterometry grating used to find the minimum measurable trench width when using a CNT AFM tip produced by this method. (b) Phase image of the area imaged in (a) shows contact with the bottom of the trench with a larger phase shift, thus clearly indicating successful imaging of the trench bottom. (c) A cross-sectional line scan taken at the indicated location on (a), showing the 33 nm minimum trench width measurable using the CNT AFM tip. (d) SEM micrograph of the scatterometry grating. The area was used because the grating lines converged, allowing observation of the exact trench width when the CNT no longer contacts the bottom. Scale bar = 1000nm..... 27
- Figure 2.7 300 \times 300 nm STM image of freshly cleaved HOPG, showing step edges of the graphitic layers. (b) 5 \times 5 nm STM image of the same sample, showing atomic resolution obtained with a CNT STM tip. (c) 5 \times 5 nm STM image with good atomic resolution obtained with an annealed W STM tip. Cross-sectional line scans across the images on HOPG surface (bottom of (b) and (c)) show atomic spacing of 2.45 \AA obtained with both CNT STM and annealed W tips..... 29
- Figure 2.8 100 x 100 nm STM image of TiO_2 (110) obtained using a CNT STM tip, demonstrating stability of the tip over larger scan sizes. (b) 20 x 20 nm STM image obtained using a CNT STM tip, showing clear row to row resolution as well as hydroxyl groups formed from water dissociation on oxygen vacancies in the bridging oxygen rows on the surface.²⁵ A cross-sectional line scan taken from (b) (below) shows accurate row to row spacing of 0.65 nm. (c) 20 x 20 nm STM image of TiO_2 taken with a conventional, well annealed W STM tip. A cross-sectional line scan taken from (c) (below) shows row to row spacing similar to that of a CNT STM tip, which agrees with literature values.²⁵ 30

- Figure 3.1 Graph of the effect of tip-to-sample separation on the oscillation amplitude of a conventional AFM tip and a high aspect ratio AFM tip (b) on Si (100). c) Graph of the phase shift of the conventional AFM tip shown in (a), which is dominated by attractive forces (phase shift $>90^\circ$) throughout the approach curve. d) The phase shift for a high aspect ratio AFM tip enters the attractive mode similar to the conventional probe shown in (c), but repulsive forces due to intermittent contact between the tip and the surface become more intense than the attractive forces, sending the tip into the repulsive mode (phase shifts $<90^\circ$). 41
- Figure 3.2 Topography AFM image of an optical scatterometry grating acquired with a conventional SiO₂ AFM tip. b) Phase contrast image of the grating shown in (a). c) Topography image of the grating shown in (a) acquired with a HAR Pt spike AFM tip. d) The phase contrast image shows much higher sensitivity than the image acquired with the conventional SiO₂ AFM tip. 42
- Figure 3.3 SEM micrograph of a high aspect ratio Pt probe fabricated by electron beam deposition of (CH₃)₃ Pt (C_pCH₃). By confining the SEM beam to a spot at the apex of the probe, a columnar structure 30nm in diameter can be formed. b) The resulting Pt spikes have conical apexes, with tip radii $<10\text{nm}$. c) By changing the orientation of the Pt spike, additional deposition steps allow formation of more complex structures. d) TEM images of the Pt spikes show that the resulting structures are not pure Pt metal, but a Pt-C matrix..... 44
- Figure 3.4 EDS spectra of a Pt spike shows that the deposition is not pure Pt metal, but a Pt-C matrix that is $99.1 \pm 0.6 \text{ wt\% Pt}$. b) Despite the small wt% C, IV curves indicate that the conductivity of a Pt spike AFM tip is very similar to that of a Pt metal coated AFM tip. 45
- Figure 3.5 Average phase shift of Pt spike probes on HOPG (black squares) and Si (100) (red circles) as a function of Pt spike length. Short Pt spikes were dominated by strong attractive forces, resulting in phase shifts $>90^\circ$. Pt spike probes longer than $\sim 150\text{nm}$ were dominated by repulsive forces, indicating that the surface area of the conical section of the probe was the

primary source of the strong attractive forces that caused the phase shifts to be higher than 90° in short Pt spike probes..... 47

- Figure 3.6 Average phase shift of Pt spike probes on HOPG as a function of spike length (black line) and the force exerted between the tip and surface due to attractive and repulsive forces (blue line). Pt spikes longer than 150nm experience 0.8nN more force than Pt spikes shorter than 150nm. This difference is due to attractive forces being minimized due to the conical section of the AFM tip being further from the surface while the tip makes intermittent contact..... 50
- Figure 3.7 Graph of the effect of humidity on phase shift of 0nm, 180nm, and 560nm Pt spike AFM tips. As expected, the 0nm Pt spike had a reduction in phase shift with decreased humidity, indicating that capillary forces are the primary attractive forces for large tip geometries. Addition of a high aspect ratio structure (180nm and 560nm Pt spikes) reduces the surface area near the sample surface, which results in a decrease in capillary forces. As a result, the capillary forces are so small that humidity variations have no resolvable effect on the phase shift..... 52
- Figure 4.1 SEM micrograph of a conventional Pt coated AFM tip used for SSPM studies. b) SEM micrograph of a Pt spike AFM tip fabricated by electron beam induced deposition of a Pt organometallic. (7nm radius) c) SEM micrograph of a conventional Pt coated AFM tip that has been FIB milled to reduce the surface area of the tip structure while keeping the tip radius $<20\text{nm}$ 62
- Figure 4.2 Schematic of a surface potential measurement on an interdigitated electrode array. The alternating electrodes allow different potentials (V_A and V_B) to be applied and measured by the tip while the surface topography remains constant. As the probe scans over the sample, the attractive forces due to the potential difference between the tip and the surface are eliminated by applying a bias to the tip that nulls the tip to surface potential difference..... 64
- Figure 4.3 50x50 μm AFM topography image of an interdigitated electrode array used to evaluate the performance of high aspect ratio SSPM probes on biased surfaces. b) Surface potential data acquired during an interleave scan at 10nm above the surface shown area in (a) with applied potentials of $\pm 4\text{V}$.

	An external bias switching circuit was used so bias would only be applied during the interleave mode of the SSPM scan. c) Cross sections of the topography and surface potential data show the alternating potentials of the electrodes. All data acquired with a FIB milled conventional SSPM probe (tip radius $\leq 10\text{nm}$).	65
Figure 4.4	AFM topography image of the interdigitated electrode array shown in Figure 4.3a acquired with a conventional Pt coated tip, a Pt spike tip, and a FIB milled high aspect ratio Si tip. b) By applying the bias to the electrodes in the interleave scan and not the topography scan, accurate surface topography traces can be acquired with all three tips. The similar traces for all three probes ensure that there are no topographical effects (dissimilar interleave scans) in the surface potential data.	66
Figure 4.5	Surface potential line scans of the interdigitated electrode array (IDEA) shown in Figure 4.3a acquired at different bias levels with a conventional Pt coated SPM probe. Figures 4.5b and 4.5c show surface potential data acquired with a Pt spike and high aspect ratio Si tip, respectively.	68
Figure 4.6	Graph of the potential difference measured with each SSPM probe with respect to the applied potential. All of the probes experienced surface potential averaging, which lead to a smaller measured surface potential than what was applied to the interdigitated electrodes.	69
Figure 4.7	Graph of the effect of scan height on measured surface potential of a $\pm 2\text{V}$ DC interdigitated electrode array with a conventional Pt coated SSPM tip, a Pt spike tip (b) and a high aspect ratio FIB milled Si tip (c) Pt spike tips showed the least change in measured surface potential as a function of height, while high aspect ratio FIB milled tips showed sharper transitions at the interfaces of different materials (e.g. electrode to glass to electrode).	71
Figure 4.8	Graph of the measured potential difference between a -2V and $+2\text{V}$ biased interdigitated electrode as a function of scan height. Data from all three probes indicate that none of the tips are capable of resolving the surface potential difference between the two electrodes of the IDEA, regardless of scan height. Pt spike tips, while less accurate than conventional tips at scan heights less than 300nm , are more accurate at large scan heights. High aspect ratio FIB milled Si tips are the least accurate of the three	

probes, though the probe shows the sharpest transition between surface potentials indicating high sensitivity..... 72

- Figure 4.9 AFM topography image of a 3nm Pt nanoparticle on a Si wafer acquired with a HAR Si SSPM tip. b) Surface potential image taken of the same Pt nanoparticle. c) Graph of the topography and surface potential data of the Pt nanoparticle (indicated on a, b) indicated that HAR FIB milled Si tips can resolve a surface potential difference of 75mV between the Pt nanoparticle and the Si surface. d) Graph of topography and SSPM data acquired with a conventional Pt coated Si tip. The large surface area of the conventional probe resulted in greater surface potential averaging, which lead to a much smaller potential difference (<20mV) between the Pt nanoparticle and the Si surface. 74
- Figure 4.10 SEM micrograph of a mesoporous TiO₂ film deposited on an ITO electrode. The hexagonally packed pores (10nm) provide a well defined resolution standard for SSPM. b) Gold nanoparticles were added to the pores by electrophoretic migration and studied with SSPM. 76
- Figure 4.11 1x1 micron topography image of the TiO₂ surface structure using a conventional Pt coated SSPM tip. b) SSPM image measured as a function of applied sample bias to the TiO₂ surface (0V, 5V, 10V DC). c) The measured surface potentials at 0, 5, and 10V DC indicated that the nonconductive nature of the TiO₂ film had very little effect on measured surface potential; however the porous framework of the TiO₂ could not be resolved in the SSPM image. 77
- Figure 4.12 500 x 500nm topography image of the porous TiO₂ substrate. b) 500 x 500nm surface potential image of (a) shows clear resolution of the porous structure. c) Data from the line indicated in (a) and (b) shows typical potential differences between the pore and the walls of the TiO₂ substrate. High aspect ratio FIB milled AFM tips showed potential differences between the pore and the TiO₂ substrate of 50mV. 79
- Figure 5.1 Scheme showing acquired surface profile (line scan) (dotted line) using a conventional AFM tip with a constant scan rate. The geometry of the tip is not capable of accurately reproducing the true morphology of the surface due to convolution of the probe tip dimensions with the interrogated feature. b) Resulting 2D profile obtained when a special “boot” tip is used

with a conventional AFM at a constant scan rate. The high aspect ratio of the probe results in a better surface trace at the top of interrogated features, but the constant scan rate keeps the probe from imaging variations in the sidewall dimensions. c) Accurate surface profiles can be acquired with a “boot” tip when used with a 3D AFM, where an additional feedback loop allows variation of the scan rate as a function of Z..... 86

- Figure 5.2 SEM image of a conventional Si based 3D “boot” AFM probe. Commercially available Si boot tips have a flared Si ridge at the base of the high aspect ratio Si support (100nm) that allows them to image sidewalls and undercuts of surfaces, but they can only measure undercuts less than 30nm. b) SEM image of a custom built 3D AFM probe using Pt EBID to form a well defined imaging surface capable of imaging much larger undercuts..... 94
- Figure 5.3 SEM image of a calibration standard used for tip characterization of 3D AFM probes. b) Line scans of data acquired with a Pt boot tip (red trace) and a Si boot tip (blue trace). The Pt boot tip (c) was able to probe 350% further into the undercut of the calibration standard than the conventional Si boot tip (d). 96
- Figure 5.4 SEM image of a vertically oriented Pt spike deposited on a conventional AFM tip. b) The vertical structure was deposited to be a support structure for an angled Pt spike that would act as the imaging surface. The rigidity of the Pt deposits caused the structure to fail during use. 97
- Figure 5.5 SEM micrograph of a CNT cut by the electrical cutting method described in chapter 2. b) By placing an additional CNT in contact with the CNT at the apex, a small section can be welded in place with EBID of C. c) Once welded, the resulting structure can be shortened by additional electrical cutting steps to fabricate a bidirectional boot tip (d)..... 99
- Figure 5.6 SEM image of a C-CNT boot tip fabricated by chemical vapor deposition of C on a CNT AFM tip prepared with the methods described in chapter 2. b) SEM image of a 40nm boot tip fabricated on a 20nm CNT. Boot tips on this small size scale are not commercially available because of limitations with current Si-based fabrication schemes. 102

- Figure 5.7 SEM micrograph of the apex of an Al coated NSOM optical fiber. The 200nm Al coating often results in a completely or partially covered aperture that must be removed by FIB milling. b) SEM micrograph of an NSOM fiber after FIB milling. c) Topographical resolution is poor with Al coated NSOM fibers because of their large size, so Pt nanoparticles were deposited on the aperture to act as the surface used for acquiring topographical data. d) Profile of the probe shown in C. The Pt particle height should not exceed 10nm or the optical resolution will be adversely affected. 104
- Figure 5.8 SEM micrograph of a gold pattern deposited on ITO. b) NSOM topographical data of the pattern acquired using a Pt nanoparticle NSOM probe. The addition of the Pt nanoparticle allowed the probe to resolve much smaller features than was possible with a conventional tapered optical fiber. c) 2x2 μ m AFM topography data of the pattern acquired using a conventional Si AFM tip showed comparable resolution to that of the Pt nanoparticle NSOM tip..... 105
- Figure 5.9 SEM image of a Pt Spike AFM tip coated with a thin layer of parylene N polymer. Coating the entire surface allows only the end of the Pt tip to be the electroactive area in combined SECM-AFM measurements. b) SEM image of the SECM-AFM tip shown in (a) after the end was removed with a focused ion beam. c) Removal of the polymer and apex of the Pt spike allows the formation of a 30nm disk electrode..... 108

CHAPTER 1

Development of Advanced Tools for Surface Metrology

1.1 INTRODUCTION

For significant technological advances to occur in surface science and nanotechnology, new materials and processes must be developed, and their chemistries and properties must be fully characterized.¹ As these advancements occur, they create new requirements for the tools used to characterize the materials and processing steps.² For instance, in the semiconductor industry, transistor sizes have dropped from 3 μ m to 70nm in the last 15 years. Projections indicate that in 2019, when the 16nm transistor node is achieved, characterization methods must be able to resolve features as small as 4Å.³ Semiconductor development, like other nanoscopic materials research, requires characterization methods that can resolve features and properties beyond the size scale of current research in order to continue advancing at an appreciable rate, so development of new tools and characterization methods is of extreme importance.^{4, 5}

Many different techniques are used to characterize nanoscopic features, such as transmission electron microscopy (TEM), high-resolution scanning electron microscopy (SEM), and scanning probe microscopy (SPM),⁶ but while these techniques are available

for surface and material characterization, each has significant limitations that impede their use. TEM, having sub-nanometer resolution, is a great technique for evaluating nanoscopic surface features, but because samples must be conductive, stable in high vacuum, and often require thinning with a focused ion beam before imaging, most materials and devices cannot be studied while in operation. The advent of aberration corrected lenses has allowed SEMs to have resolution similar to TEM,² but like TEM, samples must be conductive, stable in vacuum, and sometimes require cross sectioning to fully characterize sample morphology.⁷ Additionally, SEMs induce localized deposition of C from residual pump oils and surface contaminations, which can lead to significant measurement errors.⁸ SPM is a non-destructive technique that requires no sample preparation prior to imaging, and because of its accuracy, it is frequently used for calibrating other methods.² While extremely accurate, the primary factor in the resolution limit of SPM and its various imaging modes is the design of the probes that are used to acquire surface properties.⁹

SPM is a general classification for techniques that acquire surface properties (topography, sample hardness, work function, etc.) by scanning a sharp probe on or near a surface. The first probes designed for scanning probe microscopes were fabricated from bent metal wires with electrochemically etched apices.^{5,10} These probes lacked reproducibility because of their one-off fabrication process, but improvement came with the development of mass-produced Si based SPM tips.¹¹⁻¹³ Since their development over

15 years ago, the number of AFM studies has grown exponentially while tip design has changed very little (Fig. 1). Since sample feature sizes have been steadily decreasing since these probes were developed, further development is essential for SPM to be useful for high resolution nanoscopic studies.

In its simplest form, SPM is a technique similar to profilometry, where a sharp tip is scanned across a surface to obtain topographical data.¹⁴ This information is acquired by monitoring deflections of the tip as it follows the surface of the sample. Modern electronics and computing power enable very precise control of the probe as well as fast data collection, but the limit of the resolution of SPM currently lies in the probe used for data collection. Batch fabricated SiO₂ probes are good probes for general SPM studies because they are inexpensive, they have a relatively small tip radius (<20nm), and they are useful for collecting data on low aspect ratio samples (low height to width ratio). These studies aside, conventional probes do not provide sufficient resolution for more advanced studies on the challenging samples that are being produced in this nanoscopic age. The first major limitation of conventional SPM tips involves the large tip geometry, where cone angles (30°)¹⁵ prohibit imaging of vertical or nearly vertical structures (sidewall angle <30°). These large cone angles result in significant data convolution, and in many cases do not permit imaging of true structural dimensions. In addition to having a large size, their makeup (SiO₂, Si₃N₄) requires them to be coated with a metal film in order to be used in electrical SPM studies such as scanning surface potential AFM and

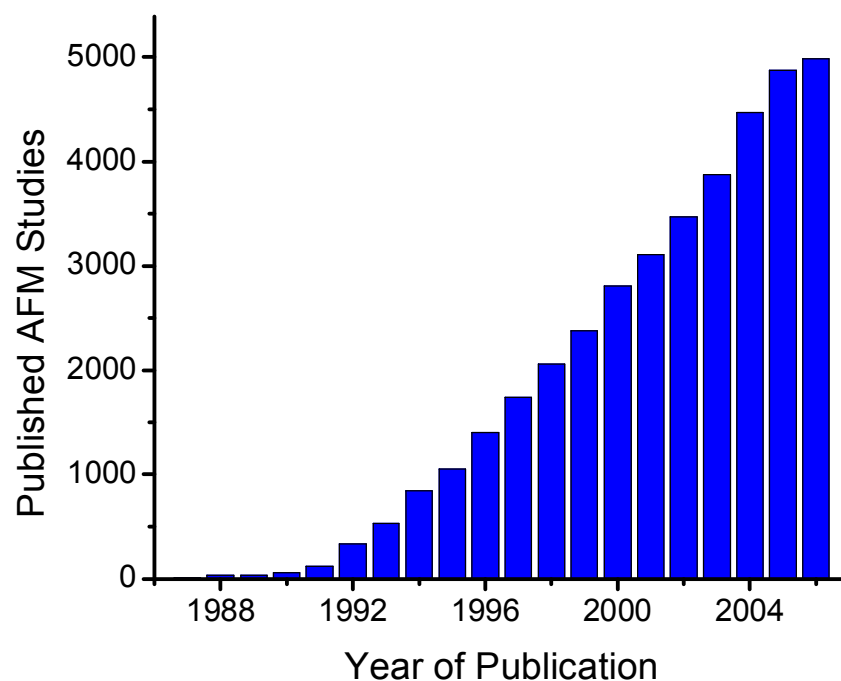


Figure 1.1 Graph of the number of published AFM studies in the past 19 years. While the number of AFM studies has risen exponentially, probe development has made very little progress since the development of batch-fabricated Si AFM tips. For AFM and other SPM techniques to be useful in high resolution nanoscopic studies, further development is essential.

tunneling AFM. This metal film, typically 20-50nm in thickness, is not durable, and peels off after prolonged use. If undetected, this slow degradation of conductivity can skew results and lead to false conclusions. Additionally, the peeled metal coating can result in data convolution by acting as an additional imaging surface in topographical studies, as well as electrical studies. The final major limitation of conventional probes is that they are subject to wear during surface studies, which can result in varying data quality over the duration of an experiment (e.g. varying tip geometry during topographical data acquisition). In three-dimensional metrology this problem is lessened by characterizing the tip before and after use, but this only results in an approximation since the true tip condition during the measurement is not known. Ideally, an SPM probe should enable scientists to probe surfaces of all geometries while not degrading over the duration of an experiment. Additionally, the probe should be conductive so nanoscopic features can be electrically characterized.

Despite these limitations, conventional probes have been used to characterize many nanoscopic samples, and their use has been influential in the development of nanotechnology. To enable its use in future studies, the same materials that have brought about the need for advances in SPM probes have been targeted as possible solutions for their limitations. One example of this is the development of carbon nanotube (CNT) SPM tips. Carbon nanotubes have unique structural, electrical, and chemical properties that make them ideal structures for

SPM tips. By carefully controlling growth conditions, carbon nanotube diameters (from one nanometer to tens of nanometers) and lengths (from ten nanometers to tens of microns) can be precisely controlled in order to achieve extremely high aspect ratios (high length to width ratio). In addition to having ideal surface geometry, CNTs, while not as conductive as true metals, are sufficiently conductive for use in electrical characterization techniques. Last, they are extremely durable and have the unique ability to bend elastically. While these properties make CNT SPM tips ideal for use in high resolution SPM studies, their widespread use is limited because of their low-yield fabrication process and subsequent lack of availability.

The synergy of nanoscopic materials and surface metrology methods will be demonstrated in this dissertation by the fabrication and implementation of CNT atomic force microscopy (AFM) tips, CNT scanning tunneling microscopy (STM) tips, Pt spike AFM tips, and Pt spike near-field scanning optical microscopy (NSOM) tips for the methods of critical dimension metrology, STM, AFM phase imaging, scanning surface potential AFM (SSPM), NSOM, and three-dimensional AFM. This dissertation is organized into five chapters, the first being a general introduction. Chapter 2 describes two methods for the simultaneous fabrication of carbon nanotube atomic force microscopy and scanning tunneling microscopy probes. Carbon nanotubes, having small diameters ($<10\text{nm}$), high aspect ratios, and unique chemical, electrical, and mechanical properties, provide

the ideal probe geometry when combined with conventional AFM probes. The fabrication of these high resolution probes, as well as their imaging characteristics, is described in detail. Furthermore, resolution standards were used to characterize the behavior of the probes, as well as the resolution limits for the probes.

In Chapter 3, the effect of high aspect ratio probe length on AFM phase imaging is studied by fabricating Pt spike AFM tips. By monitoring phase shifts on homogenous surfaces such as Si (100) and highly oriented pyrolytic graphite (HOPG) as a function of spike length, it is shown that attractive forces at the tip are significantly reduced when high aspect ratio structures are added to conventional AFM probes. Careful control of imaging conditions showed that the reduction in attractive forces at the tip were due to changes in surface area, which caused a reduction in capillary forces experienced when performing AFM measurements in ambient conditions.

In Chapter 4 the effect of probe geometry on scanning surface potential microscopy (SSPM) is described. By studying the effect of scan height in SSPM, it was found that large surface area probe geometries, such as conventional Pt coated AFM tips, have lower surface potential resolution because of contributions from the sides of the tip as well as the cantilever. These contributions cause surface potential averaging, and can be reduced by altering the probe geometry by focused ion beam milling. Pt nanoparticles and mesoporous TiO_2 films were used

as resolution standards to show increased surface potential resolution for high aspect ratio probe geometries.

Chapter 5 describes the fabrication of specialized probes for three-dimensional atomic force microscopy, scanning near-field optical microscopy, and scanning electrochemical – atomic force microscopy (SECM-AFM). Using techniques described in Chapters 2-4, high aspect ratio structures were added to conventional probes used in 3D AFM, NSOM and SECM-AFM to solve limitations inherent to current probe designs for each method. Preliminary data indicates that the addition of the high aspect ratio structures to each probe will have a significant beneficial effect on the resolution limit of each technique.

1.2 REFERENCES

1. Draper, J. W. Textbook on Chemistry. 10th ed, H. W. Derby Publishers: Cincinnati, **1853**.
2. Diebold, A. C. Characterization and Metrology for Nanoelectronics. *Front. Char. Met. Nanoelec.* **2007**, 34-39.
3. ITRS – International Technology Roadmap for Semiconductors, http://www.itrs.net/Links/2006Update/FinalToPost/08_Lithography2006Update.pdf, 2006.
4. Nesladek, P. Challenges of the Mask Manufacturing Approaching Physical Limits. *J. Phys. Chem. Sol.* **2007**, 68, 926-930.
5. Danzebrink, H.; Koenders, L.; Wilkening, G.; Yacoot, A.; Kunzmann, H. Advances in Scanning Force Microscopy for Dimensional Metrology. *Annals CIRP* **2006**, 55/2/2006, 841-878.
6. Garner, C. M.; Herr, D. Metrology For Emerging Research Materials and Devices. *Front. Char. Met. Nanoelec.* **2007**, 20-33.
7. Ukraintsev, V. A.; Baum, C.; Zhang, G.; Hall, C. L. The Role of AFM in Semiconductor Technology Development: the 65nm Technology Node and Beyond. *Proc of SPIE* **2005**, 5752, 127-139.
8. Lee, C. S.; Baker, S. E.; Marcus, M. S.; Yang, W.; Eriksson, M. A.; Hamers, R. J. Electrically Addressable Biomolecular Functionalization of Carbon Nanotube and Carbon Nanofiber Electrodes. *Nano Lett.* **2004**, 4(9), 1713-1716.
9. Wendel, M.; Lorenz, H.; Koothaus, J. P. Sharpened Electron Beam Deposited Tips for High Resolution Atomic Force Microscope Lithography and Imaging. *Appl. Phys. Lett.* **1995**, 75(25), 3732-3734.
10. Chen, L.; Cheung, C. L.; Ashby, P. D.; Lieber, C. M. Single-Walled Carbon Nanotube AFM Probes: Optimal Imaging Resolution of Nanoclusters and Biomolecules in Ambient and Fluid Environments. *Nano Lett.* **2004**, 4(9), 1725-1731.

11. Wickramasinghe, H. K. Scanning Probe Microscopy: Current Status and Future Trends. *J. Vac. Sci. Technol. A* **1990**, 8(1), 363-368.
12. Albrecht, T. R.; Akamine, S.; Carver, T. E.; Quate, C. F. Microfabrication of Cantilever Styli for the Atomic Force Microscope. *J. Vac. Sci. Technol. A* **1990**, 8(4), 3386-3396.
13. Akamine, S.; Barrett, R. C.; Quate, C. F. Improved Atomic Force Images Using Microcantilevers with Sharp Tips. *Appl. Phys. Lett.* **1990**, 57(3), 316-318.
14. Wolter, O.; Bayer, T.; Greschner, J. Micromachined Silicon Sensors for Scanning Force Microscopy. *J. Vac. Sci. Technol.* **1991**, 9, 1353.
15. Wang, Y.; Van der Weide, D. W. Microfabrication and Application of High-Aspect-Ratio Silicon Tips. *J. Vac. Sci. B* **2005**, 23(4), 1582-1584.
16. <http://www.spmtips.com> (Mikromasch)

CHAPTER 2

Simultaneous Fabrication of Carbon Nanotube Atomic Force Microscopy and Scanning Tunneling Microscopy Tips Via Localized Chemical Vapor Deposition and Nanomanipulation

2.1 INTRODUCTION

Scanning probe techniques such as atomic force microscopy (AFM) and scanning tunneling microscopy (STM) have become vital tools for high-resolution surface characterization, nanoscopic measurements and manipulation. Unfortunately, commercially available probes are still prone to tip-shape induced imaging artifacts, tip-radius irregularities, tip durability limitations, and tip induced sample degradation. Current technological drivers in the manufacturing of nanoelectronic devices have created significant demand for precise critical dimension (CD) measurement of nanoscopic spatial features such as trenches, undercuts and vias.¹ Carbon nanotube (CNT) based probe tips have been explored as possible candidates to meet this demand due to their unique chemical and mechanical properties, high-aspect length-to-width ratio and nanoscopic dimensions. Additionally, CNTs are mechanically robust and electronically conductive, offering further possibilities for development of high resolution probe tips for electrical characterization of nanoscopic features with improved durability.

Several reports have detailed the fabrication of CNT AFM tips via manual addition of previously grown CNTs onto commercially available Si cantilevers with various methods for attachment including gluing² and e-beam welding.³ Examples such as the “pick up” method described by Lieber⁴ and the electrophoretic method described by Zhou⁵ require no modification of a silicon-based AFM tip, but have low yields due to multistep nature of isolating and placing single CNTs. In an effort to increase CNT AFM tip yields, more complex processing steps, such as using a focused ion beam (FIB) to mill a channel into the side of an existing Si AFM probe, have been used to fabricate a guide for affixing a single CNT.⁶ Yet another method has used nanomanipulation⁷ to “pluck” an isolated CNT from a knife edge with a Si AFM tip. Furthermore, several fabrication methods have been reported that involve direct growth of CNTs onto the apex of a Si cantilever in order to develop a method for batch fabrication. Current direct growth methods, such as the “surface growth” method,⁸ require very little sample preparation but do not appear reproducible enough to be considered commercially economical nor scaleable for batch fabrication. The eleven-step fabrication procedure described by Meyeppan and coworkers⁹ represents one of the more complex assembly methods available for batch fabrication, and while this appears to be a viable method, it is not clear whether specific CNT tip characteristics such as alignment and length can be controlled without additional processing steps.

While there is an abundance of literature reports describing CNT AFM tips,²⁻¹¹ there are fewer examples of functional CNT-based STM tips. Conventional STM tips such as those made from etching¹² or cutting of metal wire¹³ are fully capable of imaging with atomic resolution, yet they are generally not very durable and lose resolution after repeated use or accidental surface contact. Since CNTs are conductive, high aspect ratio structures with nanometer diameters they offer a possible solution for making more robust STM tips.¹⁴ Similar to CNT AFM tips, the two main methods currently utilized for fabricating CNT STM tips are direct growth¹⁵ and manual attachment.¹⁶ CNT STM tips made via the direct growth method have several disadvantages such as the large size (ca 40 nm) of CNTs employed¹⁷ and the uncontrolled bundling or clustering of too many CNTs at the apex of the supporting metal wire.¹⁵⁻¹⁸ Manually attached CNT STM tips are more controlled in their properties, though they are significantly more time consuming to fabricate than direct growth methods.

In this work we describe an integrated approach for fabricating, in a few steps, functional CNT-based AFM and STM tips prepared from a single CNT grown via chemical vapor deposition on an existing silicon AFM cantilever. Using nanomanipulation, the “as grown” CNT AFM tip can be subsequently affixed to a tungsten wire and selectively cut to fabricate a CNT-based STM tip. Importantly, the nanomanipulation process allows for precise control of CNT tip characteristics including length and orientation. Various calibration standards are evaluated using CNT-based

AFM and STM tips fabricated from a single process to demonstrate the feasibility of this approach for producing high-quality, high-resolution CNT probe tips for scanning probe microscopy.

2.2 EXPERIMENTAL

Multiwalled CNTs (MWCNTs) were grown directly on non-contact AFM tips (BudgetSensors Tap300) via chemical vapor deposition of ethylene as described previously.⁸ By finely tuning the growth parameters, single freestanding multiwalled CNTs can be grown at the apex of the Si AFM tip with a high degree of vertical alignment. To shorten the length of the free standing CNT grown at the apex of the Si tip, a nanomanipulator system (Zyvex S-100 Nanomanipulator) was used in an electron microscope (FEI DB235) to move an etched W wire into contact with the CNT. Once in contact, the CNT was welded to the W wire by electron beam deposition of C from residual contaminants within the microscope chamber. The CNT, bound at both the Si apex and the W wire, was then pulled apart by overcoming the tensile strength of the CNT. In cases where CNT length needed to be finely tuned for experimental conditions, a second method was used that took advantage of the conductive nature of the CNTs. Similar to the mechanical shortening method, the CNT was brought into contact with both the AFM and W wires to form a conductive pathway between the Si AFM tip and W STM tip. By applying a large bias across the CNT ($\geq 15\text{V}$), localized Joule heating caused

breakdown of the CNT structure midway between the two probes. As a result of either procedure, a freestanding segment of the CNT was left on each probe tip that could then be directly used for AFM or STM experiments. The CNT AFM probes were tested with tapping mode atomic force microscopy, which was conducted using a Digital Instruments Bioscope Atomic Force Microscope with a Nanoscope IV controller. AFM experiments were conducted on scatterometry calibration gratings (test wafer, die 141) obtained from Sematech's Advanced Metrology Advisory Group (AMAG). Scan sizes varied from 500 nm x 500 nm to 1 μ m x 1 μ m, and the scan rate used was 0.5 Hz. To determine the accuracy of the AFM measurements, the probed area of the scatterometry grating was imaged with a scanning electron microscope (Leo 1530, 10keV).

STM experiments were performed with an Omicron variable temperature STM operated in an ultrahigh vacuum chamber (base pressure < 8 x 10⁻¹¹ Torr). The highly oriented pyrolytic graphite (HOPG) was prepared for STM imaging by removing the upper layers by cleaving with Scotch tape. The TiO₂ (110) single crystal was mounted on a modified double plate sample holder (Omicron), and was heated with a tungsten filament heater. To prepare a well-ordered TiO₂ (110) surface, the crystal underwent repeated cycles of Ne ion sputtering and UHV annealing (900-1000 K).²⁶ Commercial tungsten STM tips (Custom Probe Unlimited) were cleaned prior to use, via Ne⁺ sputtering and UHV annealing, while the CNT STM tips were not subjected to any cleaning procedure. All STM images were collected at room temperature in UHV using

constant current mode (~ 0.1 nA) while applying a positive bias (~ 1.0 V) to the sample surface. All images were processed using WSxM software (Nanotech, freeware).²⁷

2.3 RESULTS AND DISCUSSION

2.3.1 CNT AFM and STM Fabrication

Single multiwalled carbon nanotubes were synthesized by chemical vapor deposition of ethylene⁸ on conventional Si AFM tips, but the resulting CNTs had uncontrolled length. This lack of control was likely due to the random location of the Fe-based catalyst used as the CNT growth catalyst. CNTs grown by this procedure are typically 3-5 microns long, but because the origin of the growth varies, the resulting freestanding CNT can vary from ~ 50 nm to several microns in length. Previous experiments in our lab agree with other recent reports¹⁹ that precise length control is necessary for stable, high-resolution imaging with CNT AFM tips especially when investigating high aspect ratio vertical structures. Too long or too short of a CNT can cause unintended tip deflections due to repulsive or attractive tip-sample interactions. As such, the ability to control the length and orientation of the CNT becomes extremely important in an effort to minimize CNT AFM tip breakage during use and to improve imaging resolution when probing nanoscopic features.

To control the length of the CNT AFM tip, we have developed a method to shorten the CNT AFM tip while simultaneously producing a CNT STM tip. To

manipulate the CNTs and form a substrate for STM probes, etched W wires were prepared by electrochemical etching. 0.005-inch W wires were etched in 1.0M KOH using a Pt counter electrode and monitored with a custom LabView chronoamperometric etching program that limited the etching current and precisely controlled the etching conditions (Fig. 2.1a). Because etching W wires in KOH results in vigorous bubbling from hydrogen reduction, the maximum current was set to 50mA. This was necessary because large bubbles would begin to accumulate at the interface between the W wire and the KOH solution, causing uneven etching because of rising solution levels. As the etching current dropped below 15mA, the software monitored the changes in current and stopped the etching process if the current dropped by more than 4mA in less than 100ms. This current drop, while occasionally the result of a bursting bubble of H₂ gas, typically indicated the exact point where etching of the W wire was complete. The resulting tip radii were less than 20nm, and tapered region of the W wire was typically 300μm in length (Fig. 2.1b).

After etching the W wire, the wire was brought into contact with the CNT AFM tip in an SEM using a nanomanipulator (Fig. 2.2a). Since the junction between the W wire and the CNT was weak and only due to Van der Waals forces, the CNT was “welded” to the W wire by imaging the junction with the electron beam at high magnification. This procedure, also known as electron beam deposition, resulted in deposition of a thin layer of C at the W-CNT interface. The resulting bond, being

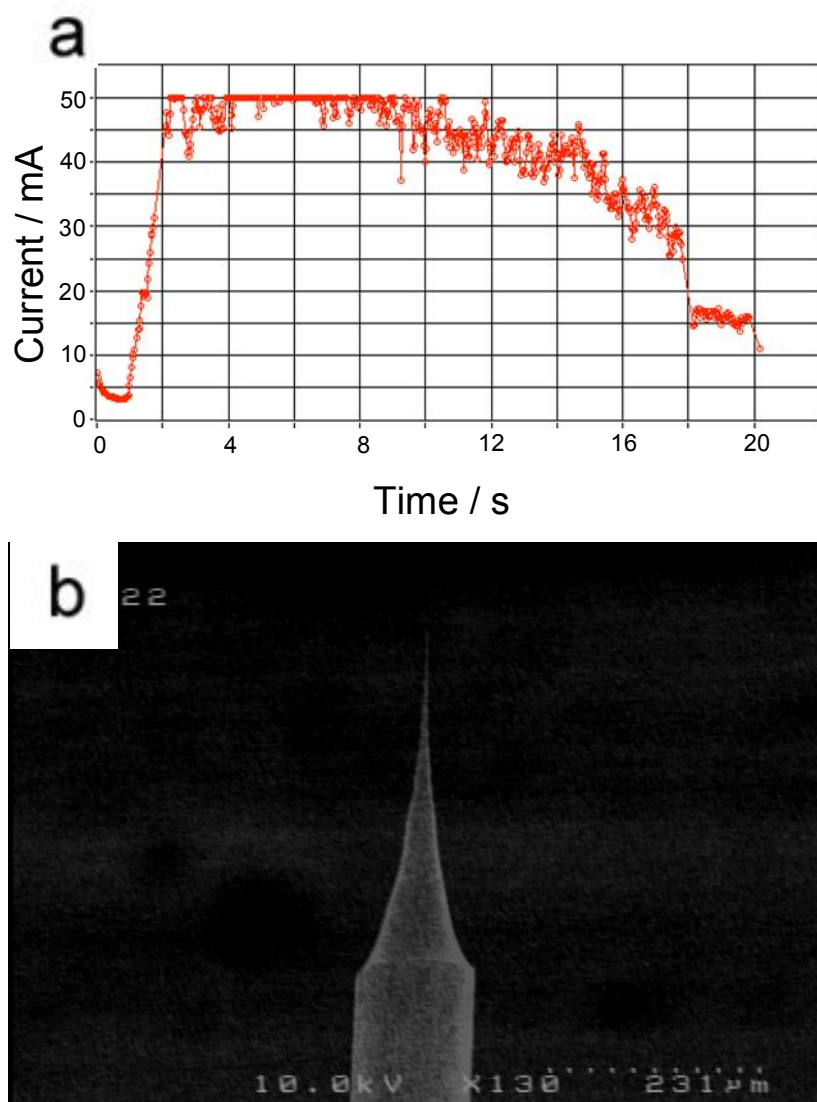


Figure 2.1 a) Chronoamperometric data showing the etching process for W wires. Vigorous bubbling occurs during the etching process, so the etching current was limited to 50mA. The etching process was halted when the current dropped by more than 4mA in less than 100ms, which indicated the completion point. b) SEM micrograph of the W wire after etching. The tapered region of the W wire was typically 300µm in length, and the tip radii were typically less than 20nm.

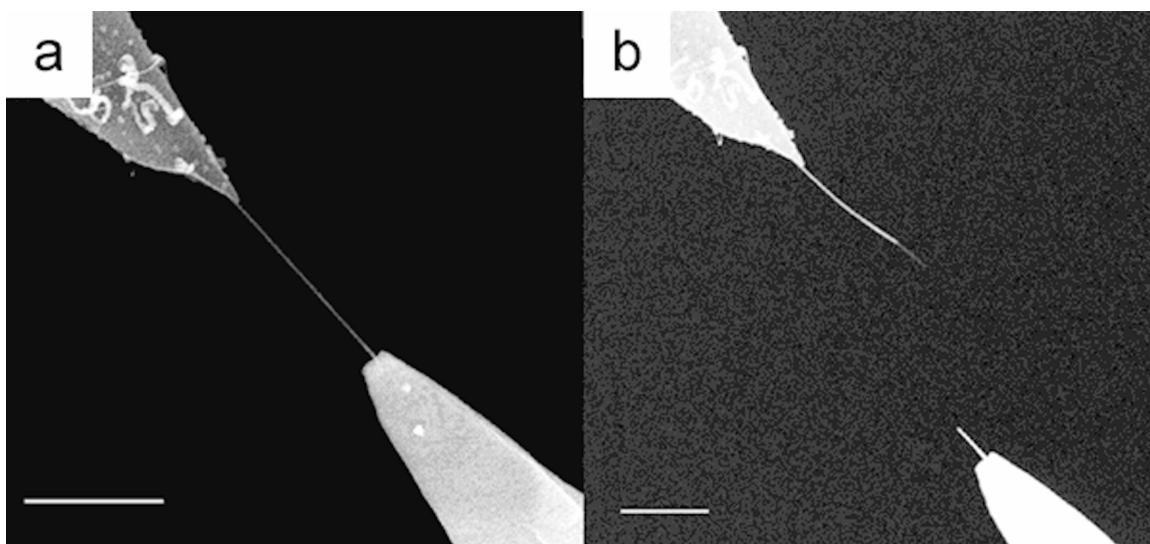


Figure 2.2. a) SEM micrograph of an etched W wire (bottom right) in contact with a carbon nanotube grown from the apex of a Si atomic force microscopy probe (top left). (b) Through the process of electron beam deposition of carbon, the CNT is affixed to the W wire so that when it is pulled away from the AFM probe the CNT breaks to produce both a CNT AFM (at Si) and CNT STM (at W) tip. Because of the nested shell structure of multi-walled carbon nanotube, a small segment of one of the resulting nanotube lengths is often smaller in diameter. Scale bars represent 500 nm.

stronger than the tensile strength of the CNT,²⁰ allowed the CNT to be mechanically shortened by pulling the Si AFM cantilever and the W wire apart with the nanomanipulator (Fig. 2.2b), resulting in the simultaneous formation of a CNT AFM (at Si) and a CNT STM (at W) tip. Because the CNTs used in these experiments were multi-walled, the fracture point of the carbon nanotube was not the same for all of the walls within the structure. As a result of the varying fracture point within the CNT, different diameters for CNT-AFM and CNT-STM tips were often observed at the fractured CNT apices. The reduced diameter in these fractured CNT segments provided the added benefit of improved spatial resolution relative to the original CNT. In situations where nanotube length was a critical factor, an alternative method for nanotube shortening was used.²¹ Differing from the mechanical method in only one step, the nanotubes could also be cut by application of a large bias ($\geq 15\text{V}$) across the AFM-STM tip junction rather than mechanically separating the two probes. Once the current flow through the CNT exceeded the capacity of the CNT, localized Joule-heating caused failure of the CNT (Fig 2.3). Because of the Joule heating at the failure point of the CNT, the resulting CNT apices were sharpened and had tip radii far less than the radii of the CNT.

2.3.2 CNT AFM Tip Characterization

Critical dimension (CD) measurements have always been challenging for atomic force microscopy because of the geometric limitations of commercially available scanning probes. High aspect ratio AFM tips, such as the CNT AFM tips prepared in this

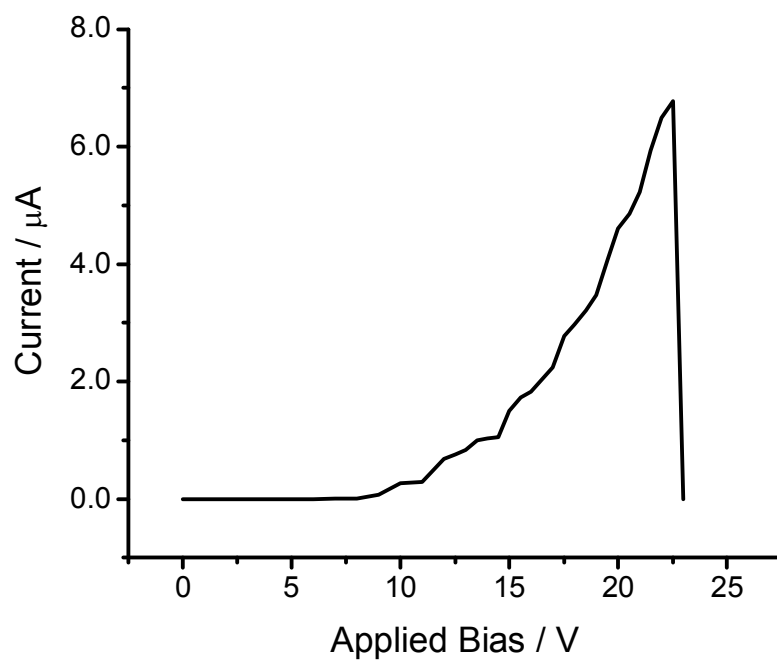


Figure 2.3 IV curve of a CNT grown on an AFM tip by chemical vapor deposition of ethylene. At current levels approaching $7\mu\text{A}$, Joule heating occurs in the carbon nanotube causing failure of the crystalline structure. This failure typically occurs in the middle of the CNT's length, and results in sharpening at the ends where failure occurred.

paper, allow CD measurements to be accurately performed in a nondestructive manner, unlike typical CD evaluation techniques such as TEM or cross-sectional SEM.²² Imaging performance was evaluated in tapping mode using fabricated CNT AFM tips on an optical scatterometry grating with 60 nm pitch. Since the average height of the grating was 160 nm, the length of the CNT was shortened to 200 nm to maximize CNT AFM tip stability. The CNTs' ability to bend elastically, while preventing catastrophic tip crash and subsequent breakage, has an adverse effect when brought near a parallel surface as the CNT tends to bend and adhere to the interrogated feature because of strong attractive van der Waals forces.³ When using intermittent mode AFM, this interaction is often seen as an abrupt change in oscillation amplitude, which causes the AFM feedback loop to overcompensate by raising the tip until no attractive force is sensed at the tip. At this point the tip oscillates at its resonant frequency with undamped amplitude, causing the AFM feedback loop to lower the tip in order to bring the oscillation amplitude nearer to the imaging set point. This kind of imaging artifact is often referred to as ringing²³ and occurs each time a CNT tip is brought near a parallel surface. If the gain levels of the feedback loop are not set appropriately, ringing will be seen at every vertical sidewall feature. To eliminate this artifact, the gain levels had to be significantly altered from typical set point levels. Figure 2.4a shows the effect of changing proportional gain levels while interrogating the scatterometry grating structure with a CNT AFM tip in tapping mode. A proportional gain value of 1, a scanning parameter typically suitable for a

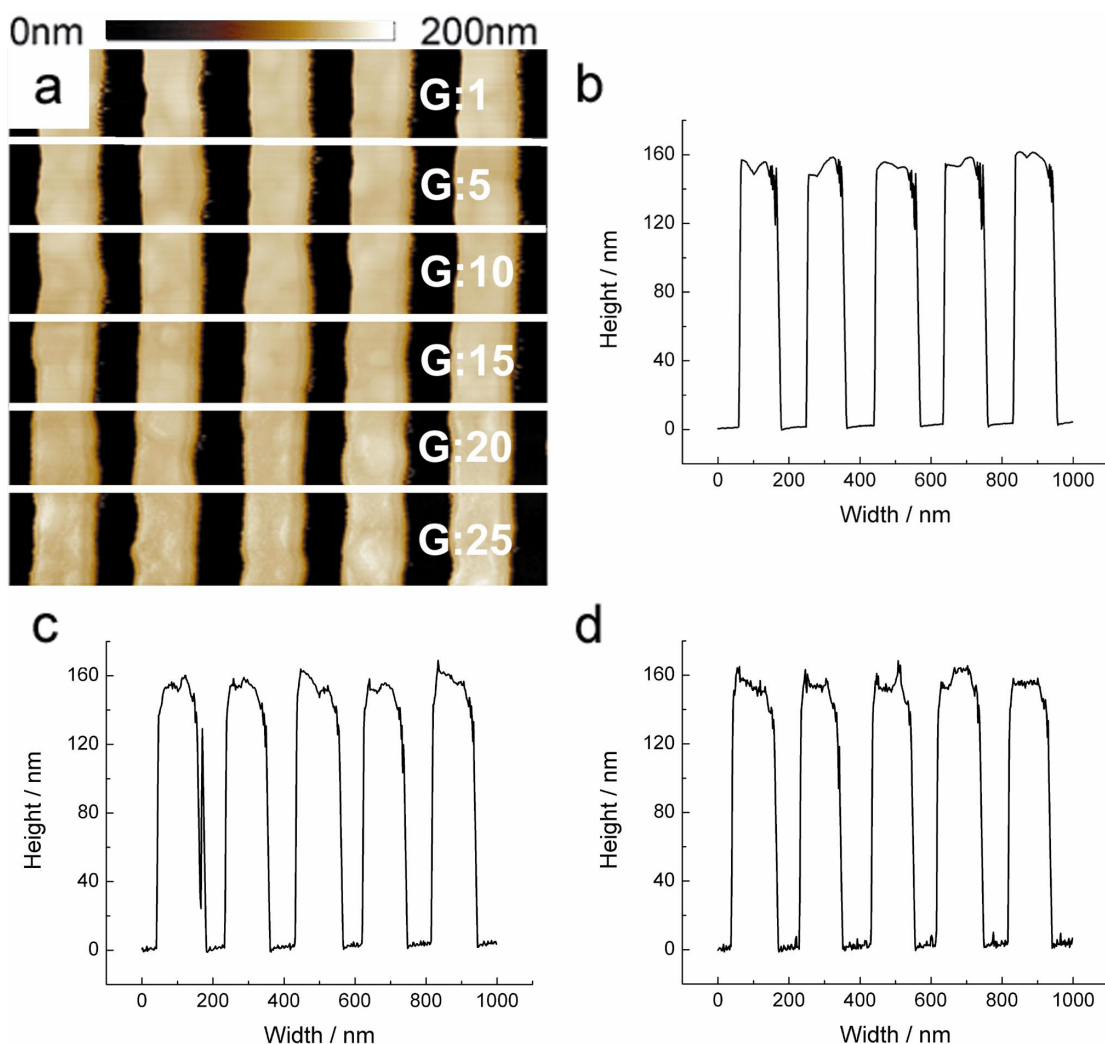


Figure 2.4. a) 1 x 1 μm AFM topography image of an optical scatterometry grating obtained with a CNT AFM tip at different feedback levels. At the top of the AFM scan feedback settings typical of a conventional Si AFM tip were used, resulting in ringing. The gain levels were increased at regular intervals indicated by white lines in (a) until the ringing artifact was eliminated. Cross-sectional line scans of the AFM data show the effect of changing proportional gain from 1 (b), to 10 (c) and then 20 (d).

conventional Si AFM tip, was used for the first section of the scan. As shown in the cross-sectional line scan (Fig. 2.4b) ringing occurred at nearly every vertical surface, and only started to diminish once the proportional gain reached values near 15 (Fig. 2.4c). At gain values approaching 20, the ringing was virtually eliminated (Fig. 2.4d). Once proper gain levels were determined for the CNT AFM tip, topography data of 60 nm trenches (Fig. 2.5a) was free of ringing, allowing accurate trench widths to be determined. In addition to revealing accurate trench widths, the phase data taken during the topographical scan clearly indicates when the CNT was in contact with the side of the trenches (Fig. 2.5b). Careful observation of the phase data as well as the cross-sectional data (Fig. 2.5c) indicates that the CNT used for interrogating the vertical sidewall was slightly misaligned by ca 5 degrees. We have found that our CNT AFM tips are very resilient and possess excellent wear characteristics in comparison to commercial Si AFM probes. As shown in Figure 2.5d, the CNT AFM tip remains intact even after repeated use of over 10 h. To date, we have demonstrated fabrication of hundreds of CNT tips possessing diameters as small as 3 nm and no larger than 20 nm with lengths ranging from 50 nm to 3 μ m and CNT tip compensation angles of 0° to 20°. The CNT tips can be fabricated on metal coated Si AFM probes, n-doped Si AFM probes and sharpened W probes.

Using the optimized scanning parameters, a section of the scatterometry grating was chosen where portions of the grating features converge due to limitations in

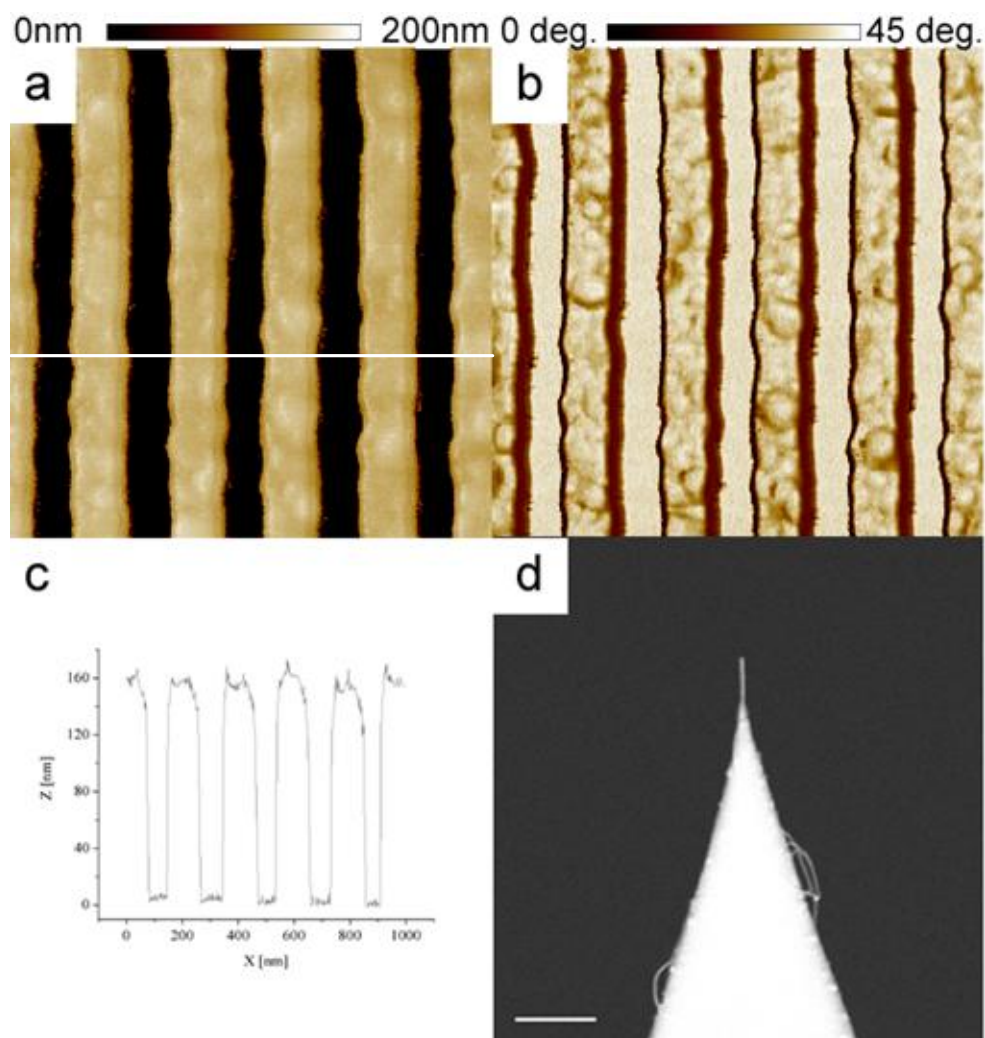


Figure 2.5. a) 1 x 1 μm AFM topography image of an optical scatterometry grating taken after optimum scanning parameters were determined to eliminate ringing. (b) Phase data of the AFM scan shows misalignment of the CNT AFM tip, resulting in a larger phase shift along the front side of each trench wall. (c) Cross-sectional line scan of the data depicted in Fig. 3a shows stable imaging of the vertical sidewalls. (d) SEM micrograph of the CNT AFM tip after repeated scanning of the scatterometry grating shows no change in the CNT alignment or length. Scale bar = 500 nm.

photolithography for creating such nanostructures (Fig. 2.6a). By imaging underdeveloped features of the grating, a minimum resolvable trench width could be determined by estimating when the CNT AFM tip could no longer contact the bottom of the trench. Phase data taken during the scan indicated successful imaging of the trench bottom with positive phase shifts (Fig. 2.6b), and cross-sectional line scans suggest that the minimum trench width resolvable with the CNT AFM tip was $\sim 33\text{nm}$ (Fig. 2.6c). The resolution limit for CNT AFM tips is dependant on many factors including CNT size, CNT misalignment and CNT instability, as well as Van der Waals interactions between the CNT and both sidewalls in the confined scanning space at the bottom of the trench. Steps toward reducing these factors would likely result in a lower resolution limit for high aspect ratio structures.

2.3.3 CNT STM Tip Characterization

As stated previously, using sharpened W wires to shorten CNT AFM tips simultaneously produces conductive CNT STM tips. While conventional W STM probes are capable of atomic resolution, their preparation in vacuum is time-consuming as it involves cycles of sputtering and annealing. Furthermore, when the tips are damaged they cannot be easily regenerated. Conductive CNT STM tips offer an alternative to this lengthy preparation, because the CNT tips may be easily regenerated by simply bringing the CNT into contact with a biased surface. Joule heating induced by contact with the biased surface effectively sharpens the CNT tip, thus enabling STM operators to

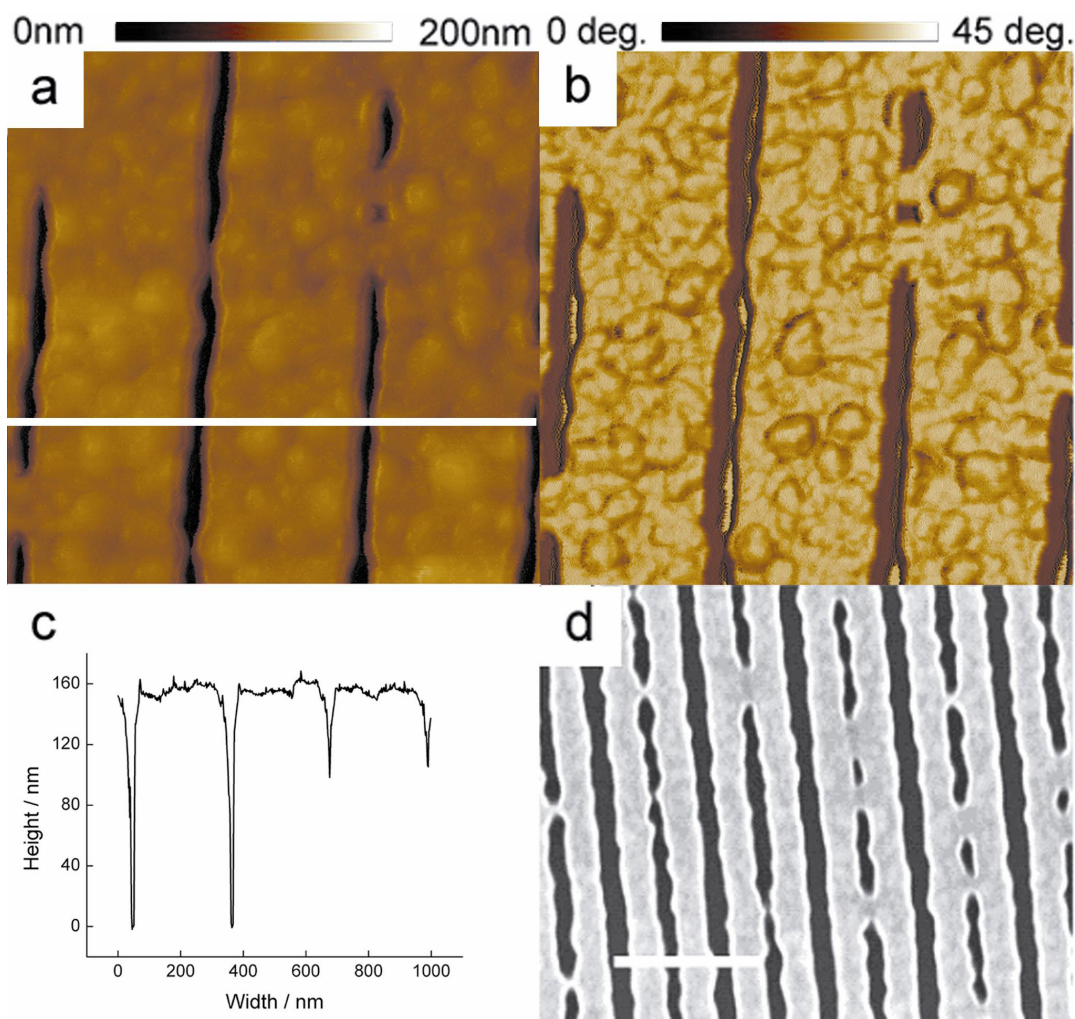


Figure 2.6. a) 1 x 1 μm AFM topography image of a scatterometry grating used to find the minimum measurable trench width when using a CNT AFM tip produced by this method. (b) Phase image of the area imaged in (a) shows contact with the bottom of the trench with a larger phase shift, thus clearly indicating successful imaging of the trench bottom. (c) A cross-sectional line scan taken at the indicated location on (a), showing the 33 nm minimum trench width measurable using the CNT AFM tip. (d) SEM micrograph of the scatterometry grating. The area was used because the grating lines converged, allowing observation of the exact trench width when the CNT no longer contacts the bottom. Scale bar = 1000nm.

efficiently regenerate probes without annealing or removing the tip.²¹

Several CNT STM tips produced by this method were used to interrogate the surface of highly-oriented pyrolytic graphite (HOPG), a common STM calibration standard. Two representative images show large-scale morphology (Fig. 2.7a) as well as atomically resolved structure (Fig. 2.7b) imaged with a CNT tip. An atomically resolved image obtained using an annealed W tip (Fig. 2.7c) is also included for comparison. Typically, somewhat higher resolution is obtained using the annealed W tip, but it lacks the reliability and robustness of the CNT STM tips. Cross-sectional linescans from both CNT STM and annealed W tips (bottom of Fig. 2.7b and 2.7c) reveal an atomic spacing of 2.45 Å between carbon atoms, similar to what is expected and observed by others.²⁴

To further evaluate the CNT STM tip performance, we have used a more complex substrate, rutile $\text{TiO}_2(110)$ (Fig. 2.8a). The $\text{TiO}_2(110)$ surface is composed of rows of topographically low lying Ti^{4+} ions and rows of topographically high lying bridge-bonded oxygen (BBO) ions along the [001] direction. In the empty state STM images, the low lying Ti^{4+} ions are imaged as protrusions, while the rows of BBO ions are imaged as depressions due to the inverse electronic contrast of these two ions.²⁵ The alternating Ti^{4+} - O^{2-} row periodicity of 0.65 nm is clearly visible in the 20 x 20nm images obtained using the CNT STM tip (Fig. 2.8b) and the annealed W tip (Fig. 2.8c). While row periodicity is clearly visible with both types of STM probes, neither provide resolution of individual Ti^{4+} ions within the rows. The highly ordered nature of $\text{TiO}_2(110)$, specifically

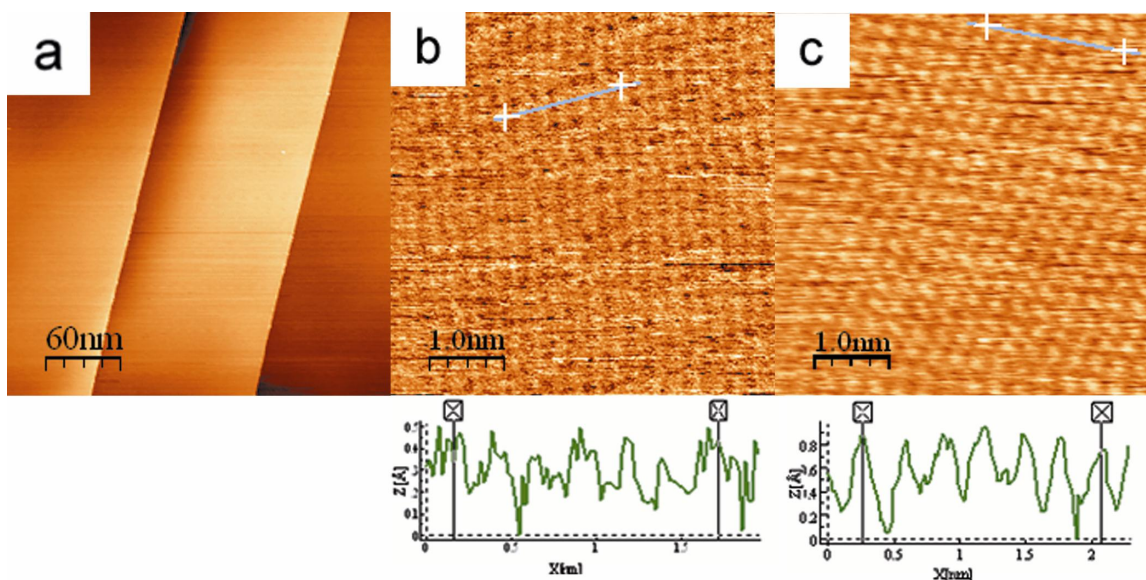


Figure 2.7. a) 300×300 nm STM image of freshly cleaved HOPG, showing step edges of the graphitic layers. (b) 5×5 nm STM image of the same sample, showing atomic resolution obtained with a CNT STM tip. (c) 5×5 nm STM image with good atomic resolution obtained with an annealed W STM tip. Cross-sectional line scans across the images on HOPG surface (bottom of (b) and (c)) show atomic spacing of 2.45 \AA obtained with both CNT STM and annealed W tips.

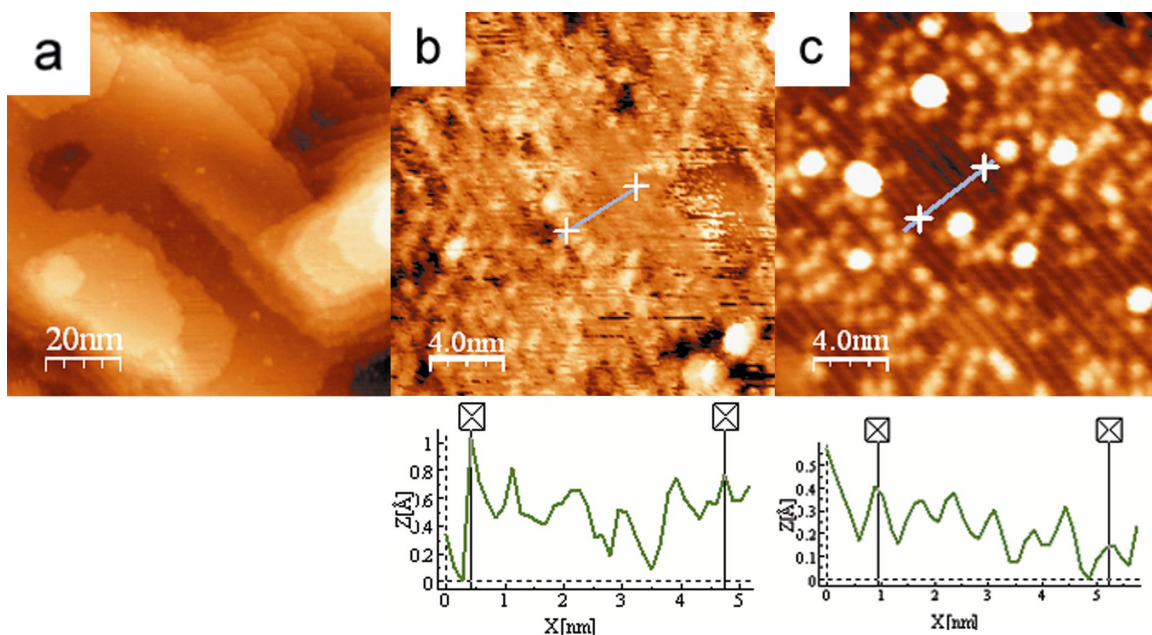


Figure 2.8 a) 100 x 100 nm STM image of TiO_2 (110) obtained using a CNT STM tip, demonstrating stability of the tip over larger scan sizes. (b) 20 x 20 nm STM image obtained using a CNT STM tip, showing clear row to row resolution as well as hydroxyl groups formed from water dissociation on oxygen vacancies in the bridging oxygen rows on the surface.²⁵ A cross-sectional line scan taken from (b) (below) shows accurate row to row spacing of 6.5 Å. (c) 20 x 20 nm STM image of TiO_2 taken with a conventional, well annealed W STM tip. A cross-sectional line scan taken from (c) (below) shows row to row spacing similar to that of a CNT STM tip, which agrees with literature values.²⁵

spacing between the rows of Ti^{4+} and O^{2-} ions, provides a good standard for evaluating CNT STM tips with STM. In addition to the row periodicity, isolated bright single-atom features are observed on the dark O^{2-} rows (Fig. 2.8c), which can also be used to evaluate the resolving capabilities of the CNT STM tips. These features are hydrogen atoms resulting from the hydroxylation of missing O^{2-} defects on partially reduced $\text{TiO}_2(110)$ surface from UHV background.²⁶

Typical large and small area images obtained with the CNT STM tips on $\text{TiO}_2(110)$ are shown in Fig. 2.8a and 2.b. In the atomically resolved image (Fig. 2.8b), the rows of Ti and O atoms are clearly visible, and a cross-sectional line scan reveals a row to row spacing of 0.65 nm, which agrees with previously reported values in the literature.²⁵ As with the annealed W tip (Fig. 2.8c), we were unable to resolve individual Ti^{4+} ions within the rows (Fig. 2.8b) using the CNT STM tip, but the individual hydroxyl groups are clearly visible and further demonstrate that subnanometer resolution can be obtained with the CNT-STM tips.

2.4 CONCLUSIONS

In this work, an efficient procedure was developed that successfully produces carbon nanotube AFM and STM tips using only a few steps. Following fabrication, instabilities due to CNT AFM tip-sample interactions were overcome by optimizing scanning parameters. Once these scanning parameters were established, a

high-aspect ratio standard was investigated to demonstrate resolution capabilities of the tips. Multiwalled CNT AFM tips were able to resolve 35 nm wide trenches that were 150 nm deep, but were hindered by slight misalignment of the CNT. The CNT STM tips were used to evaluate both TiO_2 (110) and HOPG calibration standards, and were shown to be capable of sub-nanometer resolution. While we were not yet capable of achieving “true” atomic resolution comparable to conventional STM tips, CNT STM tips have the capability of being easily regenerated, offering promise for repetitive, reproducible, long-term imaging studies. Future studies with conductive CNT AFM and CNT STM tips are planned to evaluate localized electronic, structural and compositional features in model electronic materials systems.

2.5 REFERENCES

1. Ukraintsev, V. A.; Baum, C.; Zhang, G.; Hill, C. L. The Role of AFM in Semiconductor Development: the 65nm Node and Beyond. *Proc of SPIE*. **2005**, 5752, 127-139
2. Barwich, V.; Bammerlin, M.; Baratoff, A.; Bennewitz, R.; Giggisberg, M.; Loppacher, C.; Pfeiffer, O.; Meyer, E.; Güntherodt, H.-J.; Salvétat, J. P.; Bonard, J.-M.; Forró, L. Carbon Nanotubes as Tips in Non-Contact SFM. *Appl. Surf. Sci.* **2000**, 157, 269-273.
3. Yu, M. F.; Dyer, M. J.; Skidmore, G. D.; Rohrs, H. W.; Lu, X. K.; Ausman, K. D.; Von Ehr, J. R.; Ruoff, R. S. Three-Dimensional Manipulation of Carbon Nanotubes Under a Scanning Electron Microscope. *Nanotechnology*. **1999**, 10, 244-252
4. Hafner, J. H.; Cheung, C. L.; Oosterkamp, T. H.; Lieber, C. M. High-Yield Assembly of Single-Walled Carbon Nanotube Tips for Scanning Probe Microscopies. *J. Phys. Chem. B* **2001**, 105, 743-746.
5. Tang, J.; Gao, B.; Geng, H.; Velev, O. D.; Qin, L. C.; Zhou, O. Assembly of 1D Nanostructures into Sub-Micrometer Diameter Fibrils with Controlled and Variable Length by Dielectrophoresis. *Adv. Mater.* **2003**, 15, 1352-1355.
6. Yasutake, M.; Watanabe, K.; Wakiyama, S.; Yamaoka, T. Critical Dimension Measurement Using New Scanning Mode and Aligned Carbon Nanotube Scanning Probe Microscope Tip. *Jpn. J. Appl. Phys.* **2006**, 45, 1970-1973.
7. Akita, S.; Nishijima, H.; Nakayama, Y.; Tokumasu, F.; Takeyasu, K. Carbon Nanotube Tips for a Scanning Probe Microscope: Their Fabrication and Properties. *J. Phys. D: Appl. Phys.* **1999**, 32, 1044-1048.
8. Hafner, J. H.; Cheung, C. L.; Lieber, C. M. Direct Growth of Single-Walled Scanning Probe Microscopy Tips. *J. Am. Chem. Soc.* **1999**, 121, 9750-9751.
9. Ye, Q.; Cassell, A. M.; Liu, H.; Chao, K. J.; Han, J.; Meyyappan, M. Large-Scale Fabrication of Carbon Nanotube Probe Tips for Atomic Force Microscopy Critical Dimension Imaging Applications. *Nano Lett.* **2004**, 4, 1301-1308.

10. Song, W. Y.; Jung, K. Y.; O, B. H.; Park, B. C. Accuracy Improvement of Protrusion Angle of Carbon Nanotube tips by Precision Multiaxis Nanomanipulator. *Rev. Sci. Instrum.* **2005**, 76, 025107 1-4.
11. Guo, L.; Liang, J.; Dong, S.; Xu, Z.; Zhao, Q. Property of Carbon Nanotube Tip for Surface Topography Characterization. *Appl. Surf. Sci.* **2004**, 228, 53-56.
12. Kazinczi, R.; Szöcs, E.; Kálmán, E.; Nagy, P. Novel Methods for Preparing EC STM Tips. *Appl. Phys. A.* **1998**, 66, S535-S538.
13. Iri, T.; Shiba, H.; Nishikawa, H. Observation of Surface Corrugation of Highly Oriented Pyrolytic Graphite by Scanning Tunneling Microscope in Air. *Jpn. J. Appl. Phys.* **1992**, 31, 1441-1445.
14. Shimizu, T.; Tokumoto, H.; Akita, S.; Nakayama, Y. Stable Atomic Imaging of Si(111)-7x7 Surface by Scanning Tunneling Microscope with Carbon Nanotube Tip. *Surf. Sci.* **2001**, 486, L455-L460.
15. Wongwiriyan, W.; Honda, S.; Mizuta, T.; Ohmori, T.; Murakami, T.; Kisoda, K.; Harima, H.; Lee, J. G.; Mori, H.; Oura, K.; Katayama, M. Direct Growth of Single-Walled Carbon Nanotubes on W Tip Apex. *Jpn. J. Appl. Phys.* **2006**, 45, 1880-1882.
16. Pasquini, A.; Picotto, G. B.; Pisani, M. STM Carbon Nanotube Tips Fabrication for Critical Dimension Measurements. *Sens. Actuators, A.* **2005**, 123-124, 655-659.
17. Tanaka, K.; Yoshimura, M.; Ueda, K. Fabrication and Growth of Carbon Nanotube Tips for Scanning Tunneling Microscopy by Direct Growth Using the Microwave Plasma-Enhanced Chemical Vapor Deposition. *e-J. Surf. Sci. Nanotech.* **2006**, 4, 276-279.
18. Yoshimura, M.; Jo, S.; Ueda, K. Fabrication of a Carbon Nanostructure onto the Apex of Scanning Tunneling Microscopy Probe by Chemical Vapor Deposition. *Jpn. J. Appl. Phys.* **2003**, 42, 4841-4843.
19. Nguyen, C. V.; Ye, Q.; Meyyappan, M. Carbon Nanotube Tips for Scanning Probe Microscopy: Fabrication and High Aspect Ratio Nanometrology. *Meas. Sci. Technol.* **2005**, 16, 2138-2146.

20. Yu, M. F.; Yakobson, B. I.; Ruoff, R. S. Controlled Sliding and Pullout of Nested Shells in Individual Multiwalled Carbon Nanotubes. *J. Phys. Chem. B* **2000**, *104*, 8764-8767.
21. Nguyen, C. V.; So, C.; Stevens, R. M.; Li, Y.; Delziet, L.; Sarrazin, P.; Meyyappan, M. High Lateral Resolution Imaging with Sharpened Tip of Multi-Walled Carbon Nanotube Scanning Probe. *J. Phys. Chem. B.* **2004**, *108*, 2816-2821.
22. Giannuzzi, L. A.; Drown, J. L.; Brown, S. R.; Irwin, R. B.; Stevie, F. A. Applications of the FIB Lift-Out Technique for TEM Specimen Preparation. *Microsc. Res. Techniq.* **1998**, *41*, 285-290.
23. Strus, M. C.; Raman, A.; Han, C. S.; Nguyen, C. V. Imaging Artefacts in Atomic Force Microscopy with Carbon Nanotube Tips. *Nanotechnology.* **2005**, *16*, 2482-2492.
24. Suzuki, Y.; Enoki, H.; Akiba, E. Observation of HOPG by STM and Contact AFM in Various Gas Atmospheres Under Pressures up to 1.1MPa. *Ultramicroscopy.* **2005**, *104*, 226-232.
25. Diebold, U. The Surface Science of Titanium Dioxide. *Surf. Sci. Rep.* **2003**, *48*, 53-229.
26. Zhang, Z.; Bondarchuk, O.; Kay, B. D.; White, J. M.; Dohnálek, Z. Imaging Water Dissociation on TiO₂ (110): Evidence for Inequivalent Germinate OH Groups. *J. Phys. Chem. B.* **2006**, *110*, 21840-21845.
27. I. Horcas, R. Fernandez, J.M. Gomez-Rodriguez, J. Colchero, J. Gomez-Herrero and A. M. Baro, WSXM: A Software for Scanning Probe Microscopy and a Tool for Nanotechnology. *Rev. Sci. Instrum.* **2007**, *78*, 013705 1-8.

CHAPTER 3

The Effect of Probe Length on AFM Phase Imaging

3.1 INTRODUCTION

As shown in chapter 2, high aspect ratio (HAR) probes enable metrology of complex geometries and nanoscale features, however the high aspect ratio nature of the probes causes interaction forces between the tip and surface (e.g. capillary, van der Waals) to be quite different from those of conventional probes. These forces are at work in every type of surface metrology, and must be understood before advanced probes such as carbon nanotube (CNT) atomic force microscopy (AFM) tips are readily utilized in AFM applications.¹ Specifically, further studies are needed to understand the role of tip geometry and tip composition on phase imaging in tapping mode AFM. During tapping mode AFM experiments, the oscillating tip experiences attractive and repulsive forces that shift the driving frequency of the cantilever oscillation. This perturbation is monitored as a shift in the phase of the driving frequency, and recorded along with the topography. Despite being used for studies in the determination of mechanical properties,² evaluation of nanoparticle-aerosol interactions,^{3,4} monitoring AFM tip power dissipation,⁵ the effect of AFM sample tilt upon phase shift,⁶ the study of nanoscopic

material domains,⁷ and phase based compositional mapping,⁸ Quantification and extrapolation of phase shift in relation to physical properties of the interrogated sample is not fully understood because of the complexity of the nanoscale interactions between the tip and the sample.⁹ These complex interactions have severely limited phase imaging for quantitative analysis, and further research is necessary to understand and enumerate the interactions between an AFM tip and a sample.¹⁰

A commonly observed effect in phase imaging is a dramatic shift between the attractive and repulsive regimes of the oscillating cantilever in tapping mode AFM.^{1, 10-15} In the attractive regime of the cantilever's motion, the predominating forces are described by equation 3.1:¹⁶

$$F_{ad} = F_c + F_{vdW} + F_E + F_B \quad (3.1)$$

where predominant adhesion forces (F_{ad}) include contributions from capillary forces (F_c),¹⁷ van der Waals forces (F_{vdW}),¹⁸ electrostatic forces (F_E), and chemical bonding forces (F_B). These forces combine to dampen the oscillation amplitude of the tip when it is far away from the surface, and as the tip continues its approach, their increasing tip to sample interaction forces causes further damping. As the mean height of the tip is reduced, it begins to make intermittent contact with the sample surface, which results in the emergence of repulsive forces because the probe begins to indent the sample surface

on its downward swing. These forces increase significantly when the mean height of the probe is reduced, and quickly overcome the attractive forces, leading to positive phase shifts and the so called “repulsive mode” of AFM imaging.¹⁹

With the addition of high aspect ratio structures such as carbon nanotubes and Pt spikes formed by e-beam lithography, the behavior and resulting phase images can change significantly to that observed for conventional AFM tips. In this chapter, the influence of modifying conventional Si-based AFM tips with high aspect ratio structures upon phase imaging characteristics is explored. We also discuss other benefits of utilizing HAR probes in phase imaging studies.

3.2 EXPERIMENTAL

High aspect ratio phase imaging probes were fabricated from Ti-Pt coated Si AFM tips (NSC15/Ti-Pt Mikromasch, 300 kHz) using electron beam induced deposition of a Pt organometallic, $(\text{CH}_3)_3\text{Pt}(\text{C}_6\text{H}_5)$. Precisely controlled Pt columnar structures (spikes) were deposited on the apex of the AFM tips by subjecting the adsorbed Pt compound to an electron beam (FEI DB235) in single spot scan mode. By confining the electron beam to a single location, the resulting Pt-C matrix grew toward the beam at a constant rate of $\sim 200\text{nm/s}$. This deposition rate allowed probes of precise dimensions to be fabricated in order to determine the effect of Pt spike length on phase imaging. Transmission electron microscopy (TEM) images were acquired with a JEOL 2010F

TEM, and energy dispersive spectrometry (EDS) data was acquired with an Oxford INCA Energy Dispersive Spectrometer.

Phase data was acquired with a Digital Instruments Bioscope interfaced with a Nanoscope IV controller operated in tapping mode. Scan rates were varied between 0.3 and 0.5 Hz, and the tapping mode amplitude was set at 1.0 V. Highly oriented pyrolytic graphite (HOPG) and doped Si wafers (100) were used as ultraflat test surfaces for phase imaging studies. Humidity studies were done in a homemade enclosure with humidity controlled by addition of N₂ gas to ambient conditions.

3.3 RESULTS AND DISCUSSION

3.3.1 The Behavior of High Aspect Ratio AFM Tips in Phase Imaging

In tapping mode AFM, a cantilever is oscillated at its harmonic frequency and lowered toward a surface so that it “taps” the surface at the lowest point of its oscillation. As it oscillates near the surface, attractive and repulsive forces interact with the probe causing the frequency of the oscillation to change with respect to the driving frequency. This shift in frequency is recorded by the AFM as a change in phase, and can be recorded simultaneously with topography images. Examples of this interaction are shown in Figure 1a and 1b, where a conventional AFM tip and a high aspect ratio Pt spike AFM tip with oscillation amplitudes of 1.0 V are lowered toward a Si (100) surface. At large tip-to-sample separations (i.e. the height of the tip at the center of the oscillation), there is no

observable change in the amplitude of the cantilever (Figs 3.1a, b) nor is there a noticeable phase shift in their respective phase response (Figs 3.1c, d). This indicates that there are no attractive or repulsive forces interacting with the probe. However, as the probe is brought closer to the surface, attractive forces begin to interact with the probe causing damping of the oscillation and a positive phase shift (i.e. attractive mode). While the tip continues to approach to the surface, the oscillating cantilever begins to make intermittent contact with the surface, which results in the onset of repulsive forces. In the case of conventional probes (Figs. 3.1a, c) these repulsive forces are often less intense than the attractive forces, causing the phase shift to remain higher than 90° . In the case of high aspect ratio AFM tips, the repulsive forces quickly become more intense than the attractive forces and the phase shift enters the repulsive mode (i.e. less than 90°).¹⁵ This transition also causes a shift in the amplitude of the oscillation because the tip becomes unstable due to probe response being dominated by attractive forces to repulsive forces.¹⁸

The location of this abrupt transition is typically overlooked because most probes used for phase imaging studies are conventional pyramid or cone-based AFM tips and often never enter the repulsive mode. However, when the geometry of the probes is changed, such as the CNT probes fabricated in chapter 2, the transition point from attractive to repulsive mode varies considerably. As a result of this, phase images are very different when acquired with conventional probes (Figs 3.2a, b) versus HAR probes (Figs 3.2c, d).

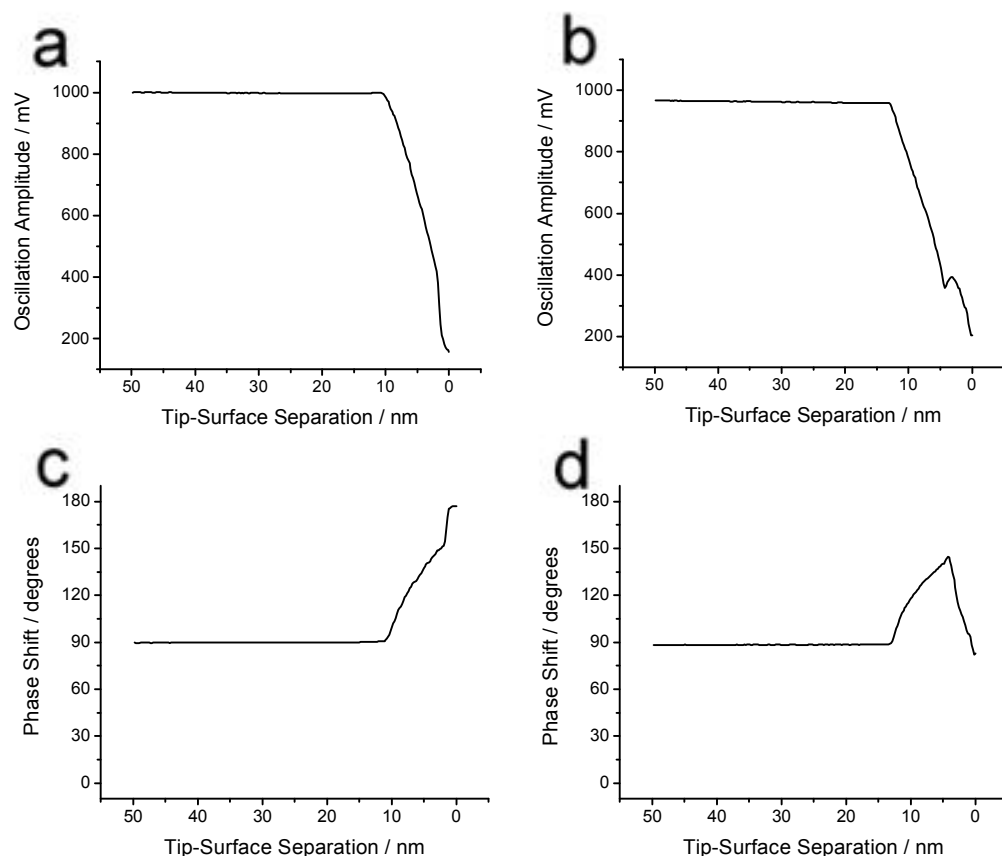


Figure 3.1. a) Graph of the effect of tip-to-sample separation on the oscillation amplitude of a conventional AFM tip and a high aspect ratio AFM tip (b) on Si (100). c) Graph of the phase shift of the conventional AFM tip shown in (a), which is dominated by attractive forces (phase shift $>90^\circ$) throughout the approach curve. d) The phase shift for a high aspect ratio AFM tip enters the attractive mode similar to the conventional probe shown in (c), but repulsive forces due to intermittent contact between the tip and the surface become more intense than the attractive forces, sending the tip into the repulsive mode (phase shifts $<90^\circ$).

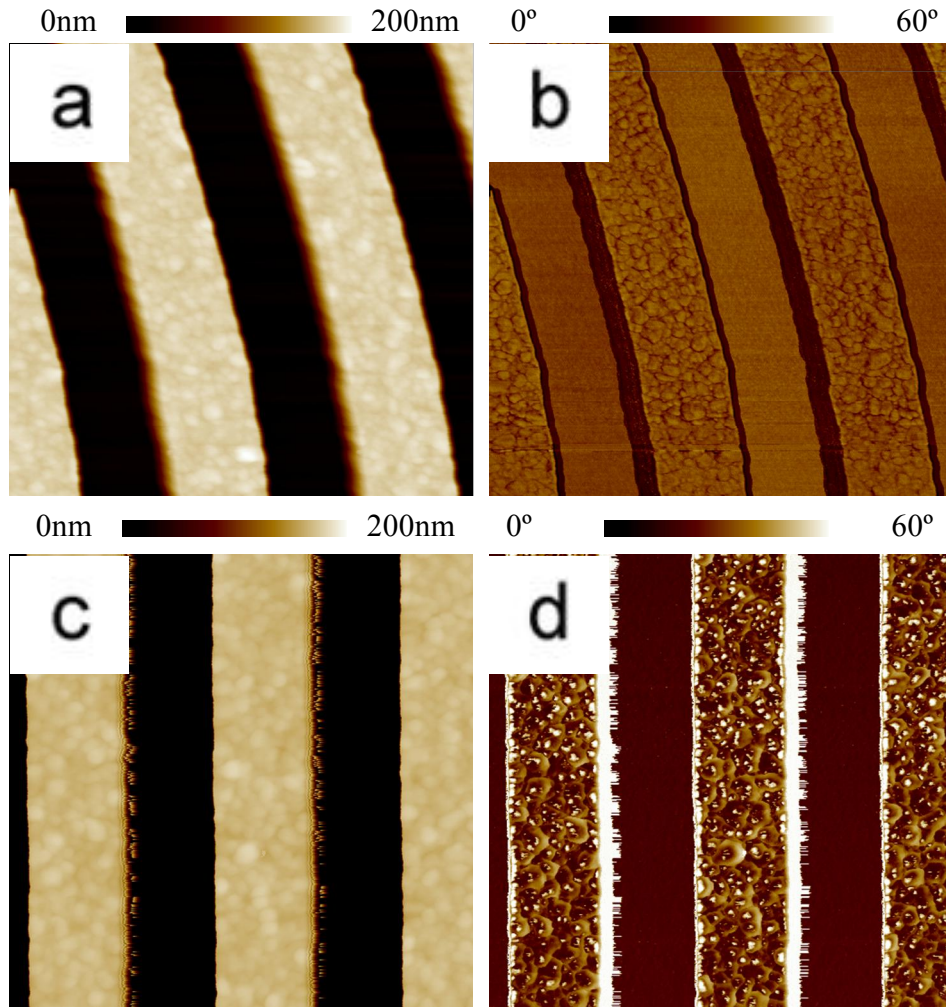


Figure 3.2 a) Topography AFM image of an optical scatterometry grating acquired with a conventional SiO₂ AFM tip. b) Phase contrast image of the grating shown in (a). c) Topography image of the grating shown in (a) acquired with a HAR Pt spike AFM tip. d) The phase contrast image shows much higher sensitivity than the image acquired with the conventional SiO₂ AFM tip. All images 1.8 x 1.8μm.

3.3.2 Pt Probe Fabrication

To show the effect of probe geometry on phase imaging, HAR probes were fabricated by electron beam induced deposition (EBID) of a Pt organometallic, $(\text{CH}_3)_3\text{Pt}(\text{C}_p\text{CH}_3)$. Pt spike based probes were used in place of CNT AFM probes because they are easier to produce and the length is easier to control, charging is minimized because they are more conductive, and their rigid structure simplifies data interpretation. To produce HAR Pt spike tips a conventional Pt coated AFM tip was placed in an electron microscope, where the Pt organometallic was vaporized and guided to the apex by a heated capillary. After leaving the capillary, the vaporized material adsorbed to the apex of the AFM tip, where it was deposited on the apex by exposing the material to an electron beam in spot-scan mode (Fig 3.3a). The resulting Pt spike had a radius of 15nm at the base, with a smaller radius of 7nm at the conical apex (Fig 3.3b). Additionally we found that complex structures could be formed by additional exposures after changing the orientation of the tip (Fig 3.3c) relative to the e-beam and capillary position. TEM images showed that the Pt spikes deposited as a Pt-C matrix rather than pure Pt (Fig 3.3d), as EDS data acquired during the TEM studies showed that the Pt-C matrix was 99.1 ± 0.6 wt% Pt (Fig 3.4a). The high Pt content of the Pt-C matrix had very little effect on the conductivity of the probe, since current-voltage (IV) curves of the Pt spike AFM tip were very similar to that of a Pt metal coated SiO_2 AFM tip (Fig 3.4b).

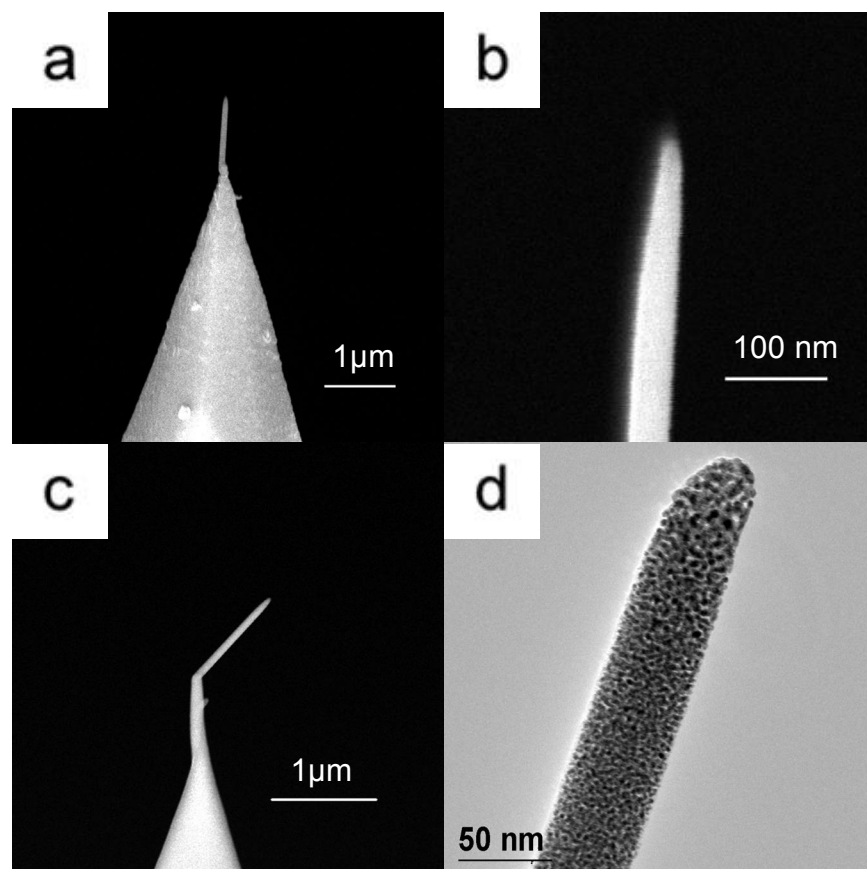


Figure 3.3. a) SEM micrograph of a high aspect ratio Pt probe fabricated by electron beam deposition of $(\text{CH}_3)_3\text{Pt}$ (C_pCH_3). By confining the SEM beam to a spot at the apex of the probe, a columnar structure 30nm in diameter can be formed. b) The resulting Pt spikes have conical apexes, with tip radii $<10\text{nm}$. c) By changing the orientation of the Pt spike, additional deposition steps allow formation of more complex structures. d) TEM images of the Pt spikes show that the resulting structures are not pure Pt metal, but a Pt-C matrix.

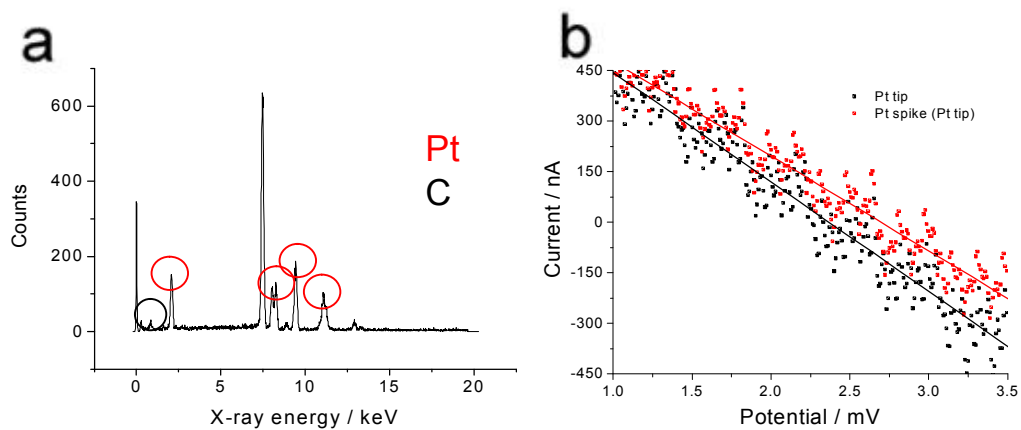


Figure 3.4 a) EDS spectra of a Pt spike shows that the deposition is not pure Pt metal, but a Pt-C matrix that is 99.1 ± 0.6 wt% Pt. b) Despite the small wt% C, IV curves indicate that the conductivity of a Pt spike AFM tip is very similar to that of a Pt metal coated AFM tip.

3.3.3 Effect of Pt Spike Length on Phase Shift

After the Pt spike AFM tips were produced, their effect on phase shift was determined by evaluating the probes of different lengths on clean Si wafer (100) and freshly cleaved HOPG. Each probe was scanned on the surfaces in ambient conditions at an amplitude setpoint of 0.7V to keep the tapping conditions constant between all of the probes. As shown in Figure 3.5, 0nm spikes, or Pt AFM tips coated with a thin layer of EBID deposited Pt, showed an average phase shift of 142° for Si and HOPG surfaces (amplitude setpoint ratio = 0.7), indicating that AFM tips with no high aspect ratio structure were strongly dominated by attractive forces. Addition of short HAR structures (<100nm) lowered the overall phase shift slightly, but were still dominated by attractive forces. Longer Pt spikes ($\geq 150\text{nm}$) resulted in phase shifts less than 90° , meaning that the interactions between the tip and surface were dominated by repulsive forces, though not as strong as the attractive forces acting on shorter HAR probes. Interestingly, extremely long probes did not show a significant increase in repulsive forces. The likely reason for this effect is that the attractive forces associated with the conical section of the AFM tip gradually decreased as the conical section was offset by the Pt spike, and once the spike length reached 150nm, the conical section no longer contributed to the attractive forces interacting with the tip. The interaction forces remained constant for longer probes because the geometry within 150nm was always similar for HAR probes longer than 150nm.

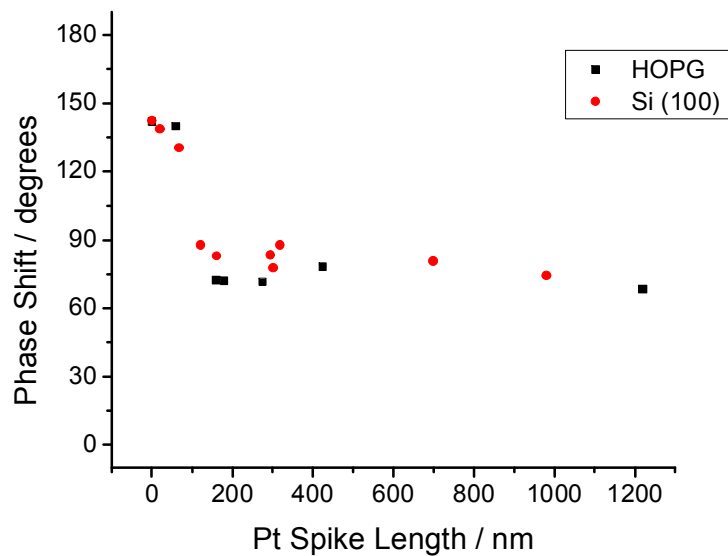


Figure 3.5. Average phase shift of Pt spike probes on HOPG (black squares) and Si (100) (red circles) as a function of Pt spike length. Short Pt spikes were dominated by strong attractive forces, resulting in phase shifts $>90^\circ$. Pt spike probes longer than $\sim 150\text{nm}$ were dominated by repulsive forces, indicating that the surface area of the conical section of the probe was the primary source of the strong attractive forces that caused the phase shifts to be higher than 90° in short Pt spike probes.

3.3.4 Quantification of Tip-To-Sample Forces

As stated previously, the forces that act on an AFM tip during imaging includes attractive forces such as capillary, van der Waals, electrostatic and chemical bonding forces, as well as repulsive forces from tip-sample contact. Because the Pt spike probes were produced from the same conductive material and had similar tip radii, van der Waals, electrostatic and chemical bonding forces should be the same from tip to tip. Additionally, because all the probes were scanned with the same tapping setpoints, the repulsive forces should remain constant between the probes. Capillary forces however, are very sensitive to surface area, which changes very dramatically with the addition of HAR structures such as Pt spikes and CNTs. Theoretical modeling is difficult however, as cone²⁰ and sphere^{16, 21} based models have been proposed to elucidate the attractive forces associated with capillary layers, but neither model adequately describes the system in the case of a high aspect ratio tip-to-sample interaction. Quantification of the overall forces is possible using the relationship between phase shift and tip-to-sample forces given by equation 3.2:¹⁰

$$\cos \Phi = 2 (F_{ts})/F_0 \quad (3.2)$$

where Φ is the measured phase angle and F_{ts} is the interaction force between the tip and the surface. F_0 is the driving force of the tip and is described by equation 3.3:¹⁰

$$F_0 = kA_0 / Q \quad (3.3)$$

where k is the cantilever force constant, A_0 is the oscillation amplitude and Q is the cantilever quality factor. Combining and rearranging equations 2 and 3 results in equation 3.4:

$$F_{ts} = \cos\Phi kA_0/2Q \quad (3.4)$$

By converting the measured phase shifts to tip-to-sample forces using equation 3.4, the attractive forces that interact with the conical section of the probe can be calculated. Figure 3.6 shows average phase data acquired with varying Pt spike lengths (black line) and the calculated tip-to-sample force of the interaction (blue line) on HOPG. Pt spike probes of 0nm show a tip-to-sample force of -0.6nN, which is due to the attractive forces listed in equation 3.1 as well as repulsive forces associated with intermittent contact between the tip and the surface. Pt spike probes longer than ~150nm show repulsive forces of 0.2nN, which indicates that an attractive force of 0.8nN was removed from the system when the conical section of the probe was offset from the surface by the Pt spike section of the probe. As stated earlier, this difference in attractive force is likely due to capillary forces. It is most likely not due to differences in repulsive forces, as the tapping conditions were constant for all probes, nor is it due to van der Waals forces or

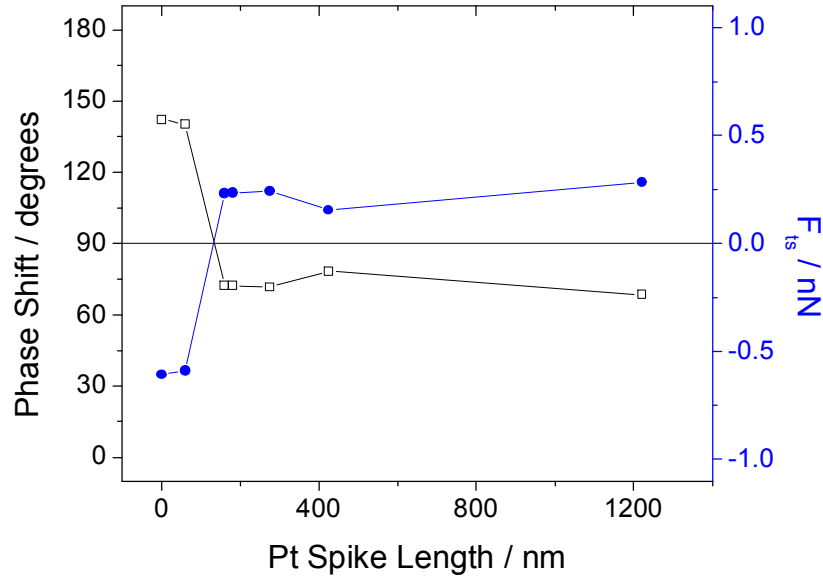


Figure 3.6. Average phase shift of Pt spike probes on HOPG as a function of spike length (black line) and the force exerted between the tip and surface due to attractive and repulsive forces (blue line). Pt spikes longer than 150nm experience 0.8nN more force than Pt spikes shorter than 150nm. This difference is due to attractive forces being minimized due to the conical section of the AFM tip being further from the surface while the tip makes intermittent contact.

electrostatic forces because the tip apexes were identical for all probes and the tip and sample surfaces were grounded.

3.3.5 Effect of Humidity on Pt Spike Phase Shifts

To further illustrate the effect of capillary forces on both high aspect ratio and conventional AFM tips, freshly cleaved HOPG was imaged with 0nm, 180nm, and 560nm Pt spike AFM tips while the humidity was varied (Fig 3.7). Each tip was scanned on HOPG at ambient conditions, and then N₂ gas was introduced into the imaging chamber to observe the effect of humidity on the measured phase shift. As expected, 0nm Pt spike tips showed a decrease in phase shift (i.e. decreasing attractive forces) of with reduction in humidity. As the humidity in the sample chamber decreased, the capillary layer thickness on the HOPG decreased, causing a reduction in phase shift of 25°. The 180nm and 560nm Pt spike tips showed no trends with humidity, and had average phase shifts of 90.4° and 77.4° respectively. While a slight reduction in phase shift would be expected for Pt spike tips, the magnitude and variation of the capillary force is expected to be quite low, and may not be resolvable with this detection scheme.

3.4 CONCLUSIONS

In conclusion, high aspect ratio probes are less susceptible to attractive forces than conventional cone and pyramid-based AFM tips. Experimental data indicates that the primary attractive forces that effect phase imaging in ambient conditions are capillary

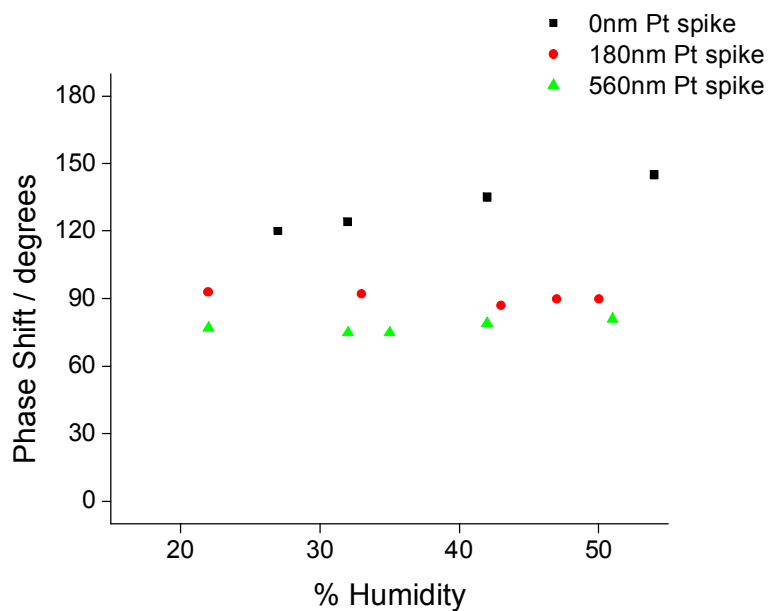


Figure 3.7 Graph of the effect of humidity on phase shift of 0nm, 180nm, and 560nm Pt spike AFM tips. As expected, the 0nm Pt spike had a reduction in phase shift with decreased humidity, indicating that capillary forces are the primary attractive forces for large tip geometries. Addition of a high aspect ratio structure (180nm and 560nm Pt spikes) reduces the surface area near the sample surface, which results in a decrease in capillary forces. As a result, the capillary forces are so small that humidity variations have no resolvable effect on the phase shift.

forces, and the addition of high aspect ratio structures such as Pt spikes or CNTs reduce these forces significantly. This is advantageous for phase imaging because high contrast phase images require imaging conditions to be carefully chosen so the phase shifts associated with different materials fall near the transition point between the attractive and repulsive modes of the tip.²²

Conventional AFM tips are more susceptible to capillary forces causing the attractive-repulsive transition to occur only with harsh imaging conditions (i.e. hard tapping), which may not be suitable for all materials.⁷ The reduced capillary forces associated with high aspect ratio tips cause the transition from attractive mode to repulsive mode to occur with light tapping conditions, making high contrast phase imaging more suitable for fragile samples. Future work will address the possibility that the decreased attractive forces on the tip effect resolution capabilities of the probes.

3.5 REFERENCES

1. Lee, S. I.; Howell, S. W.; Raman, A.; Reifenberger, R.; Nguyen, C. V.; Meyyappan, M. Nonlinear Tapping Dynamics of Multi-Walled Carbon Nanotube Tipped Atomic Force Microcantilevers. *Nanotechnology* **2004**, *15*, 416-421.
2. Ye, J.; Kano, M.; Yasuda, Y. Determination of Nanostructures and Mechanical Properties on the Surface of Molybdenum Dithiocarbamate and Zinc Dialkyl-Dithiophosphate Tribochemical Reacted Films Using Atomic Force Microscope Phase Imaging Technique. *J. Appl. Phys.* **2003**, *93*, 5113-5117.
3. Dong, R.; Yu, L. E. Investigation of Surface Changes of Nanoparticles Using TM-AFM Phase Imaging. *Environ. Sci. Technol.* **2003**, *37*, 2813-2819.
4. Schmitz, I.; Schreiner, M.; Friedbacher, G.; Grasserbauer, M. Phase Imaging as an Extension to Tapping Mode AFM for the Identification of Material Properties on Humidity-Sensitive Surfaces. *Appl. Surf. Sci.* **1997**, *115*, 190-198.
5. Balantekin, M.; Atalar, A. Power Dissipation Analysis in Tapping-Mode Atomic Force Microscopy. *Phys Rev. B.* **2003**, *67*, 193404-1-193404-4.
6. D'Amato, M. J.; Marcus, M. S.; Eriksson, M. A.; Carpick, R. W. Phase Imaging and the Lever-Sample Tilt Angle in Dynamic Atomic Force Microscopy. *Appl. Phys. Lett.* **2004**, *85*, 4738-4740.
7. Pang, C. H.; Hing, P.; See, A. Application of Phase-Imaging Tapping-Mode Atomic-Force Microscopy to Investigate the Grain Growth and Surface Morphology of TiSi_2 . *J. Vac. Sci. Technol. B.* **2002**, *20*, 1866-1869.
8. Rodriguez, T. R.; Garcia, R. Compositional Mapping of Surfaces in Atomic Force Microscopy by Excitation of the Second Normal Mode of the Microcantilever. *Appl. Phys. Lett.* **2004**, *84*, 449-451.
9. San Paulo, A.; Garcia, R. Unifying Theory of Tapping-Mode Atomic-Force Microscopy. *Phys. Rev. B.* **2002**, *66*, 041406-1-041406-4.
10. Martinez, N.; Garcia, R. Measuring Phase Shifts and Energy Dissipation with Amplitude Modulation Atomic Force Microscopy. *Nanotechnology* **2006**, *17*, S167-S172.

11. Chen, X.; Davies, M. C.; Roberts, C. J.; Tendler, S. J. B.; Williams, P. M.; Davies, J.; Dawkes, A. C.; Edwards, J. C. Interpretation of Tapping Mode Atomic force Microcopy Data Using Amplitude-Phase-Distance Measurements. *Ultramicroscopy* **1998**, *75*, 171-181.
12. Tamayo, J.; Garcia, R. Effects of Elastic and Inelastic Interactions on Phase Contrast Images in Tapping-Mode Scanning Force Microscopy. *Appl. Phys. Lett.* **1997**, *16*, 2394-2396
13. Cleveland, J. P.; Anczykowski, B.; Schmid, A. E.; Elings, V. B. Energy Dissipation in Tapping-Mode Atomic Force Microscopy. *Appl. Phys. Lett.* **1998**, *72*, 2613-2615.
14. Behrend, O. P.; Odoni, L.; Loubet, J. L.; Burnham, N. A. Phase Imaging: Deep or Superficial? *Appl. Phys. Lett.* **1999**, *75*, 2551-2553.
15. Garcia, R.; San Paulo, A. Attractive and Repulsive Tip-Sample Interaction Regimes in Tapping-Mode Atomic Force Microscopy. *Phys. Rev. B.* **1999**, *60*, 4961-4967.
16. Xiao, X.; Qian, L. Investigation of Humidity-Dependent Capillary Force. *Langmuir* **2000**, *16*, 8153-8158.
17. Sirghi, L.; Nakagiri, N.; Sugisaki, K.; Sugimura, H.; Takai, O. Effect of Sample Topography on Adhesive Force in Atomic Force Spectroscopy Measurements in Air. *Langmuir* **2000**, *16*, 7796-7800.
18. Kühle, A.; Sørensen, A. H.; Bohr, J. Role of Attractive Forces in Tapping Tip Force Microscopy. *J. Appl. Phys.* **1997**, *81*, 6562-6569.
19. Whangbo, M. H.; Bar, G.; Brandsch, R. Description of Phase Imaging in Tapping Mode Atomic Force Microscopy by Harmonic Approximation. *Surf. Sci.* **1998**, *411*, L794-L801
20. Malotky, D. L.; Chaudhury, M. K. Investigation of Capillary Forces Using Atomic Force Microscopy. *Langmuir* **2001**, *17*, 7823-7829.

21. Heim, L. O.; Kappl, M.; Butt, H. J. Tilt of Atomic Force Microscope Cantilevers: Effect on Spring Constant and Adhesion Measurements. *Langmuir*. **2004**, *20*, 2760-2764.
22. Chen, X.; Davies, M. C.; Roberts, C. J.; Tendler, S. J. B.; Williams, P. M.; Burnham, N. A. Optimizing Phase Imaging Via Dynamic Force Curves. *Surf. Sci.* **2000**, *460*, 292-300.

CHAPTER 4

Effect of Probe Geometry on Scanning Surface Potential Atomic Force Microscopy

4.1 INTRODUCTION

Scanning surface potential microscopy (SSPM) is a noncontact AFM method that enables material differentiation¹ and electrical characterization² of sample surfaces based on surface potential differences due to work function differences or sample biasing. Because the technique relies on long range electrostatic forces and not a tunneling current like scanning tunneling microscopy (STM), nonconductive samples can be studied as well as conductive surfaces. This allows a variety of studies, such as measuring data bits on recordable media,³ resolving electrostatic potentials of semiconductor devices,⁴⁻⁶ and determining the molecular orientation of aryldiazonium cation modified indium tin oxide (ITO) electrodes.⁷

Although somewhat similar because they both rely on attractive forces due to potential differences between the probe and the surface, SSPM differs from Kelvin probe force microscopy (KFM) because the topography and surface potential scans are taken sequentially rather than simultaneously as in KFM.⁸ This difference allows for better lateral resolution in topographical data, as long range electrostatic forces due to potential

differences inherent to KFM cause topographical errors⁹⁻¹¹. SSPM is based on a two-step scan of the surface, the first being a topography scan in tapping mode, and the second being an interleave scan at a fixed distance (10nm) above the previous topography scan. In the interleave scan, the tip is not driven mechanically like the previous topography scan, but the tip is biased directly as shown in Equation 4.1:

$$V_{\text{tip}} = V_{\text{dc}} + V_{\text{ac}}\cos(\omega t) \quad (4.1)$$

where ω is the resonant frequency of the cantilever and V_{ac} is the driving voltage. If the surface potentials of the tip (V_{tip}) and surface (V_{s}) are different, capacitive forces (F_{cap}) cause tip deflection (Eq. 4.2).

$$F_{\text{cap}}(z) = \frac{1}{2} (V_{\text{tip}} - V_{\text{s}})^2 \delta C(z) / \delta z \quad (4.2)$$

By monitoring the first harmonic of the capacitive force that is dependant on tip geometry (Eq. 4.3), surface topography and tip to surface separation (z),

$$F_{\text{cap}}^1(z) = \delta C(z) / \delta z (V_{\text{dc}} - V_{\text{s}}) V_{\text{ac}} \quad (4.3)$$

the AFM controller nullifies the capacitive force by varying the DC bias (V_{dc}) applied to the tip until the tip to surface potential difference is eliminated. Mapping this nulling potential allows formation of a surface potential map can be acquired with complementary topographical data.⁸

While capable of sensing surface potential differences of less than 5mV,^{12, 13} the technique is limited by a lack of lateral spatial resolution. This lack of resolution is due to the geometry of the probes used for the measurement²; typically metal coated Si tapping mode AFM tips.¹⁴ These probes, while inexpensive, are not capable of accurately resolving nanoscale potential differences because of the large surface area of the tip and cantilever.^{6, 15} The large surface area causes different areas on the tip to experience different levels of attractive force, leading to contributions from not only the tip apex, but also from the sides of the tip and the cantilever. Additionally, because these structures are so large, they can also experience attractive forces from different materials, effectively producing a weighted average surface potential of the materials under the tip and cantilever.¹

High aspect ratio probes, such as carbon nanotube and Pt spike AFM tips, provide ideal solutions for this limiting factor because of their low contact surface area and high aspect ratio.^{16, 17} The effect of adding a high aspect ratio structure to a conventional SSPM tip, as well as the effect of modifying the tip base structure, will be described in this chapter. In addition to studies on the effect of probe geometry, several high

resolution standards were studied to determine the performance of conventional and modified SSPM tips.

4.2 EXPERIMENTAL

SSPM measurements were performed on a Digital Instruments Bioscope Atomic Force Microscope with a Nanoscope IV controller. Scan sizes were $1 \times 1 \mu\text{m}$, and the scan rate used was 1 Hz. The probes used for data collection were NSC15/Ti-Pt (Mikromasch) Pt coated AFM probes. Studies were done to determine the effect of the geometry of the probe, so several variants of the conventional probe were used. One such modification included the addition of a metallic partition, or spike, fabricated on the surface by electron beam induced deposition (EBID) of a Pt organometallic in an electron microscope (FEI DB235). In other studies, the effect of the cone angle was evaluated by reducing it via modification with a focused Ga ion beam (FEI DB235) with a 30keV beam energy and beam current of 20nA. Cone angles of the probes were reduced from 30° to 10° and tip radii (10nm) were unchanged.

For stable SSPM imaging, the samples were electrically contacted to the sample stage by conductive Cu tape to eliminate any charge buildup that would cause a surface potential shift. For studies evaluating the effect of interleave scan height, a Pt interdigitated electrode array (IDEA) (BAS Inc.) was connected to a custom designed bias switching circuit. The circuit was designed to apply a bias the electrodes only during

the interleave scan, as previous studies have shown that topography scans of biased surfaces can produce significant topographical errors as well as tip damage. For surface potential studies of Pt nanoparticles, 3nm Pt nanoparticles were formed by reducing Pt salts in solution with generation IV dendrimers¹⁸. The resulting dendrimer encapsulated nanoparticles were drop cast on doped Si wafers and heated to 200°C to burn off the dendrimer. For studies of well ordered nanoscale features, porous TiO₂ films were prepared on ITO, and gold was impregnated in the pores by electrophoretic migration.¹⁹

4.3 RESULTS AND DISCUSSION

4.3.1 High Aspect Ratio Probe Development

Previous studies have shown that conventional probes (Fig. 4.1a, conical or pyramidal) are not ideal for high resolution KFM and SSPM studies because of the high surface area of the tip structure.^{1, 2} SSPM relies on capacitive forces between the tip and the surface, and the large surface area of conventional probes results in contributions from not only the apex, but the sides of the tip and the cantilever. Conductive high aspect ratio probes were fabricated to determine if this problem could be reduced by significantly decreasing the surface area of the tip structure near the sample surface.

Using the fabrication procedure described in chapter 3, high aspect ratio Pt spike probes were fabricated by electron beam induced deposition (EBID) of a Pt organometallic, (CH₃)₃ Pt (C_pCH₃), on Pt coated AFM tips (Fig. 4.1b). As shown in

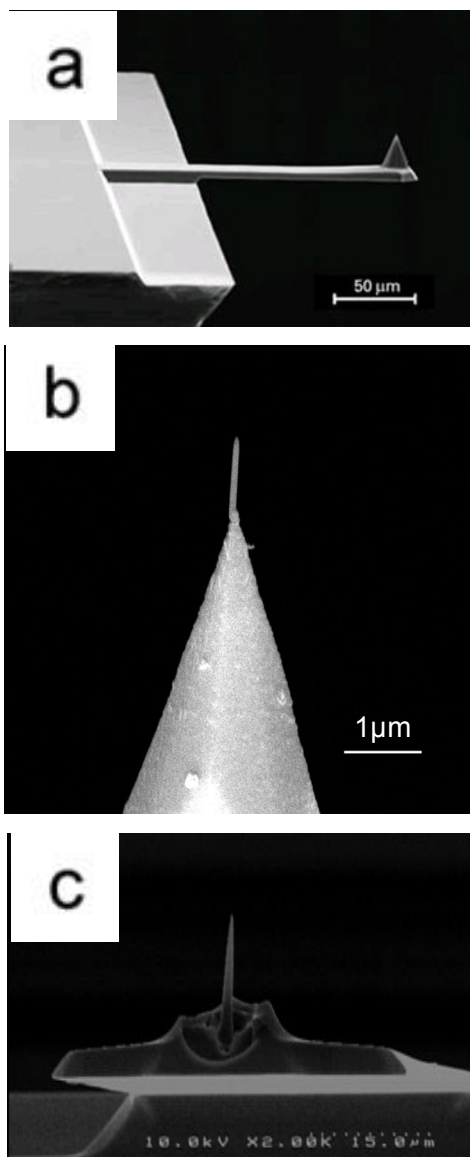


Figure 4.1 a) SEM micrograph of a conventional Pt coated AFM tip used for SSPM studies. b) SEM micrograph of a Pt spike AFM tip fabricated by electron beam induced deposition of a Pt organometallic. (7nm radius) c) SEM micrograph of a conventional Pt coated AFM tip that has been FIB milled to reduce the surface area of the tip structure while keeping the tip radius <20nm.

Chapter 3, the resulting Pt-C matrix formed a conductive structure (7nm radius) with resistance values similar to that of a conventional Pt coated AFM tip. To evaluate the effect of the surface area of a conventional tip, specifically the 30° cone angle of the tip, Pt coated probes were modified using a focused ion beam to reduce the cone angle to 10° while keeping a similar tip radius (<20nm) (Fig. 4.1c).

4.3.2 IDEA testing

To determine if either of the probe modifications influenced the measured surface potential with respect to conventional Pt coated AFM tips, the probes were used to scan an IDEA (Fig. 4.2). The alternating 10µm wide Pt electrodes, isolated by 5µm of glass, allowed different potentials to be applied to each set of electrodes while all other surface properties, such as the topography, remained constant. 50x50µm scans of the IDEA were acquired while potentials of 0, ±1, ±2, ±3, ±4, and ±5V DC were applied to the interdigitated electrodes (Fig. 4.3a). Special care was taken to only apply the bias during the interleave scan of the surface potential measurement, as probe failure due to significant potential differences between the probe and the surface during tapping mode have been observed (Fig. 4.3b). This required external circuitry that was built to turn on an external voltage source only when the probe was in the interleave mode.²⁰ As a result of the potential only being applied during the interleave scan, the topography scans were not adversely effected by electrostatic forces from large surface potential differences between the tip and the surface (Fig. 4.4a). Figure 4.4b shows that all three probes had

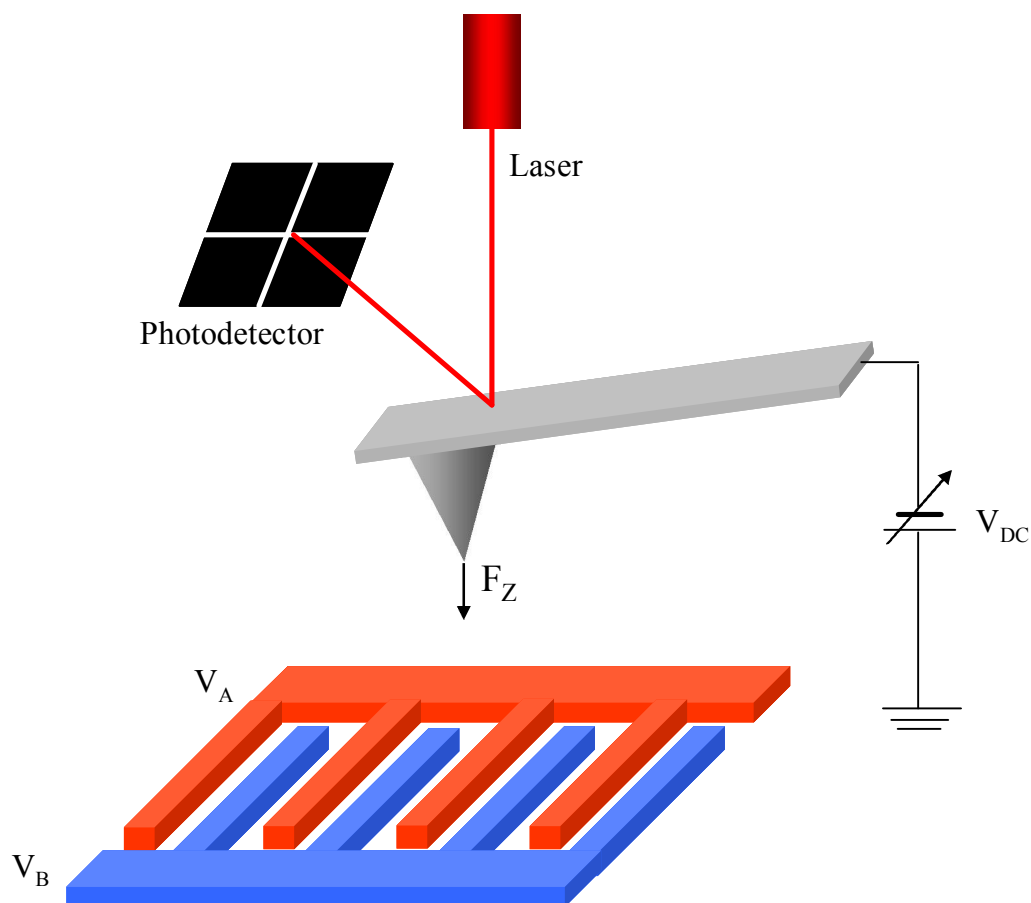


Figure 4.2: Schematic of a surface potential measurement on an interdigitated electrode array. The alternating electrodes allow different potentials (V_A and V_B) to be applied and measured by the tip while the surface topography remains constant. As the probe scans over the sample, the attractive forces due to the potential difference between the tip and the surface are eliminated by applying a bias to the tip that nulls the tip to surface potential difference.

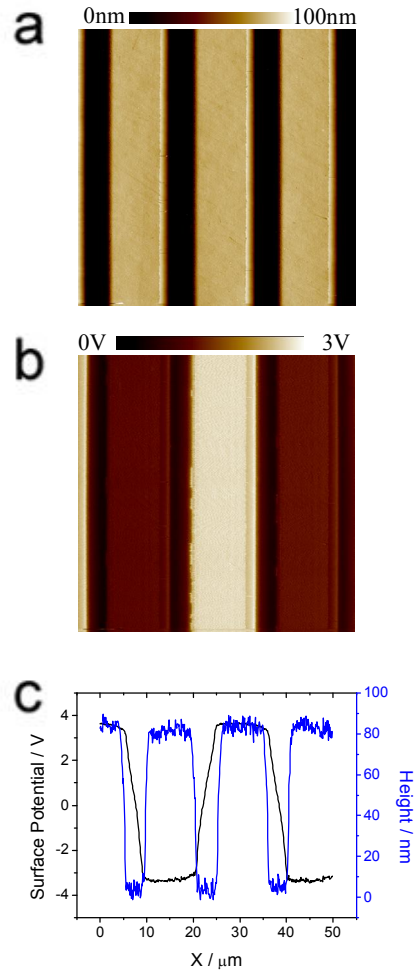


Figure 4.3. a) $50 \times 50 \mu\text{m}$ AFM topography image of an interdigitated electrode array used to evaluate the performance of high aspect ratio SSPM probes on biased surfaces. b) Surface potential data acquired during an interleave scan at 10nm above the surface shown area in (a) with applied potentials of $\pm 4\text{V}$. An external bias switching circuit was used so bias would only be applied during the interleave mode of the SSPM scan. c) Cross sections of the topography and surface potential data show the alternating potentials of the electrodes. All data acquired with a FIB milled conventional SSPM probe (tip radius $\leq 10\text{nm}$).

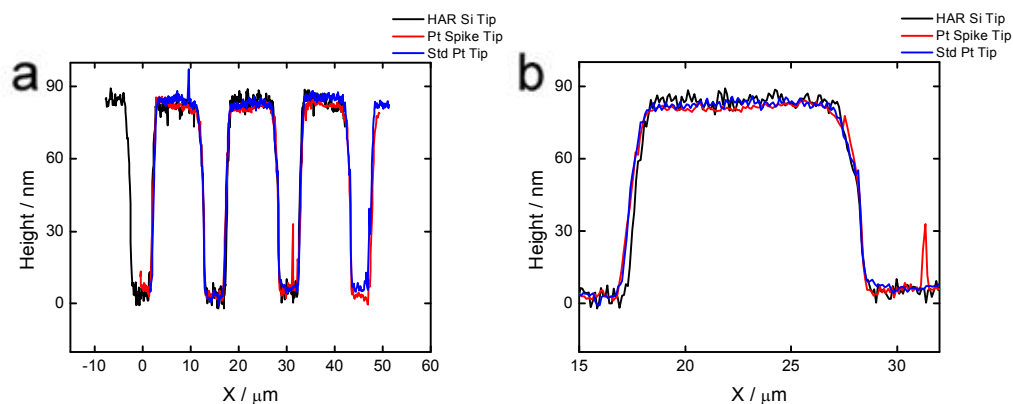


Figure 4.4 a) AFM topography image of the interdigitated electrode array shown in Figure 4.3a acquired with a conventional Pt coated tip, a Pt spike tip, and a FIB milled high aspect ratio Si tip. b) By applying the bias to the electrodes in the interleave scan and not the topography scan, accurate surface topography traces can be acquired with all three tips. The similar traces for all three probes ensure that there are no topographical effects (dissimilar interleave scans) in the surface potential data.

similar topography scans, which allows surface potential differences to be attributed to differences in tip geometry rather than from inaccurate interleaved traces. Surface potential traces were acquired for alternately biased electrodes for each probe: a conventional Pt coated probe (Fig. 4.5a, $\leq 40\text{nm}$ tip radius), a Pt spike tip (Fig. 4.5b, $\leq 10\text{nm}$ tip radius) and a high aspect ratio FIB milled AFM tip (Fig. 4.5c, $\leq 10\text{nm}$ tip radius). The resulting maximum potential differences for each probe (Fig. 4.6) indicate that significant surface potential averaging occurred for all three probes, as all three probes had measured potential errors of or exceeding 20%. These surface potential errors are likely due to a variety of factors such as contributions from the cantilever or the sides of the tip structure, which has been suggested to contribute to potential averaging in previous studies.¹ The tip that showed the most significant error between applied and measured potential was the FIB milled Si tip, which had errors of 30%. Because the probe was FIB milled, the tip height was decreased, causing greater interaction between the cantilever and the surface. While the height of the tip may have had an influence on the surface potential averaging, the dominant problem for the FIB milled tips was likely due to the Pt coating of the tip being removed during the FIB milling process. The removal of the conductive layer from the tip's surface results in IR drop between the apex of the tip and the cantilever, which lead to a systematic error in the measured surface potential. The Pt spike tip also showed increased potential error, though not as severe as the FIB milled probe. This error is likely due to the Pt coated tip structure under the Pt spike being raised

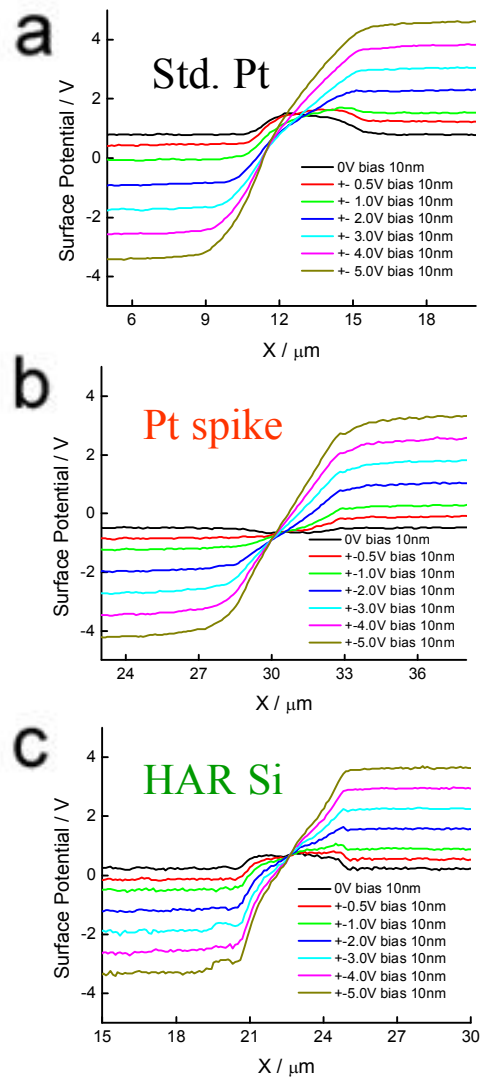


Figure 4.5 a) Surface potential linescans of the interdigitated electrode array (IDEA) shown in Figure 4.3a acquired at different bias levels with a conventional Pt coated SPM probe. Figures 4.5b and 4.5c show surface potential data acquired with a Pt spike and high aspect ratio Si tip, respectively.

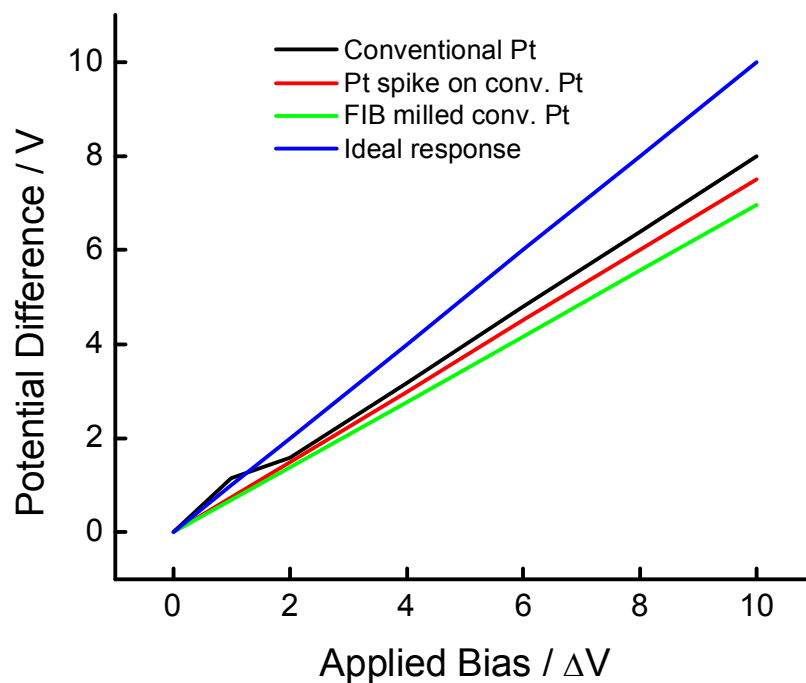


Figure 4.6 Graph of the potential difference measured with each SSPM probe with respect to the applied potential. All of the probes experienced surface potential averaging, which lead to a smaller measured surface potential than what was applied to the interdigitated electrodes.

higher above the surface, causing increased potential averaging.

To evaluate the effect of scan height on measured surface potential, the IDEA electrode was rescanned with each probe at a bias of $\pm 2\text{V}$ at heights of 10, 20, 50, 100, 200, 500, and 1000 nm as shown in Figure 4.7a, b, and c. Figure 4.8 shows the measured potential difference for each probe as a function of scan height. Pt spike AFM tips, like the conventional Pt coated Si probes, showed increased averaging with increased scan height. As shown in Figure 4.8, the relative error for Pt spike tips was worse than conventional tips at scan heights less than 500 nm, but showed less error at scan heights at or above 500 nm. This observation indicates that at distances greater than 500 nm the contribution of the conical section of the tip to averaging is minimized. Taking into account the length of the Pt spike (180 nm), the conical section of the tip must be lifted higher than 700 nm before the averaging from the tip will be reduced.

The FIB milled tip, similar to the data showed in Figure 4.6, showed the most error in measured potential, which is most likely due to the cantilever being less conductive. While this probe showed the highest error in both studies, it showed the most sensitivity at low potentials and scan heights. An example of this sensitivity can be seen in Figure 4.5c where the glass substrate that separates each electrode could be resolved and a stable surface potential could be acquired. This potential difference between the glass and the electrodes could also be seen in the conventional Pt tip scans, but the

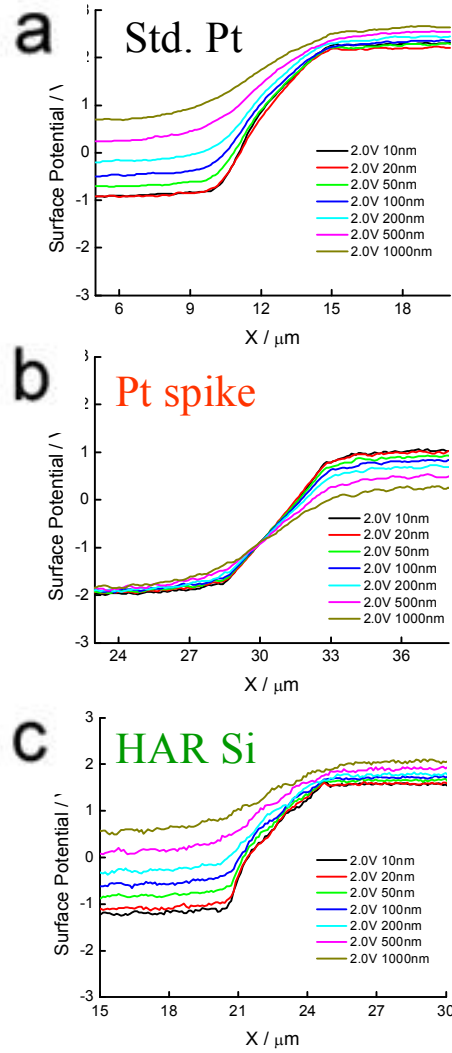


Figure 4.7 a) Graph of the effect of scan height on measured surface potential of a $\pm 2V$ DC interdigitated electrode array with a conventional Pt coated SSPM tip, a Pt spike tip (b) and a high aspect ratio FIB milled Si tip (c) Pt spike tips showed the least change in measured surface potential as a function of height, while high aspect ratio FIB milled tips showed sharper transitions at the interfaces of different materials (e.g. electrode to glass to electrode).

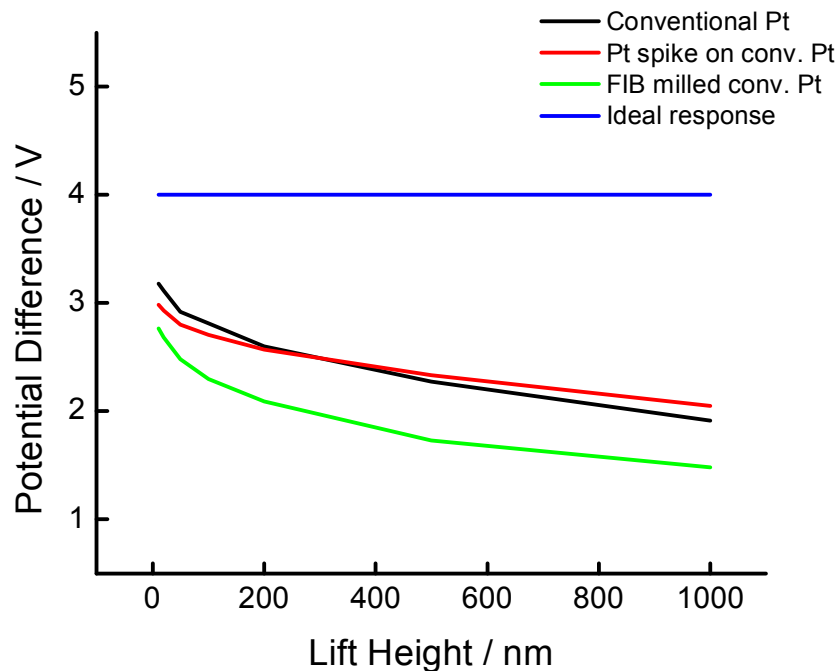


Figure 4.8 Graph of the measured potential difference between a -2V and +2V biased interdigitated electrode as a function of scan height. Data from all three probes indicate that none of the tips are capable of resolving the surface potential difference between the two electrodes of the IDEA, regardless of scan height. Pt spike tips, while less accurate than conventional tips at scan heights less than 300nm, are more accurate at large scan heights. High aspect ratio FIB milled Si tips are the least accurate of the three probes, though the probe shows the sharpest transition between surface potentials indicating high sensitivity.

contributions from averaging caused the tip to never acquire a stable surface potential for the substrate.

4.3.3 Effect of Tip Structure on Resolution of Pt Nanoparticles

To evaluate the effect of the conical section of the probe on surface potential sensitivity, Pt nanoparticles were dispersed on a Si wafer and imaged with a conventional Pt coated probe and a FIB milled probe. 3nm Pt dendrimer encapsulated nanoparticles were prepared by reduction of Pt salts in generation IV dendrimers. The resulting dendrimer solution was drop cast on a Si wafer and heated to 200C to remove the dendrimer from the nanoparticle. After removal of the dendrimer capsule, topography (Fig. 4.9a) and surface potential scans (Fig. 4.9b) with both the conventional and FIB milled probes revealed a clear difference in SSPM sensitivity. High aspect ratio FIB milled probes showed a surface potential difference of 62mV between the Si wafer and Pt nanoparticles (Fig. 4.9c). SSPM scans with conventional probes showed a surface potential difference of 20mV (Fig. 4.9d). The 40mV difference in measured surface potential for the different types of probes is likely the result of the difference in surface area of each probe. Conventional probes, having a significantly larger surface area than the FIB milled probes, have a larger capacitance resulting in more averaging of the Si and Pt surface potentials. Because the Si surface potential is less than the surface potential of the Pt nanoparticles, the measured surface potential of the Pt nanoparticle is reduced. Because the surface area of the HAR FIB milled tip was reduced, the FIB milled tips

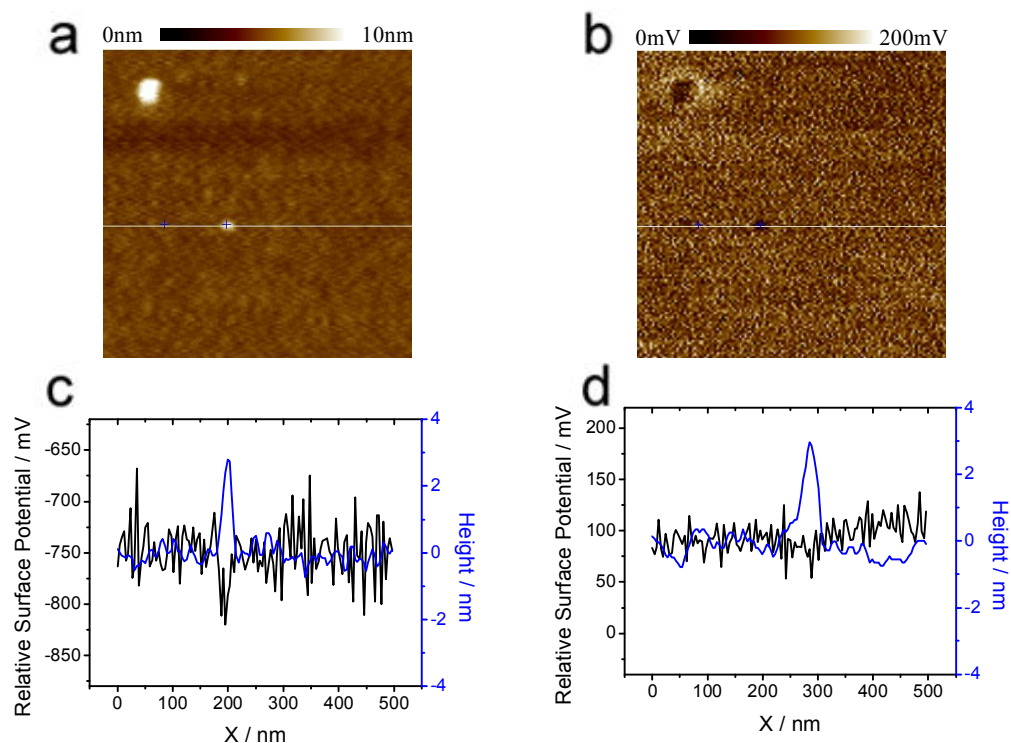


Figure 4.9. a) AFM topography image of a 3nm Pt nanoparticle on a Si wafer acquired with a HAR Si SSPM tip. b) Surface potential image taken of the same Pt nanoparticle. c) Graph of the topography and surface potential data of the Pt nanoparticle (indicated on a, b) indicated that HAR FIB milled Si tips can resolve a surface potential difference of 75mV between the Pt nanoparticle and the Si surface. d) Graph of topography and SSPM data acquired with a conventional Pt coated Si tip. The large surface area of the conventional probe resulted in greater surface potential averaging, which lead to a much smaller potential difference (<20mV) between the Pt nanoparticle and the Si surface.

measured a larger potential difference. While these probes provide a larger potential difference, the measured potential difference is significantly less than the difference in the work functions of the two materials of 1.1V.²¹ Because the measured potential was less than that of the work function difference, it is clear that the 3nm Pt nanoparticles are too small to be fully resolved with either probe, though the difference in potential indicates that the HAR FIB milled probes are capable of better surface potential resolution than conventional probes.

4.3.4 Mesoporous TiO₂ Studies

To further test the performance of high aspect ratio FIB milled SSPM tips verses conventional Pt coated SSPM tips, highly ordered porous TiO₂ surfaces were studied (Fig. 4.10a). The porous films, formed by surfactant templated calcinations,²² have hexagonally packed 10nm pores that were impregnated with 5nm Au nanoparticles by electrophoretic migration (Fig. 4.10b).¹⁹ Since the migration of the gold particles into the TiO₂ matrix depends on a strong electric field to drive the electrophoretic migration, surface potential experiments were carried out to determine if there was a potential drop across the nonconductive TiO₂ film (Fig. 4.11a). To determine this, the ITO substrate was connected to an external voltage source and biased at 0.0, 5.0, and 10.0V DC (Fig. 4.11b). Average measured surface potentials were within 1% of the applied bias, indicating that the substrate had a negligible effect in masking the applied bias (Fig. 4.11c). While measured surface potentials were similar to the applied bias on large scales,

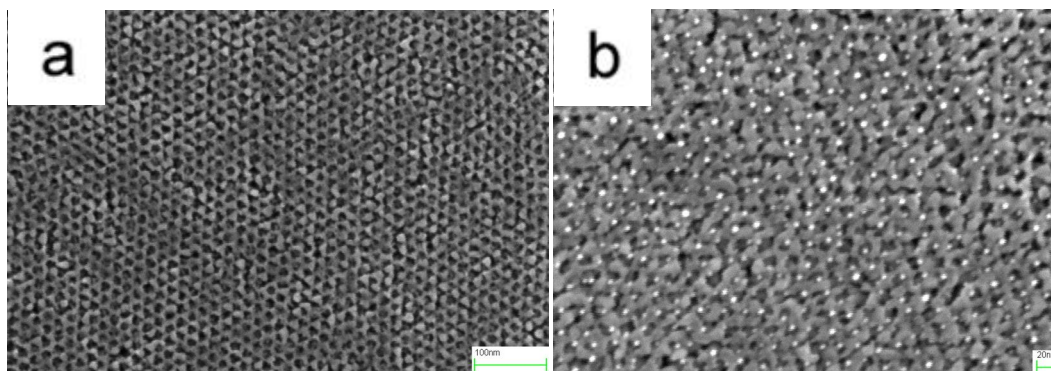


Figure 4.10 a) SEM micrograph of a mesoporous TiO_2 film deposited on an ITO electrode. The hexagonally packed pores (10nm) provide a well defined resolution standard for SSPM. b) Gold nanoparticles were added to the pores by electrophoretic migration and studied with SSPM.

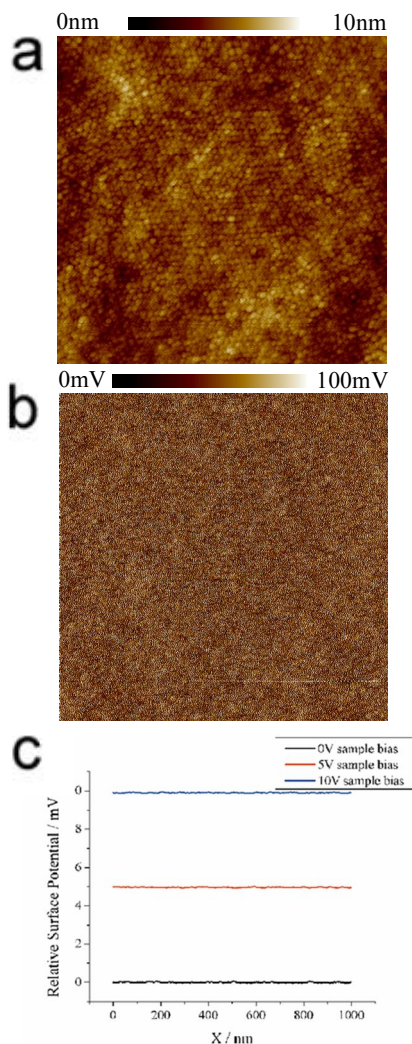


Figure 4.11 a). 1x1 micron topography image of the TiO_2 surface structure using a conventional Pt coated SSPM tip. b) SSPM image measured as a function of applied sample bias to the TiO_2 surface (0V, 5V, 10V DC). c) The measured surface potentials at 0, 5, and 10V DC indicated that the nonconductive nature of the TiO_2 film had very little effect on measured surface potential; however the porous framework of the TiO_2 could not be resolved in the SSPM image.

nanoscale potential differences could not be resolved with conventional Pt coated AFM tips. These potential differences, while very small in magnitude in comparison to the biases applied to the sample, are important to understand as they may have an effect on species migration at the surface. Determining potential differences on such small size scales is not possible with conventional probe geometries, because they have a cone angle of approximately 30° , which, as shown previously, leads to a large averaging effect in surface potential imaging. As has been shown in the Pt nanoparticles studies, high aspect ratio FIB milled AFM tips showed a significant increase in surface potential sensitivity. While the topographical resolution of the TiO_2 surface was very similar to that obtained with conventional Pt coated probes (Fig. 4.12a), surface potential sensitivity was drastically improved. The porous symmetry of the substrate was clearly visible in the surface potential scans, where measured surface potential differences between the pores and pore walls were typically 50mV (Fig. 4.12b). Linescans of the data showed that the pore sites seen in the topography scans (Fig. 4.12c) coincide with surface potentials as much as 90mV higher than that of TiO_2 that makes up the pore walls. The gold nanoparticles, having an inherently higher surface potential than TiO_2 because of their higher work function, are possible explanation for the higher surface potential within the pores. Arguments of topographical contributions to the surface potential measurements must be considered, though the structure of the pores is not cylindrical and likely results

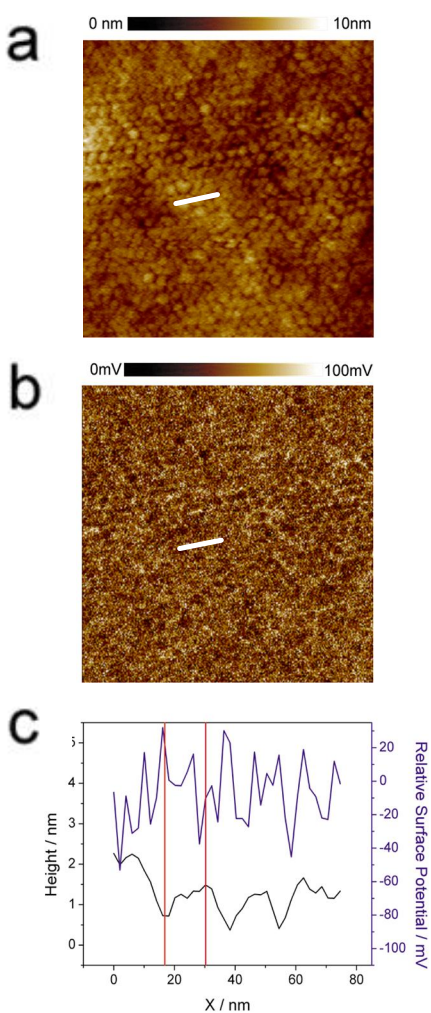


Figure 4.12 a) 500 x 500nm topography image of the porous TiO₂ substrate. b) 500 x 500nm surface potential image of (a) shows clear resolution of the porous structure. c) Data from the line indicated in (a) and (b) shows typical potential differences between the pore and the walls of the TiO₂ substrate. High aspect ratio FIB milled AFM tips showed potential differences between the pore and the TiO₂ substrate of 50mV.

in an effective void space near the surface of 10nm. This void space is unlikely to cause a significant change in surface potential, and would likely be averaged out by contributions from the cantilever.

4.4 CONCLUSIONS

Scanning surface potential microscopy is a versatile technique that allows nondestructive sample testing, and can reveal material composition differences as well as differences in sample biases. The technique can resolve very small differences in potentials, though the lateral resolution is limited by the probes used for the measurements. High aspect ratio probes such as CNT or Pt spike AFM tips have been shown to be a promising alternative to conventional Pt coated Si tips because they raise the tip and cantilever higher above the surface where their interactions with the surface will be minimized leading to less surface potential averaging. Additional studies have shown that reducing the surface area of the tip on conventional probes significantly increases the sensitivity of the technique to small surface potential differences. Future studies combining high aspect ratio structures to modified AFM tips could result in a drastic increase in lateral resolution, making this technique much more conducive to nanotechnology applications.

4.5 REFERENCES

1. Jacobs, H. O.; Knapp, H. F.; Müller, S.; Stemmer, A. Surface Potential Mapping: a Qualitative Material Contrast in SPM. *Ultramicroscopy*, **1997**, *69*, 39-49.
2. Lee, M.; Lee, W.; Prinz, F. B. Geometric Artefact Suppressed Surface Potential Measurements. *Nanotechnology*. **2006**, *17*, 3728-3733.
3. Chen, S. Y.; Hou, S. P.; Hsieh, J. H.; Chen, H. K.; Tsai, D. P. Writing and Erasing Efficiency Analysis on Optical Storage Media Using Scanning Potential Microscopy. *J. Vac. Sci. Technol. A*. **2006**, *24*, 2003-2007.
4. Koley, G.; Spencer, M. G.; Bhangale, H. R.; Cantilever Effects on the Measurement of Electrostatic Potentials by Scanning Kelvin Probe Microscopy. *Appl. Phys. Lett.* **2001**, *79*, 545-547.
5. Krtischil, A.; Dadgar, A.; Diez, A.; Krost, A. Electrical Characterization of Defect States in Local Conductivity Domains in ZnO:N,As Layers. *J. Mater. Res.* **2007**, *22*, 1775-1778.
6. Lee, J. S.; Ryu, S.; Yoo, K.; Choi, I. S.; Yun, W. S.; Kim, J. Origin of Gate Hysteresis in Carbon Nanotube Field-Effect Transistors. *J. Phys. Chem. C* **2007**, *111*, 12504-12507.
7. Maldonado, S.; Smith, T. J.; Williams, R. D.; Morin, S.; Barton, E.; Stevenson, K. J. Surface Modification of Indium Tin Oxide via Electrochemical Reduction of Aryldiazonium Cations. *Langmuir* **2006**, *22*, 2884-2891.
8. Kalinin, S. V.; Bonnell, D. A.; Local Potential and Polarization Screening on Ferroelectric Surfaces. *Phys. Rev. B* **2001**, *63*, 125411 1-13.
9. Jacobs, H. O.; Leuchtmann, P.; Homan, O. J.; Stemmer, A. Resolution and Contrast in Kelvin Probe Microscopy. *J. Appl. Phys.*, **1998**, *84*(3), 1168-1173.
10. Ono, S.; Takahashi, T. Intermittent Bias Application in Kelvin Probe Force Microscopy for Accurate Determination of Surface Potential. *Jap. J. Appl. Phys.* **2006**, *45*, 1931-1933.

11. Zerweck, U.; Loppacher, C.; Otto, T.; Grafström, S.; Eng, L. M. Accuracy and Resolution Limits of Kelvin Probe Force Microscopy. *Phys. Rev. B*, **2005**, *71*, 125424 1-9.
12. Sommerhalter, C.; Matthes, T. W.; Glatzel, T.; Jager-Waldau, A.; Lux-Steiner, M. C. High-Sensitivity Quantitative Kelvin Probe Microscopy by Noncontact Ultra-High-Vacuum Atomic Force Microscopy. *Appl. Phys. Lett.* **1999**, *75*, 286-288.
13. Liscio, A.; Palermo, V.; Gentilini, D.; Nolde, F.; Mullen, K.; Samori, P. Quantitative Measurement of the Local Surface Potential of π -Conjugated Nanostructures: A Kelvin Probe Force Microscopy Study. *Adv. Funct. Mater.* **2006**, *16*, 1407-1416.
14. Huang, H. S.; Cheng, H. M.; Lin, L. J. Coating Tips Used in Electrical Scanning Probe Microscopy with W and AuPd. *Appl. Surf. Sci.* **2005**, *252*, 2085-2091.
15. McMurray, H. N.; Williams, G. Probe Diameter and Probe-Specimen Distance Dependence in the Lateral Resolution of a Scanning Kelvin Probe. *J. Appl. Phys.* **2002**, *91*, 1673-1679
16. Wilson, N. R.; Macpherson, J. V. Enhanced Resolution Electric Force Microscopy with Single-Wall Carbon Nanotube Tips. *J. Appl. Phys.* **2004**, *96*, 3565-3567.
17. Wilson, N. R.; Cobden, D. H.; Macpherson, J. V. Single-Wall Carbon Nanotube Conducting Probe Tips. *J. Phys. Chem. B*. **2002**, *106*, 13102-13105.
18. Vijayaraghavan, G.; Stevenson, K. J. Synergistic Assembly of Dendrimer-Templated Platinum Catalysts on NitrogenDoped Carbon Nanotube Electrodes for Oxygen Reduction. *Langmuir* **2007**, *23(10)*, 5279-5282.
19. Patel, M. N.; Williams, R. D.; May, R. A.; Uchida, H.; Stevenson, K. J.; Johnston, K. P. Electrophoretic Deposition of Au Nanocrystals in Mesoporous Titania Thin Films. *Chem. Mater.* in preparation.
20. Smith, T. J. *Unpublished results*.
21. Lide, D. R. *CRC Handbook of Chemistry and Physics*; Taylor and Francis Group, LLC. : Oxford, **2007**.

22. Wu, C. W.; Ohsuna, T.; Kuwabara, M.; Kuroda, K. Formation of Highly Ordered Mesoporous Titania Films Consisting of Crystalline Nanopillars with Inverse Mesospace by Structural Transformation. *J. Am. Chem. Soc.* **2006**, *128*, 4544-4545.

CHAPTER 5

Fabrication of Specialized Probes for 3D AFM, NSOM, and Combined SECM-AFM

5.1 INTRODUCTION

Carbon nanotube (CNT) and Pt spike-based atomic force microscopy (AFM) tips have been shown to have significant advantages over conventional AFM tips because of their conductivity, nanoscopic sizes, and controllable aspect ratio. These properties have allowed existing techniques to be refined and advanced because they provide impetus to solve the limitations that exist for not only two-dimensional probe geometries and designs, but for three dimensional profiling applications as well. For instance, in chapter 2 carbon nanotubes were fabricated on conventional AFM tips to enable metrological profiling of high aspect ratio features that could not be studied with commercial AFM probes. Additionally, single CNTs were affixed to tungsten wires to enable scanning tunneling microscopy (STM) studies. Importantly, the CNT-STM tips are renewable and capable of high resolution imaging such as the atomic features and dimensions associated with single crystal TiO_2 and highly oriented pyrolytic graphite (HOPG). In chapters 3 and 4, it was shown that the addition of high aspect ratio structures result in increased sensitivity in AFM phase imaging, as well as increased resolution in scanning surface

potential microscopy (SSPM). While several examples of these limitations have been shown, many other metrology applications are limited by the geometry, composition, and structural arrangement of probes used to characterize surface properties.

5.1.1 Three-Dimensional Atomic Force Microscopy

One type of metrology that requires the use of high aspect ratio features to acquire high-resolution data is the interrogation of high aspect ratio features such as the 150nm x 40nm (depth x width) trenches shown in chapter 2 of this dissertation. While high aspect ratio AFM tips allow for precise topographical data to be obtained for nanoscopic surface features, they are still limited because they only collect data in two dimensions. This limitation is due to both the probe design and the scanning method used by conventional AFMs, because the probe is scanned at a fixed scan rate and raised or lowered depending on surface height fluctuations. While X, Y, and Z dimensions are all acquired by this scanning method, it does not yield true three-dimensional data plots, as the resulting images yield no data for the sides of high-aspect ratio height-to-width (e.g., steep-sidewall) structures being studied (Fig. 5.1a). True three-dimensional acquisition of data is important for assessing the roughness of the sidewall of a trench or for determining defects occurring at undercuts in photolithography masks.¹ Acquiring information of this nature requires at least six axial positional control of the AFM probe relative to the sample. This type of data cannot be acquired with conventional AFMs, and can only be

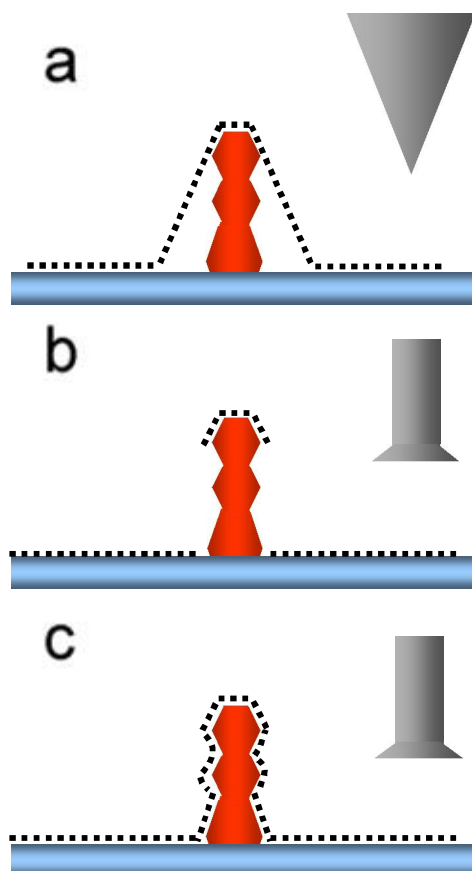


Figure 5.1. a) Scheme showing acquired surface profile (line scan) (dotted line) using a conventional AFM tip with a constant scan rate. The geometry of the tip is not capable of accurately reproducing the true morphology of the surface due to convolution of the probe tip dimensions with the interrogated feature. b) Resulting 2D profile obtained when a special “boot” tip is used with a conventional AFM at a constant scan rate. The high aspect ratio of the probe results in a better surface trace at the top of interrogated features, but the constant scan rate keeps the probe from imaging variations in the sidewall dimensions. c) Accurate surface profiles can be acquired with a “boot” tip when used with a 3D AFM, where an additional feedback loop allows variation of the scan rate as a function of Z .

obtained by altering the method of scanning since the data acquisition only uses three axes for positional control in addition to limitations associated with the probe tip features that are based on 2D profiling methods.

To attain true three-dimensional topography, advanced AFMs acquire data with different types of probes known as “boot” tips, which allow surface characterization of the sides of features, such as undercuts and sidewalls.^{2,3} While the high aspect ratio nature of the probe allows characterization of the corners of surface features, it cannot probe variations in sidewall features if it is limited to a constant scan rate, i.e., only one Z data point can be acquired for every X data point (Fig. 5.1b). To fully utilize the capabilities of the boot tips, 3D AFMs have an adaptive scan rate (otherwise known as rating and derating feedback correction parameters) that allows the probe to scan high aspect sidewall features as well as the features of in plane surfaces (Fig. 5.1c). While the combination of boot tips and adaptive scanning provide a method for characterization of 3D surfaces, the small extension of the probe (overhang) on commercially available boot tips,⁴ as well as the large overall probe diameter and wear induced errors^{1,5} limit the accuracy and precision of the measurement (i.e., accurate and precise mapping of true 3D features). We seek to develop Pt spike and CNT based 3D AFM probes as alternatives to existing Si based probes because of their small size, controllable geometry, and good wear characteristics. The development of these probes will enable interrogation of much smaller feature sizes than what is possible with commercially available probes, and the

high durability of the probes will enable more accurate dimensional metrology because the shape and dimensions of the probe will not change over the duration of experiments.

5.1.2 Near-Field Scanning Optical Microscopy

Another scanning probe technique that can be advanced by the processes described in the previous chapters is in the area of near field scanning optical microscopy (NSOM). Rather than using a Si-based probe for gathering surface information, NSOM typically uses a tapered optical fiber to map surface topography while simultaneously acquiring optical data with much higher resolution than is possible with standard optical microscopes. This increased optical resolution is possible because of the exploitation of near field optics.

As light waves pass through an aperture, the light waves diffract and form a diffraction pattern known as an “airy disk” pattern. This phenomena causes the resolution limit of optical microscopy to be roughly 2λ or two times the wavelength of the light source⁶ because when two features are within 2λ of each other, their diffraction patterns overlap causing loss of resolution in far field studies. In 1928, Synge proposed that the way to overcome this limitation was by imaging surfaces within $\sim 10\text{nm}$ of the aperture.⁷ At this short distance light does not diffract, and the diffraction limit is overcome. NSOM has now proven that this phenomenon can be exploited to perform high resolution imaging below the standard diffraction limit. NSOM is based on the scanning an optical aperture within $\sim 10\text{nm}$ of the surface to sample optical properties of the sample, and by

using feedback controlling electronics similar to that of conventional AFM designs, the tip can be dithered (oscillated) and raster scanned near the surface to acquire topographical data and optical data simultaneously.

As with AFM, the resolution limit of the topographical and optical resolution in NSOM is determined by the size of the probe,⁸ which itself has practical limits. Light waves pass through optical fiber with very little power loss because of total internal reflection, but if the end of the fiber is tapered, like the case of an NSOM fiber, the light can escape. This effect requires NSOM fibers to be coated with a thin layer of metal (>30nm) to confine the light until it reaches the aperture. Adding to the size restrictions, the aperture size of optical fiber based NSOM tips cannot be decreased below roughly 50nm. This is because power transmission is significantly reduced in probes with apertures < 50 nm, which results in a low signal to noise ratio.⁹ This lower limit of the aperture size, combined with the metal coating, results in a minimum probe diameter of 110nm, which is far too large for sufficient topographical resolution on most nanoscopic samples. Below we describe a strategy to circumvent issues associated with conventional NSOM probes.

5.1.3 Scanning Electrochemical Microscopy - Atomic Force Microscopy

Another method that requires further probe development is scanning electrochemical microscopy - atomic force microscopy (SECM-AFM). This hybrid scanning method allows surface topography and localized electrochemical data to be

acquired simultaneously by scanning and monitoring a biased ultramicroelectrode used as an AFM tip.¹⁰⁻¹² SECM resolution is dependant on electrode size and scan height, so combining the method with the highly controllable cantilever-based detection scheme of the AFM shows promise as a high resolution method for surface characterization.¹³ While the method shows promise, probe development has been slow due to the difficulties adding and properly insulating an electrode on an AFM tip.

Many examples of combined SECM-AFM tips have been proposed, but several difficulties with their preparation have limited their implementation. Most current methods are irreproducible and too time consuming, in addition to being too expensive. Furthermore, the influence of probe dimensions and characteristics on spatially resolved topographic and electrochemical data is difficult to model and experimentally evaluate. Most SECM-AFM probes that have been developed have been fabricated by depositing a metal layer on a conventional¹⁴ or custom fabricated AFM probes,¹⁵ then depositing an insulating material on the metal layer.^{13, 16} The insulating material can then removed by etching,¹⁷ focused ion beam milling,¹⁴ or heating.¹⁸ Of the probes that have been developed recently, high aspect ratio probes based on CNTs seem to be the most promising because of their conductivity and small electrode size. While promising, the probe designs are not ideal because of inexact removal of the insulator¹⁹ or because they do not fully utilize the small size and conductivity of the CNT.¹⁴ We believe the fabrication of CNT or metal-based SECM-AFM tips is essential to the advancement of

SECM-AFM metrology, and below we describe preliminary work that is underway that utilizes existing methods for fabricating these probes.

5.2 EXPERIMENTAL

5.2.1 3D AFM Probe Fabrication

3D AFM probes were fabricated by several methods, and many of the techniques used in fabrication have been described in previous chapters. Carbon nanotube-based 3D probes were fabricated with the electrical shortening technique outlined in chapter 2. Briefly, CNTs were grown on conventional AFM tips (BudgetSensors Tap300) by chemical vapor deposition of ethylene. The CNTs typically grew at the apex of the AFM tip, and were shortened by touching the CNT to an electrically biased W wire. When the current flow exceeded the capacity of the CNT, localized Joule heating resulted in failure near the center of the spanning segment of the CNT. To make the 3D AFM probes, the resultant segment of the CNT on the W wire was reattached to the main CNT in a different orientation and glued in place with electron beam induced deposition of C.

Pt based 3D AFM probes were fabricated by electron beam deposition of (Trimethyl)methylcyclopentadienylplatinum, similar to the method described in chapter 3. Conventional Si AFM tips (Mikromasch NSC15 Ti-Pt) were modified with focused ion beam milling (FEI DB235) to fabricate a vertically oriented base structure for the Pt spikes. This allowed vertical structures to be probed without the Si support contributing

to the trace. To fabricate the 3D Pt structures, an electron beam (FEI DB235) was set in spot scan mode and focused on the surface of the Si tip. Simple structures were produced by exposing the surface for short periods of time, while complex structures were produced by changing the orientation of the probe and depositing Pt in multiple steps. 2D AFM studies were conducted with a Digital Instruments Bioscope controlled by a Nanoscope IV controller. 3D AFM studies were conducted using a SXM AFM at Xidex Corp. in Austin, TX.

5.2.2 Pt Spike NSOM Fiber Fabrication

NSOM probes were fabricated from Fibercore SM750 optical fiber using a Sutter Instruments glass puller. The NSOM fibers were typically uniformly coated with 200nm of Al and FIB milled (FEI DB235) to reveal the aperture. After the aperture was revealed, a nanoscopic Pt dot was deposited on the aperture using electron beam deposition of (Trimethyl)methylcyclopentadienylplatinum. NSOM studies were conducted with a modified ThermoMicroscopes Aurora-2 NSOM on a Nikon Diaphot 300 inverted microscope. The scanner was a P-500 Series PZT Flexure Stage by Physik Instrument, and the probes were mounted on piezo-driven Accutune (95kHz) tuning forks from ThermoMicroscopes. Tom Doyle, of the Vanden Bout research group, fabricated the conventional optical fiber NSOM probes, and acquired all NSOM data shown herein.

5.2.3 SECM-AFM Probe Fabrication

Combined SECM-AFM probes were prepared by depositing Pt spikes on Pt coated AFM tips (Mikromasch NSC15 Ti-Pt) by electron beam induced deposition of (Trimethyl)methylcyclopentadienylplatinum (FEI DB235). After the Pt spikes were formed, the resulting tips were coated with Parylene N (Parylene Coating Services) in a home built parylene deposition chamber. After deposition of the parylene film, the apex of the Pt spike was exposed with FIB milling (FEI DB 235).

5.3 RESULTS AND CONCLUSIONS

5.3.1 Pt-based 3D AFM probes

Probes for three-dimensional AFMs have three major liabilities that limit the effectiveness and efficiency of the technique. The first limitation in probe designs for 3D AFMs is due to the amount of undercut that each tip can probe. Conventional boot tips are Si-based, and have a flared Si ridge at the base of a high aspect ratio Si column, and while this geometry is effective for many samples, the probes typically cannot measure undercuts in excess of 30nm (Fig. 5.2a). Ideally, 3D AFM tips should have the ability to probe much larger undercuts, and work has been started to accomplish this goal.

Utilizing methods developed in chapter 3, 3D AFM tips were fabricated that have much larger undercuts and better wear characteristics than Si boot tips. The probes were fabricated by FIB milling of conventional AFM tips to make high aspect ratio Si features

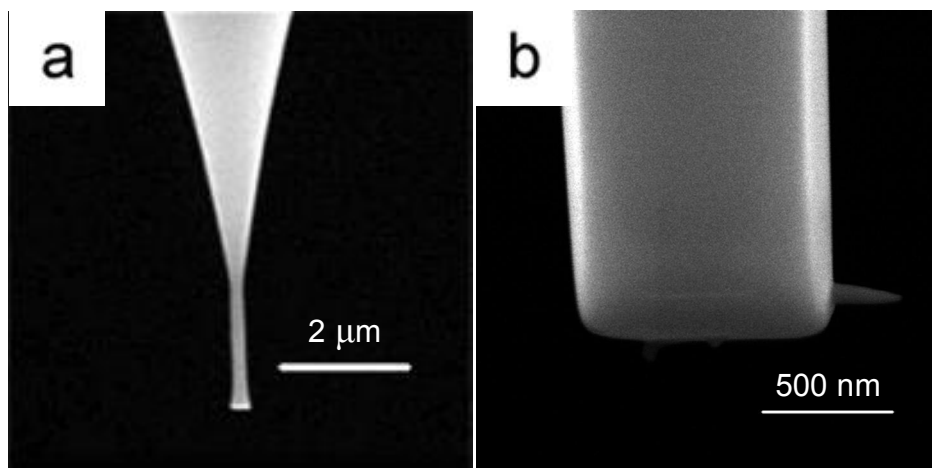


Figure 5.2 a) SEM image of a conventional Si based 3D “boot” AFM probe. Commercially available Si boot tips have a flared Si ridge at the base of the high aspect ratio Si support (100nm) that allows them to image sidewalls and undercuts of surfaces, but they can only measure undercuts less than 30nm. b) SEM image of a custom built 3D AFM probe using Pt EBID to form a well defined imaging surface capable of imaging much larger undercuts.

to act as the support structures for the Pt deposits. Once the Si column was fabricated, a small Pt spike was deposited on one side of the tip by electron beam induced deposition of Pt from the decomposition of (Trimethyl)methylcyclopentadienylplatinum (Fig. 5.2b). Once fabricated, the tip was used to interrogate a tip characterization standard to judge how much undercut the fabricated probe could measure vs. a conventional Si-based boot tip (Fig. 5.3a). As shown in Figure 5.3b, the Pt boot tip (Fig. 5.3c) was able to probe 350% deeper into the characterization standard than the Si boot tip (Fig. 5.3d), and the only limiting factor to the measurement was the length of the Pt spike. While the probe was able to interrogate much deeper into the undercut of the feature, the design needed to be optimized for more realistic sample geometries. The probe only had a Pt spike on one side, and the high aspect ratio Si support section was too large (700nm) to evaluate most high aspect ratio samples. While not very applicable for real-world samples, this type of probe shows that the addition of high aspect ratio structures allows much deeper undercuts to be imaged, though a much smaller base structure would be preferred.

To produce 3D AFM tips with smaller footprints, complex metal-based tips were fabricated using a multi-step deposition procedure where the tip and Pt organometallic was first exposed to a vertically oriented electron beam (Fig. 5.4a). As a result of the electron beam exposure, a highly controlled vertical Pt column was deposited on the apex of the Si AFM tip. The tip was then reoriented in the SEM and the beam was exposed on the apex of the Pt column at a slight angle to form a complex three-dimensional Pt

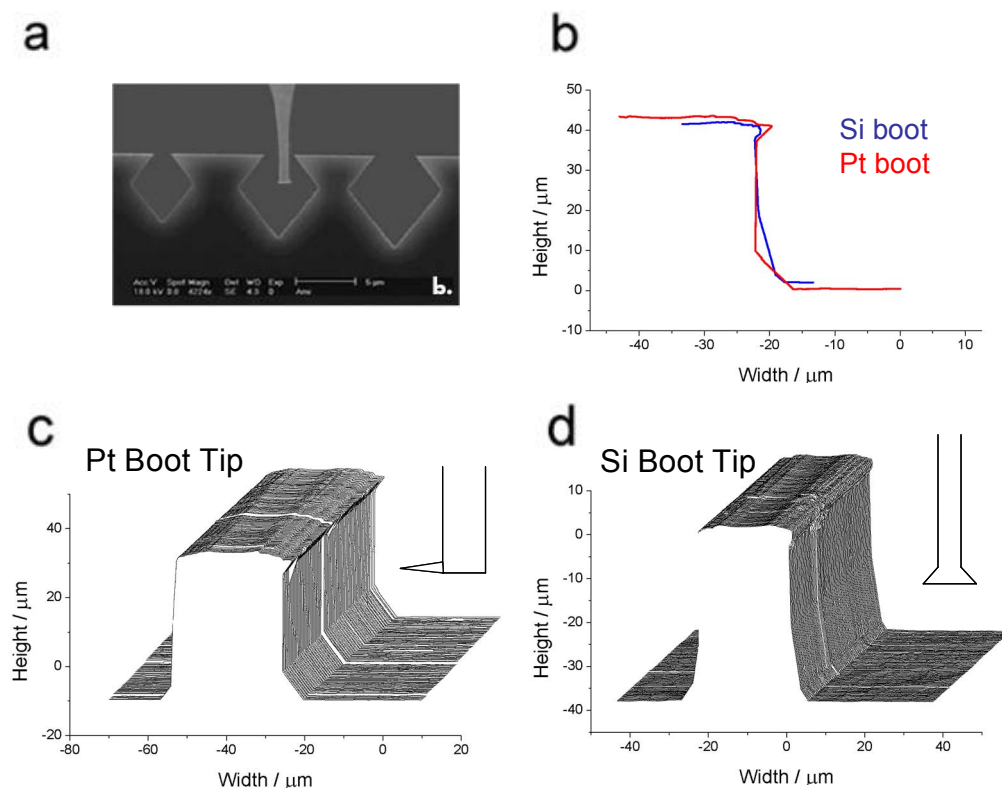


Figure 5.3 a) SEM image of a calibration standard used for tip characterization of 3D AFM probes. b) Line scans of data acquired with a Pt boot tip (red trace) and a Si boot tip (blue trace). The Pt boot tip (c) was able to probe 350% further into the undercut of the calibration standard than the conventional Si boot tip (d).

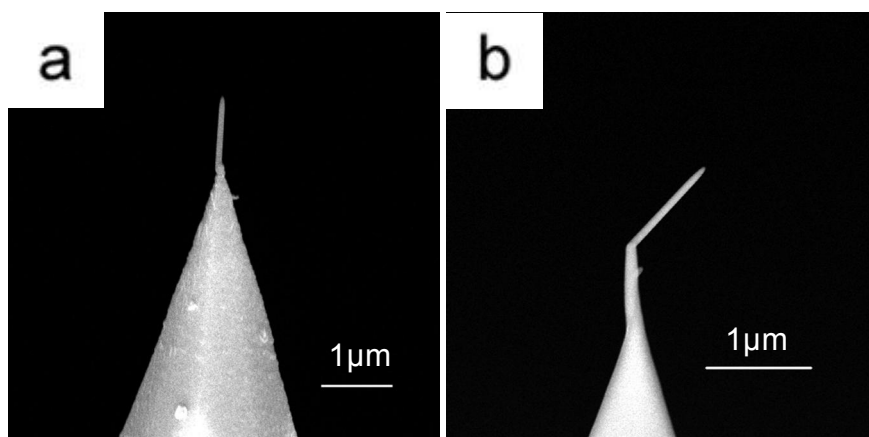


Figure 5.4 a) SEM image of a vertically oriented Pt spike deposited on a conventional AFM tip. b) The vertical structure was deposited to be a support structure for an angled Pt spike that would act as the imaging surface. The rigidity of the Pt deposits caused the structure to fail during use.

structure (Fig. 5.4b). This procedure could be repeated continuously to achieve the desired tip geometry and overhang. The clear advantage to this probe design is that the imaging surface for the vertical and horizontal components of the surfaces would be probed with the same point of the probe. This aspect would facilitate tip calibration and data interpretation, and it would provide a significant improvement in the resolution of horizontal and vertical dimensions. While the probes seemed like a suitable solution to the limitations of having a larger support structure as shown previously, the Pt column that acted as a base for the diagonal Pt imaging surface was fragile and susceptible to failure. Metal-based structures do not bend elastically, and are not the ideal structures to use in the development of 3D AFM probes. With this experience, carbon nanotubes were seen as a better alternative because of their ability to bend elastically, as well as their good wear characteristics.

5.3.2 3D CNT-Based AFM Probes

3D AFM probes based on carbon nanotubes are ideal for 3D AFM studies because they have a very narrow footprint (~20nm) and exhibit very good wear characteristics. 3D AFM probes were fabricated from 2D CNT-based AFM probes by adding small sections of CNTs to the existing apex-oriented carbon nanotube. Using the bias cutting method described in chapter 2, the CNT at the apex was cut to an appropriate length by contacting the CNT to an etched W wire. After the CNT was cut (Fig. 5.5a), the excess length of CNT bound to the W wire was put back into contact with the CNT at the

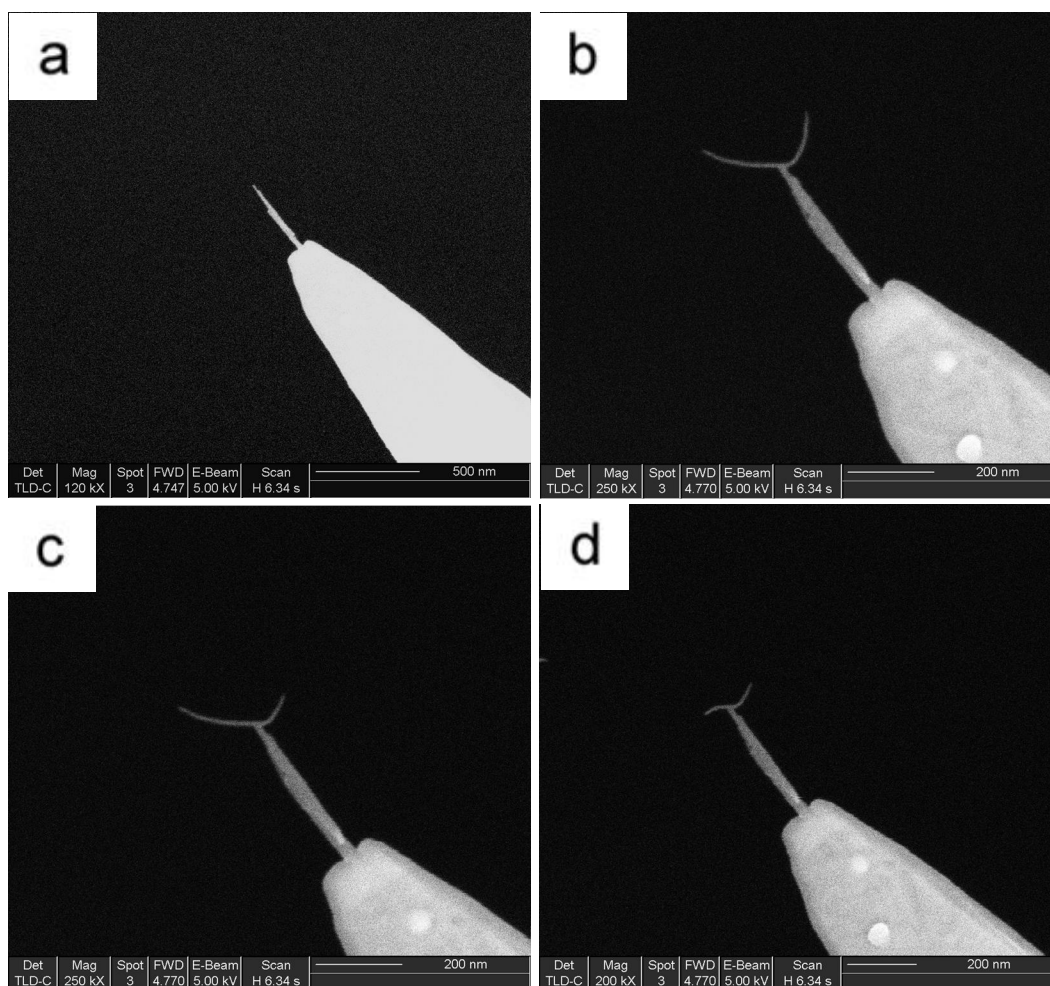


Figure 5.5 a) SEM micrograph of a CNT cut by the electrical cutting method described in chapter 2. b) By placing an additional CNT in contact with the CNT at the apex, a small section can be welded in place with EBID of C. c) Once welded, the resulting structure can be shortened by additional electrical cutting steps to fabricate a bidirectional boot tip (d).

apex at a 90° angle (Fig. 5.5b). Once the remaining CNT length was put into contact with the base CNT, the contact point was imaged at high magnification (>100kX) to induce C deposition from contaminations from pump oils in the SEM chamber. After imaging for approximately 20 seconds, the W wire was pulled away from the CNT junction. The CNTs typically remained bound at the connection point rather than pulling apart because the W-CNT junction in the cutting technique is held together by simple Van der Waals forces, which were weaker than the bond formed by the C deposition. Bringing the W wire back into contact with the joined CNTs allowed additional shortening steps, as shown in Figure 5.5c and d. As shown previously, the applied bias typically cuts the CNTs at the center of the length spanning between the W wire and the other connection point. This trend allows the CNT to be shortened in specific places to make complex structures specifically tailored to difficult sample geometries.

While seemingly a durable and effective design for probing large undercut features, the probe has some limitations. For instance, because the CNTs only extend from the front and back of the central CNT and not the sides, the probe is incapable of measuring undercuts along the Y axis. As a result, the only way to fully characterize a sample would be to change its orientation so the opposite axis could be interrogated. To truly be effective at imaging all axes, a probe must have imaging surfaces 360° around the base of the support structure, similar to that of conventional boot tips that have a

radially oriented flared ridge, or “boot”. This design enables sample interrogation at multiple scan directions.

5.3.3 3D C-CNT Boot Tips

Current Si-based boot tip fabrication methods are incapable of producing well defined boot tips when tip diameters are reduced to less than 100nm,²⁰ and in addition to having dull imaging surfaces at smaller size scales, durability is an issue because of the brittleness of the Si material. C-CNT based boot tips are an effective and durable alternative to Si based boot tips because they have an extremely small base structure (<10nm) and the boot is composed of highly durable material that has been described by some as diamond-like C.^{21, 22} As shown in Figs. 5.6a and 5.6b, boots were deposited on CNT AFM tips by chemical vapor deposition of C. After fabrication, the boot tips were scanned for 2 hours on an optical scatterometry grating to monitor the durability of the probes. SEM images of the probe revealed no change in the boot diameter or structure. Durability is one of the advantages of CNT based boot tips over Si based boot tips because the CNT support structure will bend elastically if the contact force between the C boot and the sample surface becomes too large. This advantage should allow the probes to be used for a longer duration than Si based boot tips. Another advantage of the C-CNT boot tips is that the C boot can be regenerated after significant wear has occurred. This advantage would allow boot tips to be refurbished and potentially used for thousands of hours, significantly reducing cost and time associated with probe changes.

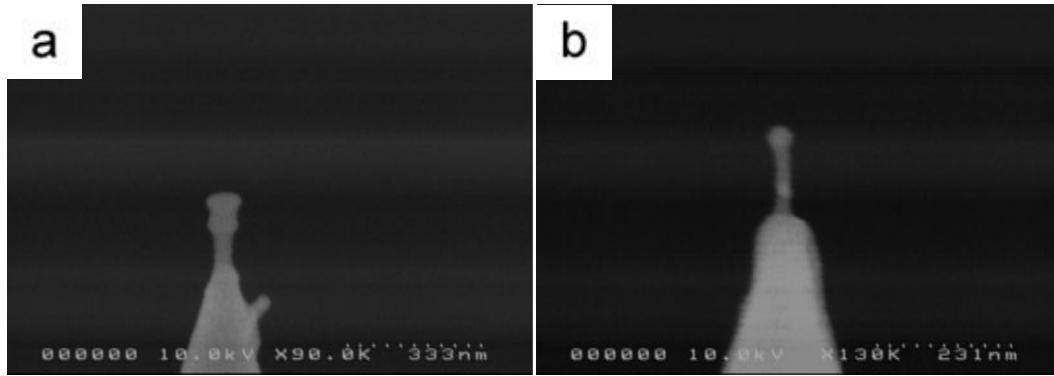


Figure 5.6 a) SEM image of a C-CNT boot tip fabricated by chemical vapor deposition of C on a CNT AFM tip prepared with the methods described in chapter 2. b) SEM image of a 40nm boot tip fabricated on a 20nm CNT. Boot tips on this small size scale are not commercially available because of limitations with current Si-based fabrication schemes.

5.3.4 Pt Spike NSOM Probes

Conventional optical fiber NSOM probes allow simultaneous acquisition of topographical and optical data, but like all scanning probe techniques, the probe limits the resolution of the measurement. In the case of topography, resolution is severely limited by the size of the probe. This large size is not ideal for use in studies of nanoscopic materials, and work has been undertaken to use existing methods to improve the resolution limits.

As shown in Figure 5.7a, optical fiber NSOM probes were coated with a layer of Al metal, which often partially or completely covered the aperture of the fiber. By carefully removing small amounts of the Al with a focused ion beam (Fig. 5.7b), the aperture size could be precisely controlled and the imaging surface could be flattened. After the aperture was exposed, a Pt nanoparticle was deposited with the electron beam induced deposition method described in chapters 2 and 3 (Fig. 5.7c)^{23, 24}. Careful attention was paid to the amount of Pt deposited on the aperture, because the optical resolution of NSOM fibers relies on the aperture staying within 10nm of the surface (Fig. 5.7d). After the probes were prepared, they were used to interrogate a gold pattern on ITO coated glass (Fig. 5.8a). The resulting shear force topography data revealed that the Pt nanoparticle NSOM fibers were capable of resolving 10nm gold particles (Fig. 5.8b), similar to the resolution capabilities of a conventional AFM tip (Fig. 5.8c). Conventional metal coated optical fibers are incapable of achieving this level of topographical

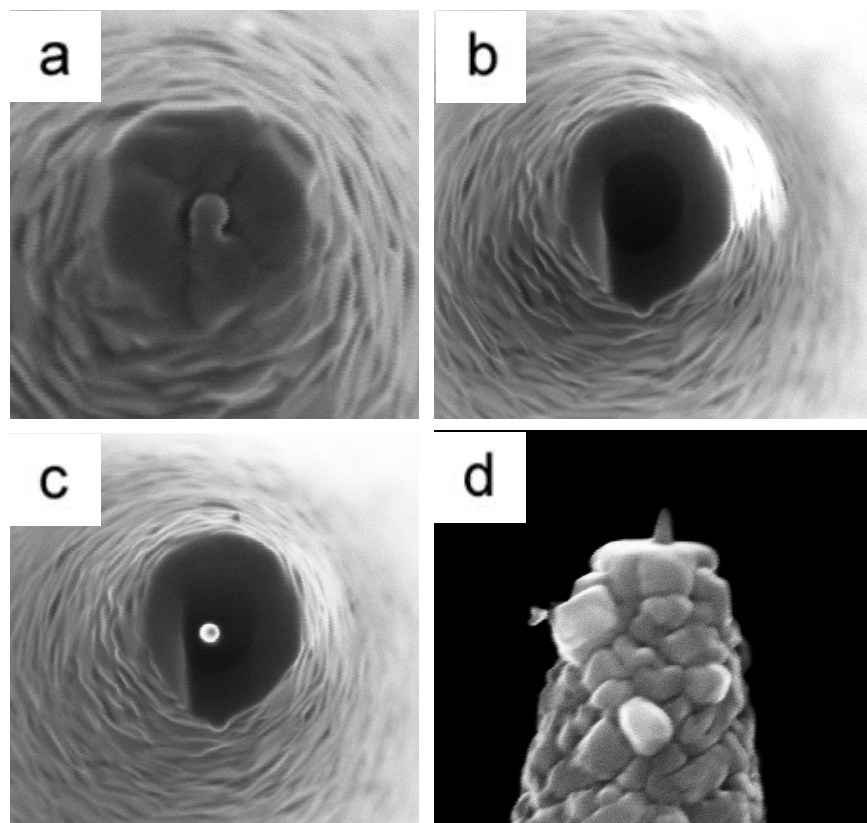


Figure 5.7 a) SEM micrograph of the apex of an Al coated NSOM optical fiber. The 200nm Al coating often results in a completely or partially covered aperture that must be removed by FIB milling. b) SEM micrograph of an NSOM fiber after FIB milling. c) Topographical resolution is poor with Al coated NSOM fibers because of their large size, so Pt nanoparticles were deposited on the aperture to act as the surface used for acquiring topographical data. d) Profile of the probe shown in C. The Pt particle height should not exceed 10nm or the optical resolution will be adversely affected.

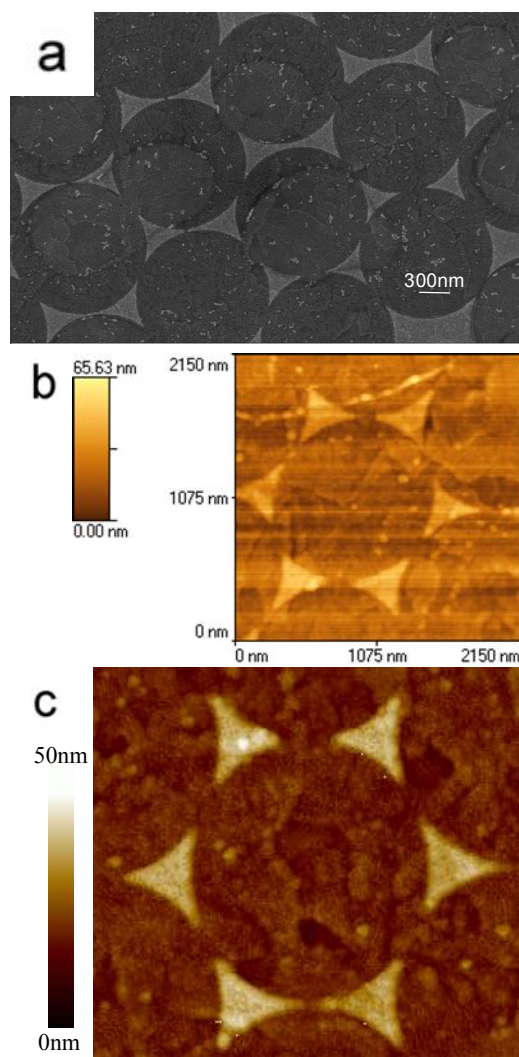


Figure 5.8 a) SEM micrograph of a gold pattern deposited on ITO. b) NSOM topographical data of the pattern acquired using a Pt nanoparticle NSOM probe. The addition of the Pt nanoparticle allowed the probe to resolve much smaller features than was possible with a conventional tapered optical fiber. c) $2 \times 2 \mu\text{m}$ AFM topography data of the pattern acquired using a conventional Si AFM tip showed comparable resolution to that of the Pt nanoparticle NSOM tip.

resolution, which makes correlation between topographical and optical data more complicated.

5.3.5 Combined SECM-AFM Probes

Scanning electrochemical microscopy is a powerful technique that allows mapping of electroactive surfaces, and its application has been important in understanding many different electrochemical systems. To improve upon the technique, several groups have suggesting coupling it with AFM to get topographical data to correlate with the electrochemical data. To combine these two techniques, special probes must be developed that combine the ultramicroelectrode with a nanoscopic AFM tip capable of achieving nanoscopic resolution. Hybrid SECM-AFM probes have been proposed that have large electrode surface areas, but the most promising probes have been CNT based because of their small size and simplicity of their data interpretation. The examples that have been proposed have limitations however, and these limitations will be addressed in future studies.

CNT based SECM-AFM probes are appealing because they offer nanoscopic electrode sizes and behave as disk electrodes for electrochemical measurements. While CNTs are conductive, their conductivity is less than that of metals such as gold or platinum. Others have circumvented this limitation by coating the CNT with a thin layer of metal, but this only serves to increase the size of the electrode and results in the formation of a disk-ring electrode because of the different conductivities of the metal and

the CNT. Pt spike based electrodes are being developed that utilize the conductivity, small size, and high aspect ratio to form the ideal SECM-AFM probe.

30 nm OD Pt spikes were deposited on Pt coated AFM tips by the EBID method described in chapter 3. Once deposited, the Pt spikes and Pt coated AFM tip were coated with parylene N in a home built vapor deposition chamber (Fig. 5.9a). A uniform coating of the nonconductive polymer was deposited so none of the surfaces would contribute to the electrochemical activity of the probe. After coating the probe with parylene, the apex of the Pt-parylene interface was removed with a focused ion beam (Fig. 5.9b) to form a disk electrode 30nm in diameter. Special care was taken to level off the Pt-parylene interface so the electrode would behave as a disk rather than an exposed sphere or cone. By using a focused ion beam to remove the parylene, unlike laser ablation methods that have been proposed, precisely controlled electrode surfaces can be created. Work towards evaluating and implementing these probes for combined atomic force and electrochemical microscopy is currently underway, and will be explored in the future.

5.4 CONCLUSIONS

Utilizing methods and knowledge from experience acquired from the CNT and Pt spike studies discussed in chapters 2 and 3, advanced probes for 3D atomic force microscopy, near-field scanning optical microscopy, and scanning electrochemical – atomic force microscopy have been fabricated. 3D C-CNT probes have been identified as a great

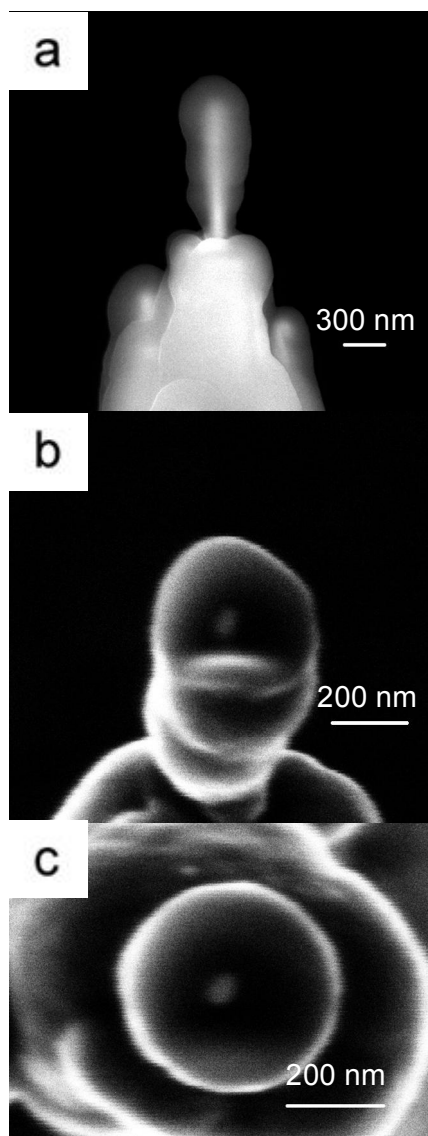


Figure 5.9 a) SEM image of a Pt Spike AFM tip coated with a thin layer of parylene N polymer. Coating the entire surface allows only the end of the Pt tip to be the electroactive area in combined SECM-AFM measurements. b) SEM image of the SECM-AFM tip shown in (a) after the end was removed with a focused ion beam. c) Removal of the polymer and apex of the Pt spike allows the formation of a 30nm disk electrode.

alternative to commercially available Si-based boot tips because of their small size, high durability, and ability to be regenerated after extensive use. Newly developed nanoscopic resolution standards will be studied in the future to compare the performance of 3D C-CNT boot tips with that of commercially available Si-based 3D boot tips. Pt spike NSOM tips have been fabricated that have significantly enhanced topographical resolution, but future studies will determine if the Pt nanoparticle can be used as a nanoantenna for optical resolution enhancement.²³ Additionally, future studies will also focus on the effect of spike material (e.g., Pt, Au, Pd, etc.) on optical resolution enhancement. Last, Pt spike based SECM-AFM tips have been developed for use in nanoscopic combined electrochemical and topographical studies. More studies are needed to characterize the electrochemical behavior of the 30nm disk electrode, but once characterized, nanoscale electrochemical studies such as determining the electrochemical activity of nanoscale domains in metal and mixed-metal oxides can be conducted. Preliminary results indicate that further development of 3D C-CNT boot tips, Pt spike NSOM probes, and Pt spike SECM-AFM probes will allow their respective techniques to achieve unprecedented resolution, and will facilitate their use in current and future nanoscopic studies.

5.5 REFERENCES

1. Dahlen, G.; Osborn, M.; Okulan, N.; Foreman, W.; Chand, A. Tip Characterization and Surface Reconstruction of Complex Structures with Critical Dimension Atomic Force Microscopy. *J. Vac. Sci. Technol B* **2005**, *23*(6), 2297-2303.
2. Caldwell, M.; Bao, T.; Hackenberg, J.; McLain, B.; Munoz, O.; Stephens, T.; Vartanian, V. Improved Dimension and Shape Metrology with Versatile Atomic Force Microscopy. *Proc. of SPIE* **2007**, *6518*, 65181L 1-10.
3. Hsieh, M. H.; Shi, K. H.; Yeh, J. H.; Hsu, R. H.; Tsai, M.; Tzou, S. F. Use of In-Line AFM as LWR Verification Tool in 45nm Process Development. *Proc. of SPIE* **2007**, *6518*, 651833 1-6.
4. Thiault, J.; Foucher, J.; Tortai, J. H.; Joubert, O.; Landis, S.; Pauliac, S. Line Edge Roughness Characterization with a Three-Dimensional Atomic Force Microscope: Transfer During Gate Patterning Processes. *J. Vac. Sci. Technol B* **2005**, *23*(6), 3075-3079.
5. Liu, H.; Klonowski, M.; Dahlen, D.; Osborn, M.; Bao, T. Advanced Atomic Force Microscopy Probes: Wear Resistant Designs. *J. Vac. Sci. Technol. B* **2005**, *23*(6), 3090-3093.
6. Fowles, G. R. *Introduction to Modern Optics*, 2nd ed, Dover Publications, Inc.: New York, **1989**.
7. Synge, E. H. *Phil. Mag.* **1928**, *6*, 356.
8. Paesler, P. A.; Moyer, P. J. *Near-Field Optics: Theory, Instrumentation, and Applications*; John Wiley & Sons, Inc.: New York, **1996**.
9. Hecht, B.; Sick, B.; Wild, U. P.; Deckert, V.; Zenobi, R.; Martin, O. J.; Pohl, D. W. *J. Chem. Phys.* **2000**, *112*, 7761-7774.
10. Bard, A. J.; Faulkner, L. R. *Electrochemical Methods: Fundamentals and Applications*, 2nd ed. John Wiley & Sons, Inc.: New York, **2001**.

11. Bard, A. J.; Denuault, G.; Friesner, R. A.; Dornblaser, B. C.; Tuckerman, L. Scanning Electrochemical Microscopy: Theory and Application of the Transient (Chronoamperometric) SECM Response. *Anal. Chem.* **1991**, *63*, 1282-1288.
12. Bard, A. J.; Fan, F. R. F.; Kwak, J.; Lev, O. Scanning Electrochemical Microscopy. Introduction and Principles. *Anal. Chem.* **1989**, *61*, 132-138.
13. Gullo, M. R.; Frederix, P. L. T. M.; Akiyama, T.; Engel, A.; deRooij, N. J.; Staufer, U. Characterization of Microfabricated Probes for Combined Atomic Force and High-Resolution Scanning Electrochemical Microscopy. *Anal. Chem.* **2006**, *78*(15), 5436-5442.
14. Burt, D. P.; Wilson, N. R.; Weaver, J. M. R.; Dobson, P. S. Macpherson, J. V. Nanowire Probes for High Resolution Combined Scanning Electrochemical Microscopy – Atomic Force Microscopy. *Nano Lett.* **2005**, *5*(4), 639-643.
15. Dobson, P. S.; Weaver, J. M. R.; Holder, M. N.; Unwin, P. R.; Macpherson, J. V. Characterization of Batch-Microfabricated Scanning Electrochemical-Atomic Force Microscopy Probes. *Anal. Chem.* **2005**, *77*, 424-434.
16. Frederix, P. L. T. M.; Gullo, M. R.; Akiyama, T.; Tonin, A.; deRooij, N. J.; Staufer, U.; Engel, A. Assesment of Insulated Conductive Cantilevers for Biology and Electrochemistry. *Nanotechnology* **2005**, *16*, 997-1005.
17. Fasching, R. J.; Tao, Y.; Prinz, F. B. Cantilever Tip Probe Arrays for Simultaneous SECM and AFM Analysis. *Sens. Act. B* **2005**, *108*, 964-972.
18. Dunn, R. C. *Chem. Rev.* **1999**, *99*, 2891-2927.
19. Macpherson, J. V.; Unwin, P. R. Combined Scanning Electrochemical – Atomic Force Microscopy. *Anal. Chem.* **2000**, *72*, 276-285.
20. Patil, A.; Sippel, J.; Martin, G. W.; Rinzler, A. G. Enhanced Functionality of Nanotube Atomic Force Microscopy Tips by Polymer Coating. *Nano Lett.* **2004**, *4*(2), 303-308.
21. <http://www.veeco.com>

22. Ding, W.; Dikin, D. A.; Chen, R. D.; Piner, R. D.; Ruoff, R. S.; Zussman, E.; Wang, X.; Li, X. Mechanics of Hydrogenated Amorphous Carbon Deposits From Electron-Beam-Induced Deposition of a Paraffin Precursor. *J. Appl. Phys.* **2005**, *98*, 014905 1-7.
23. Kometani, R.; Kanda, K.; Haruyama, Y.; Kaito, T.; Matsui, S. Evaluation of Field Electron Emitter Fabricated Using Focused-Ion-Beam Chemical Vapor Deposition. *Jpn. J. Appl. Phys.* **2006**, *45*(27), L711-L713.
24. Taminiau, T. H.; Moerland, R. J.; Segerink, S. B.; Kuipers, L.; van Hulst, N. F. *Nano Lett.* **2007**, *7*(1), 28-33.
25. Frey, H. G.; Keilmann, F.; Kriele, A.; Guckenberger, R. *Phys. Rev. Lett.* **2004**, *93*(20), 200801.

Vita

Ryan Donald Williams was born March 31, 1981 in Searcy, Arkansas. He is the son of Steven and Susan Williams. After graduating from McAlester High School, McAlester, Oklahoma, in 1999, he entered Harding University located in Searcy, Arkansas. He graduated from Harding University with a Bachelor of Science degree in Chemistry in May 2003. In August 2003 he entered the University of Texas at Austin to pursue his Doctorate in Chemistry under the guidance of Professor Keith J. Stevenson.

Permanent address: 37 Quail Ct., McAlester, OK 74501

This dissertation was typed by the author.